



Published in final edited form as:

Cell Metab. 2017 April 04; 25(4): 838–855.e15. doi:10.1016/j.cmet.2017.03.003.

SIRT4 is a Lysine Deacylase that Controls Leucine Metabolism and Insulin Secretion

Kristin A. Anderson^{1,2,*}, Frank K. Huynh^{1,*}, Kelsey Fisher-Wellman¹, J. Darren Stuart¹, Brett S. Peterson¹, Jonathan D. Douros¹, Gregory R. Wagner¹, J. Will Thompson^{2,3}, Andreas S. Madsen⁴, Michelle F. Green¹, R. Michael Sivley⁵, Olga R. Ilkayeva¹, Robert D. Stevens¹, Donald S. Backos⁶, John A. Capra⁵, Christian A. Olsen⁴, Jonathan E. Campbell^{1,2,7}, Deborah M. Muoio^{1,2,7}, Paul A. Grimsrud¹, and Matthew D. Hirschey^{1,2,7,8,**}

¹Duke Molecular Physiology Institute and Sarah W. Stedman Nutrition and Metabolism Center, Duke University Medical Center, Durham, NC 27701

²Department of Pharmacology & Cancer Biology, Duke University Medical Center, Durham, NC 27710

³Duke Proteomics and Metabolomics Shared Resource, Duke University Medical Center, Durham, NC 27710

⁴Center for Biopharmaceuticals and Department of Drug Design and Pharmacology, Faculty of Health and Medical Sciences, University of Copenhagen, Universitetsparken 2, 2100, Copenhagen, Denmark

⁵Department of Biological Sciences, Department of Biomedical Informatics, Vanderbilt Genetics Institute, Center for Structural Biology, Vanderbilt University, Nashville, TN 37235

⁶Computational Chemistry and Biology Core Facility, Skaggs School of Pharmacy and Pharmaceutical Sciences, University of Colorado Anschutz Medical Campus, Aurora, CO, USA

⁷Department of Medicine, Division of Endocrinology, Metabolism, and Nutrition, Duke University Medical Center, Durham, NC 27710

SUMMARY

Sirtuins are NAD⁺-dependent protein deacylases that regulate several aspects of metabolism and aging. In contrast to the other mammalian sirtuins, the primary enzymatic activity of mitochondrial sirtuin 4 (SIRT4) and its overall role in metabolic control has remained enigmatic.

** Correspondence: matthew.hirschey@duke.edu.

⁸Lead Contact

* Co-first author

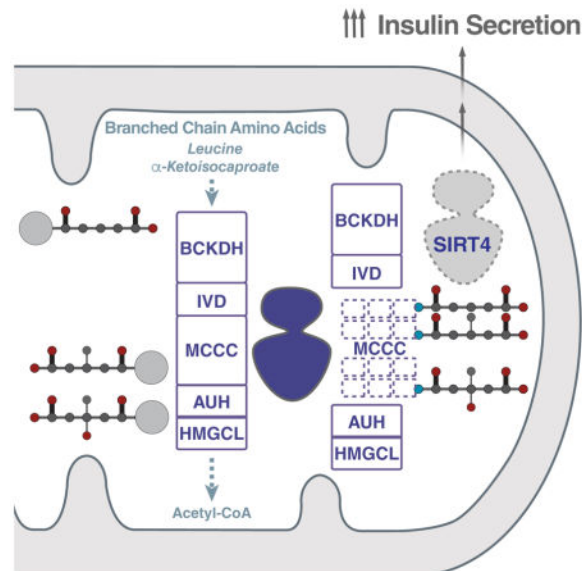
AUTHOR CONTRIBUTIONS

Conceptualization, K.A.A., F.K.H. and M.D.H.; Investigation, K.A.A., F.K.H., K.F-W., J.D.S., B.S.P., J.D.D., G.R.W., J.W.T., A.S.M., M.F.G., R.M.S., O.R.I., R.D.S., D.S.B., P.A.G.; Writing - Original Draft, K.A.A., F.K.H., K.F-W., M.D.H.; Writing - Review & Editing, All authors; Supervision, J.A.C., C.A.O., J.E.C., D.M.M., M.D.H.; Project Administration, M.D.H.; Funding Acquisition, M.D.H.

Publisher's Disclaimer: This is a PDF file of an unedited manuscript that has been accepted for publication. As a service to our customers we are providing this early version of the manuscript. The manuscript will undergo copyediting, typesetting, and review of the resulting proof before it is published in its final citable form. Please note that during the production process errors may be discovered which could affect the content, and all legal disclaimers that apply to the journal pertain.

Using a combination of phylogenetics, structural biology, and enzymology, we show that SIRT4 removes three acyl moieties from lysine residues – methylglutaryl(MG)-, hydroxymethylglutaryl(HMG)-, and 3-methylglutaconyl(MGc)-lysine. The metabolites leading to these post-translational modifications are intermediates in leucine oxidation, and we show a primary role for SIRT4 in controlling this pathway in mice. Furthermore, we find that dysregulated leucine metabolism in SIRT4KO mice leads to elevated basal and stimulated insulin secretion, which progressively develops into glucose intolerance and insulin resistance. These findings identify a robust enzymatic activity for SIRT4, uncover a mechanism controlling branched-chain amino acid flux, and position SIRT4 as a crucial player maintaining insulin secretion and glucose homeostasis during aging.

Graphical abstract



Keywords

sirtuin 4; deacylase; mitochondria; branched-chain amino acids; leucine; insulin secretion

INTRODUCTION

The sirtuin proteins (mammalian SIRT1-7) are a class of NAD⁺-dependent protein deacylases that remove post-translational acyl modifications from various cellular substrates to regulate a wide range of biological pathways (Anderson et al., 2014). Importantly, activation or over-expression of sirtuins increases healthspan and lifespan in several model organisms (Hall et al., 2013). Conversely, ablation or inhibition of sirtuins accelerates the onset of several aging phenotypes (Houtkooper et al., 2012).

Originally thought to be strictly lysine deacetylases (Imai et al., 2000; Verdin et al., 2004) or ADP-ribosyltransferases (Tanny et al., 1999), more recent studies have shown that the sirtuins remove several post-translational modifications (PTMs) from lysine residues

(Anderson et al., 2014). SIRT1-3 are strong lysine deacetylases, with the additional ability to hydrolyze longer chain acyl modifications (Feldman et al., 2013; Madsen et al., 2016). SIRT5 is a lysine demalonylase (Peng et al., 2011), desuccinylase (Du et al., 2011), and deglutarylase (Tan et al., 2014). SIRT6 is a highly specific lysine deacetylase (Michishita et al., 2008; Mostoslavsky et al., 2006), as well as a long-chain deacylase (Jiang et al., 2013). Because sirtuins with unique enzymatic activities each occupy a distinct phylogenetic subclass, the phylogeny has been suggested to provide key information about sirtuin enzymatic activity (Hirschey, 2011).

In contrast to SIRT1-3, 5 and 6, the primary enzymatic activity of SIRT4 remains enigmatic. SIRT4 resides in the mitochondria and was originally thought to be an ADP-ribosyltransferase (Ahuja et al., 2007; Haigis et al., 2006); however, this activity has been called into question as its primary enzymatic function (Du et al., 2009). SIRT4 has also been described as a lysine deacetylase (Laurent et al., 2013b), but recombinant SIRT4 does not catalyze deacetylation on a variety of substrates (Feldman et al., 2013; Verdin et al., 2004). Furthermore, SIRT4 showed no deacylation activity against known dicarboxyl-acyl modifications (Peng et al., 2011; Tan et al., 2014), and does not efficiently remove long-chain acyl modifications (Feldman et al., 2013; Madsen et al., 2016). A recent report described SIRT4 as a lipoamidase (Mathias et al., 2014), but robust lipoamidase activity was not seen using well-established sirtuin deacylation assays (Feldman et al., 2013). Thus, a strong, consistent enzymatic activity for SIRT4 has not yet been identified.

Despite this gap in knowledge, SIRT4 has been shown to influence important biological pathways. *Sirt4* ablation in mice activates glutamate dehydrogenase, leading to increased glutamine metabolism (Csibi et al., 2013; Jeong et al., 2014; Jeong et al., 2013). Several human cancers, including those with the worst prognoses (e.g. lung, gastric, and colorectal cancer) are associated with decreased expression of SIRT4 (Jeong et al., 2013; Miyo et al., 2015). SIRT4 also regulates pathways important in metabolic diseases such as diabetes and obesity. Both glucose and amino acid-stimulated insulin secretion are increased in the absence of SIRT4 (Ahuja et al., 2007; Haigis et al., 2006). Additionally, several studies have shown that SIRT4 can reduce fatty acid oxidation and/or increase lipid synthesis via various mechanisms (Ho et al., 2013; Laurent et al., 2013a; Laurent et al., 2013b; Nasrin et al., 2010). Therefore, SIRT4 has important regulatory roles in several disease pathways; however, the mechanisms linking SIRT4 enzymatic activity to regulating these pathways are not yet known.

The emerging idea that sirtuins have several enzymatic activities, coupled with the notion that previous reports identified relatively weak activities for SIRT4 compared to the other mammalian sirtuins, suggested to us that SIRT4 might have an undiscovered, robust enzymatic activity. As a result, we set out to determine if SIRT4 was a lysine deacetylase targeting a novel PTM, with the overall goal to understand the role of SIRT4 in metabolism and the diseases of aging.

RESULTS

Phylogenetic and Structural Analyses of SIRT4

To gain insight into possible SIRT4 activities, we first analyzed the sequence and structural features of the enzyme. We found that SIRT4 has the requisite amino acids known to participate in deacylase reactions (Fig. 1A and Fig. S1A). In particular, SIRT4 contains a homologous sirtuin deacylase domain, a conserved catalytic histidine (H161), and a Rossmann fold (Min et al., 2001) NAD⁺-binding motif (amino acids 62–82, 143–146, 260–262, 286–288) (Fig. 1A). Next, we modeled the secondary structure of SIRT4 (Rost and Liu, 2003) and found that it contains predicted α -helices (Fig. 1B; above the x-axis) and predicted β -sheets (Fig. 1B; below the x-axis) in nearly identical locations to the other mitochondrial sirtuins SIRT3 and SIRT5. Together, these data show that the primary sequence and predicted secondary structure of SIRT4 are highly similar to the other mitochondrial sirtuins and contain the requisite features of a sirtuin deacylase enzyme to catalyze a deacylation reaction.

Next, we sought to identify regions within SIRT4 that could be important for its enzymatic activity. Phylogenetic analysis can reveal patterns of evolutionary pressure on specific amino acids that could be important for the function of the protein. For example, the mitochondrial sirtuin SIRT5 contains an evolutionarily conserved arginine (R) and tyrosine (Y) on an α -helix in the catalytic pocket, which confers its specificity to deacylating negatively charged dicarboxyl-acyl moieties (Du et al., 2011). We performed a phylogenetic analysis of 5,869 sirtuin domains from proteins across 3,562 species (Fig. S1B). Previous phylogenetic studies of sirtuins from approximately 30 (Frye, 2000) and 70 (Greiss and Gartner, 2009) sequenced species divided the human sirtuins into four classes: SIRT1-3 occupy class I, SIRT4 occupies class II, SIRT5 occupies class III, and SIRT6 and SIRT7 occupy class IV. Our updated analysis supports this grouping (Fig. 1C and Fig. S1C) and provides a detailed evolutionary context in which to explore the patterns of conservation and difference among class II sirtuins, which show highest sequence similarity to human SIRT4.

We identified a region in human SIRT4 that showed high similarity to other species within the SIRT4 class (Fig. 1D) but was not found in any other classes (Fig. 1E). To quantify the uniqueness of this region, we applied the GroupSim algorithm for identifying specificity determining positions (SDPs) to discover alignment positions with conserved amino acid preferences within and differences between the four classes of human sirtuins (Capra and Singh, 2008). We found that position 103 (the Q in the RQRYWAR) received the highest SDP score and position 104 (the second R in the RQRYWAR) received the sixth highest score (Fig. 1D and Fig. S1D). This analysis suggested that the conserved region was under strong evolutionary pressure between the four classes of sirtuins and supported the idea that this region could be important for SIRT4 enzymatic activity.

Interestingly, a proline residue, which is often the start of an α -helix, is positioned two residues upstream of this unique amino acid sequence in human SIRT4. Indeed, α -helical wheel prediction algorithms showed this region was highly likely to be helical (Fig. 1F). In a protein sequence alignment, this helix was in a similar position to the α -helix within the catalytic pocket of SIRT5 that conferred its enzymatic specificity towards dicarboxylic acid-

modified lysines (Figs. 1B cyan and 1F), including malonyl-, succinyl-, and glutaryl-lysines. Together, these data suggest that this region is an α -helix within the catalytic pocket of SIRT4 and could confer specificity for a novel acyl-lysine substrate.

To determine the location of this α -helix within SIRT4, we built a homology model of the structure of SIRT4 based on its high level of sequence similarity to the other sirtuins. We found SIRT5 to contain the highest level of protein sequence conservation (~30% identical and ~50% conserved; Fig. S2). Given that SIRT5 has several solved crystal structures (Du et al., 2011; Schuetz et al., 2007), we used a structure with the substrate bound (Du et al., 2011) as a template to build a homology model of SIRT4 (Fig. 2A). This model showed the highly conserved α -helix at the back of the SIRT4 catalytic pocket (Figs. 2A and 2B). These data are consistent with our phylogenetic analyses and suggest that this region of SIRT4, like SIRT5, could target an acyl-lysine modification.

To further explore the possibility that this putative α -helix within SIRT4 could coordinate a novel modification, we performed molecular dynamic simulations on a library of modified lysines based on known post-translational modifications (Table S1). Also included in the library are modified lysines predicted to occur based on the physiological existence of the corresponding reactive acyl-CoAs or predicted reactive metabolites (Wagner et al., 2017). We then compared the relative abilities of SIRT3, SIRT4, or SIRT5 to favorably bind (negative interaction energies) to these modified lysines by plotting their z-scores (Fig. 2C and Table S1). Importantly, SIRT3 and SIRT5 showed favorable binding energies to modifications they are known to target. While the acetyl modification is not long enough to reach the α -helix in SIRT3's binding pocket (Madsen et al., 2016), medium- and long-chain uncharged acyl modifications showed favorable binding energies (Fig. 2C). Similarly, the model showed that negatively charged acyl modifications (e.g. malonyl-, succinyl-, and glutaryl-modifications) favorably bound within the catalytic pocket of SIRT5 (Fig. 2C). These data support the use of this prediction tool to identify and prioritize possible substrates for testing.

When performing this analysis on our SIRT4 model, we found 3-hydroxy-3-methylglutaryl (HMG)-lysine was the most favorable substrate bound (Fig. 2C). Other structurally similar modifications, including 3-methylglutaryl(MG)-lysine, and other negatively charged dicarboxyacetyl-lysine modifications, including succinyl-, glutaryl-, and adipoyl-lysine, also showed favorable binding in the model of SIRT4 (Fig. 2C). In contrast, we found no favorable binding of lipoyl-lysine to our SIRT4 model, suggesting low binding affinities of this previously reported modification (Fig. 2C and Table S1). Collectively, these analyses support the idea that an evolutionarily conserved α -helical region in the catalytic pocket of SIRT4 could confer specificity to a negatively charged lysine modification.

SIRT4 is a Lysine Deacylase

Based on these predictions, we began testing for SIRT4 enzymatic activities with a particular emphasis on negatively charged modifications (Fig. 3A), which might interact with the positively charged α -helix in the catalytic pocket of SIRT4. First, we turned to a well-established sirtuin deacylation assay that monitors the consumption of $^{32}\text{P-NAD}^+$ (Zhu et al., 2013), based on the rationale that all sirtuins require NAD^+ as a co-substrate during catalytic

deacylation, and that the readout of this assay would be agnostic to the nature of the lysine acyl modification. We focused initially on MG-lysine, a novel putative substrate identified in our modeling studies (Fig. 3A). We generated MG-modified BSA using 3-methylglutaric anhydride and confirmed its modification by gel electrophoresis (Fig. S3A). Using this substrate, we tested recombinant GST-tagged human SIRT4 obtained from a commercial source but did not observe any enzymatic activity (Fig. S3B).

Newly synthesized proteins targeted to the mitochondria often have a targeting signal (MTS) consisting of 10–70 amino acids at the N-terminus, which is often cleaved inside mitochondria. The mitochondrial sirtuins SIRT3 and SIRT5 each have an MTS (Nakagawa et al., 2009; Schwer et al., 2006), which needs to be cleaved for full activity (Fig. 1A, black). Thus, we considered that either an improperly removed MTS or the recombinant protein tag could be interfering with the catalytic activity of the enzyme. Therefore, we amplified *Sirt4* cDNA by PCR from mouse liver, sub-cloned it into a mammalian expression vector, and over-expressed FLAG-tagged mouse SIRT4 (SIRT4) in mammalian cells. We then sequenced the over-expressed SIRT4 protein by mass spectrometry and identified a putative mitochondrial target signal at residues 1–23 (Figs. 1A, 1B, and Fig. S3C), which is in agreement with a previously published report (Haigis et al., 2006). Next, we cloned a truncated version of SIRT4 that encodes the processed, mature protein for expression in bacteria with an N-terminal GST tag that is cleavable (Fig. S3D). Remarkably, we found SIRT4 with the GST tag was not active, but SIRT4 without the GST tag showed robust activity against MG-BSA (Fig. 3B). To validate this enzymatic activity, we generated catalytically inactive SIRT4 by mutating the catalytic histidine residue to tyrosine (SIRT4HY), expressed it in the same bacterial system, and detected no activity either with the uncleaved or cleaved forms of the protein (Fig 3B). Importantly, while demethylglutarylase activity was detected by cleaved SIRT4, deacetylase and delipoylase activities were below detection limits of our assay indicating selectivity of SIRT4 for MG-lysine (Fig. 3B). Together, these data show that SIRT4 catalyzes the NAD⁺-dependent demethylglutarylation of lysine residues.

Next, we tested the specificity of SIRT4 activity. We generated a series of protein substrates using acid anhydrides and acyl-CoAs to chemically modify BSA, validated each by gel electrophoresis and/or mass spectrometry (Fig. S3A, Table S1), and subjected these to the ³²P-NAD⁺-consumption assay. We first explored the chemical space surrounding MG-lysine by testing structurally similar modifications that showed favorable binding by molecular modeling (Figs. 2C, 3A). We tested glutaryl-lysine and observed strong enzymatic activity against this substrate (Fig. 3C). Then, we tested 3-hydroxy-3-methylglutaryl (HMG)-lysine and also found deacylase activity (Fig. 3C). We further tested a wide range of modified proteins or peptides using the ³²P-NAD⁺-consumption assay and found the two modifications most efficiently removed by SIRT4 were glutaryl- and MG-lysine, followed by HMG-lysine (Fig. 3C and Table S1), which is consistent with our *in silico* predictions of preference for negatively charged five carbon backbone acyl modifications.

To determine whether the other mitochondrial sirtuins could remove these modifications, we tested SIRT3 and SIRT5 in this same assay (Fig. 3D). We found that SIRT3 efficiently removed acetyl-modifications from BSA but not any negatively charged modifications (Fig.

3D) as reported previously (Feldman et al., 2013; Madsen et al., 2016; Madsen and Olsen, 2012). We found that SIRT5 efficiently targeted succinyl-lysine and glutaryl-lysine (Fig. 3D), as previously reported (Du et al., 2011; Tan et al., 2014). However, we found low or non-detectable activity against MG- and HMG-lysine, suggesting that SIRT4 specifically targets these modifications (Fig. 3D).

Several acyl-CoA species are reactive metabolites that are the carbon source for protein modifications (Wagner et al., 2017; Wagner and Payne, 2013), but 3-methylglutaryl-CoA (MG-CoA) is not a metabolite known to be generated directly from any enzymes in humans (Wishart et al., 2013). Interestingly, the structurally similar 3-methylglutaconyl-CoA (MGc-CoA; Fig. 3A) is an intermediary metabolite in leucine catabolism (Wishart et al., 2013) and MG-CoA is thought to originate from the chemical or enzymatic reduction of MGc-CoA (Roe et al., 1986). Because the difference between MG-CoA and MGc-CoA is one double bond, we considered the possibility that proteins could become 3-methylglutaconylated (MGc) and that SIRT4 might target this modification for removal.

To test this hypothesis, and to further validate the enzymatic activities described above (Fig. 3C), we turned to another sirtuin assay based on deacylation of a fluorogenic aminomethyl-coumarin (AMC) peptide substrate (Marcotte et al., 2004). We synthesized several substrates (Table S1) and tested their ability to be deacylated by SIRT4 (Fig. 3E) or the remaining mammalian sirtuins SIRT1-7 (Fig. S3B). In accordance with the NAD⁺-consumption assay, we found SIRT4 preferentially removed glutaryl- and MG-lysine modifications, followed by HMG- and MGc-lysine. Furthermore, we found that SIRT4 was inhibited by nicotinamide (Fig. 3F), similar to the other sirtuin enzymes. Finally, because our phylogenetic and structural analyses predicted an important role for tyrosine 105 and arginine 108 in the catalytic pocket of SIRT4 to coordinate negatively charged substrates (Figures 1 & 2), we generated SIRT4 with these residues mutated to abrogate their charge and tested the enzymatic activity (Y105F and R108Q; SIRT4FQ mutant). After cleaving the recombinant protein tag (Fig. S3E), we found the SIRT4FQ mutant had lower activity than wild-type SIRT4 (Fig. 3G), supporting the idea that this region was under evolutionary pressure due to its importance for enzymatic activity. Interestingly, elevating the substrate concentration from 50 μ M to 500 μ M in this assay reduced the difference between SIRT4 and SIRT4FQ activity (data not shown), suggesting that the SIRT4FQ has a lower substrate binding affinity and that the α -helical region coordinates enzyme substrates. Therefore, using two validated, well-established sirtuin activity assays, we identified several novel enzymatic activities for SIRT4.

Since neither chemically modified BSA nor pseudo-peptides are physiological substrates for SIRT4, we tested the ability of SIRT4 to remove these modifications in cells. To do so, we first generated antibodies against the modifications most potently targeted by SIRT4, namely glutaryl-lysine, HMG-lysine, and MG-lysine, and validated their ability to recognize acyl-lysine modified proteins (Fig. S3F). Using these novel antibodies, we measured protein acylation in HEK293 cells stably overexpressing SIRT4. Compared to control cells, we found that cells overexpressing SIRT4 have an overall decrease in the level of all three of the novel acyl-lysine modifications (Fig. 3H), consistent with the *in vitro* findings. Collectively,

our data show that SIRT4 can remove negatively charged five-carbon backbone modifications from a wide range of protein substrates.

SIRT4 Controls Leucine Metabolism

Next, in order to identify the proteins and pathways that SIRT4 could be targeting, we used a proteomics approach to identify SIRT4 binding partners. Using a bait-prey co-immunoprecipitation strategy, we identified interacting partners with mouse and human SIRT3, SIRT4, and SIRT5 (Table S2). We prioritized proteins based on percent coverage and then identified the interactions that were unique to SIRT4 compared to the other mitochondrial sirtuins. Importantly, we found SIRT4 interacted with several previously described binding partners (Mathias et al., 2014). We next tested for pathway enrichment of putative interacting partners using Ingenuity Pathway Analysis, and found “valine, leucine, & isoleucine metabolism” as one of the top pathways containing SIRT4 binding proteins (Fig. S4). Remarkably, the acyl-CoA species that lead to modifications that SIRT4 targets are intermediates formed in leucine catabolism, supporting the hypothesis that SIRT4 could control leucine metabolism by deacylating proteins in this pathway (Wagner et al., 2017).

Inspection of the proteins driving this enrichment revealed methylcrotonyl-CoA carboxylase A and B (MCCA and MCCB, a.k.a. MCCC1 and MCCC2) as interacting proteins (Table S2), which form a heterododecamer enzyme complex in the leucine oxidation pathway (Fig. 4A). The methylcrotonyl-CoA carboxylase complex (MCCC) was previously shown to interact with SIRT4 and was thought to be a putative substrate of SIRT4 (Wirth et al., 2013). Importantly, the MCCC enzyme generates MGc-CoA, which can be chemically or enzymatically reduced to MG-CoA (Roe et al., 1986). Both of these activated carbon species can non-enzymatically modify proteins (Wagner et al., 2017) and are targets of SIRT4-mediated deacylation (Fig. 3E). Thus, we tested the hypothesis that MCCC was acylated and was a substrate for SIRT4.

First, we measured the acylation status of MCCC in wild-type and SIRT4KO mice. Using the methylglutaryl-lysine antibody, we found MCCC was hyperacylated in liver isolated from SIRT4KO mice (Fig. 4B), as would be predicted in the absence of a protein deacylase. MCCC hyperacylation in SIRT4KO liver tissue was associated with a corresponding decrease in MCCC activity (Fig. 4C). To determine if SIRT4 can remove acyl-lysines on MCCC, we first immunoprecipitated MCCA from SIRT4KO mice. Next, we incubated acylated MCCC with recombinant wild-type or catalytically-inactive SIRT4 protein and found a lower acylation signal (Fig. 4D), supporting the notion that SIRT4 removes acyl-lysine modifications from MCCC.

Because the chemical modifications that SIRT4 can remove have highly similar structures (Fig. 3A), and our antibodies have moderate cross-reactivity (Fig. S3F), we performed mass spectrometry proteomic analyses to determine where and which modifications were present on MCCC. We immunoprecipitated, digested, and measured MCCC peptides with mass shifts indicating glutarylated (G; 114.03169 Da), methylglutarylated (MG; 128.047344 Da), 3-methylglutaconylated (MGc; 126.031694 Da), hydroxymethylglutarylated (HMG; 144.042259 Da), succinylated (100.016044), or acetylated (42.010565 Da) lysines. MCCA exhibited 86% sequence coverage from the set of peptides identified at 1% FDR.

Remarkably, we found several glutaryl-, MG-, MGc-, and HMG-lysines on MCCA peptides (Figs. 4E and 4F, Table S3), as well as previously identified acetyl- and succinyl-lysine sites (Hornbeck et al., 2011). Together, these data show that MCCC contains several of these new protein modifications.

To identify how these acyl modifications contribute to decreased MCCC activity in SIRT4KO mice, we first inspected more closely the sites of acylation. MCCC is a α 3- β 6- α 3 heterododecamer. The α -subunit contains three domains – a biotin carboxylase (BC) domain, a domain that mediates interactions between the α - and β -subunits (BT domain), and a biotin carboxyl carrier protein (BCCP) domain (Figs. 4F and 4G). The BC domain catalyzes the ATP-dependent carboxylation of biotin, which is located in the BCCP domain; the β -subunit catalyzes the transfer of the carboxyl group from biotin to the methylcrotonyl-CoA acceptor in the carboxyltransferase (CT) domain. Our proteomic analysis of MCCC identified acetylation sites dispersed throughout the α -subunit (Fig. 4E), consistent with previous findings (Hornbeck et al., 2011). In contrast, glutaryl-, MG-, HMG-, and MGc-lysines showed a distinct clustering in the BCCP domain. The β -subunit had nearly the same sequence coverage as the α -subunit at 85%, but significantly fewer modifications were detected on the β -subunit (Figs. 4F, Table S3).

Next, we modeled the sites of acylation onto the structure of MCCA. A high-resolution crystal structure and electron microscopy density mapping has been reported for the *Pseudomonas aeruginosa* MCCC (Huang et al., 2012). This bacterial enzyme is homologous to murine MCCC, with sequence identities of 47% and 66% for the α - and β -subunits, respectively (Sievers et al., 2011). We used these structures to build a homology model of the murine MCCC complex (Fig. 4G) and then mapped the sites of acylation onto the lysines we identified by proteomics (Fig. 4E). Surprisingly, we found that the biotinylated active site lysine (K677) was modified with glutaryl, MG, HMG, and MGc modifications (Fig. 4E). Biotinylation induces a conformational flip of K677 (Fig. 4H), and these data suggested that MCCC might have reduced biotinyl-lysine in the absence of SIRT4. To test this hypothesis, we measured biotin levels on MCCC immunoprecipitated from wild-type and SIRT4KO mouse livers. We saw no differences between total biotin levels when normalized to total MCCC protein in the SIRT4KO mouse liver samples (Fig. 4K), suggesting that lysine acylation does not influence lysine biotinylation.

Notably, we found several additional sites of acylation on MCCC, which were positioned at intramolecular interfaces. Therefore, we predicted protein acylation could affect intramolecular complex formation. The functionally active form of MCCC is an α 3- β 6- α 3 heterododecamer, which is thought to have a relatively unstable trimer of alpha subunits (Huang et al., 2012). One novel site of acylation (K66) lies directly at an α - α subunit interface (Fig. 4I). The majority of remaining sites lie within the BCCP domain, which must translocate approximately 80Å during MCCC catalysis to carry the carboxyl moiety from the BC domain to the CT domain (Huang et al., 2012). To carry out this function, the BCCP domain of the α -subunit must be inserted into the active site of a neighboring β -subunit (Figs. 4G and 4J). Notably, K655 and K683 are at the interaction interface between the α - β subunits, and K655 is predicted to form a salt bridge with E44 on the β -subunit (Fig. 4J).

Thus, we predicted a cluster of acylation in this region would alter binding of the α -subunit to the β -subunit, collectively reducing stability of the complex.

To test this directly, we monitored the migration of MCCC by blue native polyacrylamide gel electrophoresis (BN-PAGE) in wild-type and SIRT4KO mouse hepatic mitochondria. In wild-type mice, we observed a strong signal at 720 kDa (Fig. 4L), which is the predicted molecular weight of the functionally intact dodecameric MCC complex (Huang et al., 2012). However, in SIRT4KO mice, significantly less 720 kDa MCCC signal is present (Fig. 4M), despite similar total protein levels (Fig. 4M) and similar levels of total MCCA (Fig. 4N). These data demonstrate that in the absence of SIRT4, hyperacylation impairs the formation or overall stability of the MCC complex. Together, these findings support the model that SIRT4 regulates MCCC activity by influencing the amount of intact complex.

Next, we sought to determine the physiological consequence of MCCC protein hyperacylation and disrupted complex formation. MCCC is a protein in the leucine catabolic pathway; therefore, we tested whether leucine metabolism might be altered in the absence of SIRT4. To determine if SIRT4 ablation impacts leucine metabolism, we measured flux through the BCAA pathway *in situ* in intact, permeabilized liver mitochondria. We monitored the generation of NADH from α -ketoisocaproate (α KIC, the deaminated α -ketoacid of leucine) in alamethicin-permeabilized mitochondria isolated from livers of wild-type and SIRT4KO mice. Remarkably, we observed a significantly reduced rate of NADH production with α KIC as a substrate in SIRT4KO mouse mitochondria compared to wild-type controls (Fig. 5A). To determine if the defect observed in SIRT4KO liver mitochondria was specific for BCAA metabolism, we next tested for changes in nutrient flux through several other mitochondrial metabolic pathways, namely, α -ketoglutarate dehydrogenase (α KGDH) using α -ketoglutarate (α KG), glutamate dehydrogenase (GDH) using glutamate, and pyruvate dehydrogenase (PDH) using pyruvate (Fig. 5B and Fig. S5A). Interestingly, we observed a small, but significant reduction in the rate of NADH generated through α KGDH (Fig. 5B). Glutamate flux through GDH was elevated in SIRT4KO mouse mitochondria (Fig. 5B), consistent with previous reports (Haigis et al., 2006). However, we observed no differences in pyruvate metabolism (Fig. 5B), which is in contrast to a recent report (Mathias et al., 2014). The widely variable rates of NADH generation from pyruvate could be influenced by the fact that flux through hepatic PDH was the lowest of the complexes tested (Fig. S5A).

Since three different α -ketoacid substrates corresponding to the three BCAAs can drive BCKDH catabolic flux, we monitored NADH formation using the other two known substrates of BCKDH, α -ketoisovalerate (α KIV) and α -ketomethylvalerate (α KMV), in intact, permeabilized hepatic mitochondria. Consistent with our findings using α KIC as a substrate, NADH generation from α KIV and α KMV was lower in SIRT4KO mouse mitochondria compared to wild-type (Fig. 5C). Importantly, the reduction in BCAA flux could not be attributed to any changes in the amount of total BCKDH or phosphorylation status of its known regulatory phosphorylation sites (Fig. 5D). These data suggest that leucine metabolism, as well as isoleucine and valine metabolism, are altered in the absence of SIRT4. Taken together, these data clearly show that BCAA metabolism is specifically reduced by SIRT4 ablation.

Next, we measured whether the reduction in BCAA flux in the absence of SIRT4 was specific to the liver or could be generalizable to other tissues. Given the well-established role of skeletal muscle in BCAA disposal (Felig, 1975), we first collected mitochondria from wild-type mouse skeletal muscle and monitored NADH generation as described above; however, we were unable to detect NADH production in the presence of α KIC in isolated mitochondria prepared from skeletal muscle of wild-type and SIRT4KO mice (Fig. S5B). This is consistent with abundant expression of the leucine transaminase (BCATm) but low expression of BCKDH in skeletal muscle, which is the opposite ratio of expression of these enzymes in liver (Hutson et al., 1992; Newgard, 2012; Shimomura et al., 2006; Zhou et al., 2010).

In contrast to that observed in skeletal muscle, isolated mitochondria prepared from hearts revealed robust α KIC-supported NADH production in wild-type mice; therefore, we repeated the enzyme activity assays detailed above for hepatic mitochondria in cardiac mitochondria collected from wild-type and SIRT4KO mice. Consistent with liver data, we found that BCAA flux was reduced and glutamate flux was increased in the hearts of SIRT4KO mice (Fig. 5E and 5F). Flux through PDH and α KGDH was not different in cardiac mitochondria from wild-type and SIRT4KO mice (Fig. 5F).

Finally, we considered the possibility that a down-stream reduction in oxidative phosphorylation (OXPHOS) could be contributing to the alterations in substrate metabolism we observed. We performed high-resolution O_2 consumption experiments in isolated mitochondria from liver and hearts of wild-type and SIRT4KO mice to determine if mitochondrial respiratory defects were associated with SIRT4 ablation. Given that both liver and heart rely heavily on fatty acids for fuel, respiratory control within the beta-oxidation pathway was assessed first, followed by maximal respiratory flux in the presence of saturating levels of both NAD^+ - and FAD-linked substrates. Energization with the respiratory substrates octanoyl-carnitine/malate, followed by the addition of ADP revealed no differences in either state 4 or state 3 O_2 consumption (Fig. 5G and 5H). Respiratory control ratios for both liver and heart were identical between wild-type and SIRT4KO mice (Figure 5I). Subsequent additions of NAD^+ -linked glutamate and FAD-linked succinate led to comparable increases in respiration (Fig. 5G and 5H), all together demonstrating that loss of SIRT4 within liver and heart does not compromise maximal respiratory flux regardless of the electron entry point (e.g., electron transfer flavoprotein (ETF), complex I, or complex II). Together, these data show that SIRT4KO mice have intact OXPHOS function but a specific reduction in BCAA flux in mitochondria isolated from multiple tissues.

SIRT4 Regulates Leucine-Stimulated Insulin Secretion

Previous studies have shown that altered BCAA metabolism is associated with the progression of diabetes and cardiovascular disease (Newgard et al., 2009; Shah et al., 2010). Further, proper control of leucine catabolism is important for overall healthy aging (Mansfeld et al., 2015). Thus, we set out to identify physiological consequences of dysregulated leucine catabolism in SIRT4KO mice. First, we assessed SIRT4 protein expression across a variety of tissues to understand in which tissue(s) SIRT4 might be controlling leucine metabolism. We collected heart, liver, skeletal muscle, whole pancreas,

and pancreatic islets from wild-type mice (Fig. 6A). Given that mitochondrial content is widely heterogeneous across these tissues, and SIRT4 is a mitochondrial protein, we measured seven different mitochondrial proteins in each tissue lysate and normalized SIRT4 protein to the average expression of these markers (Fig. 6A), as well as to each mitochondrial protein individually (Fig. S6A). Regardless of how SIRT4 protein is normalized, its expression was highest in liver, followed by isolated islets of Langerhans. SIRT4 protein expression was lower in heart, skeletal muscle, and whole pancreas, relative to mitochondrial content of each tissue (Fig. 6A).

Since SIRT4 has been reported to have effects on insulin secretion, we focused on pancreatic islets (Ahuja et al., 2007; Haigis et al., 2006). Leucine has long been known as a potent insulin secretagogue in pancreatic islets (Sener and Malaisse, 1980). Considering the fact that our data show altered leucine metabolic flux in the absence of SIRT4, we hypothesized that SIRT4 might regulate leucine catabolism in the islet and therefore affect leucine-stimulated insulin secretion.

To test this hypothesis, we isolated pancreatic islets from wild-type and SIRT4KO mice and measured insulin secretion by islet perfusion (Fig. 6B). We found that leucine-stimulated insulin secretion was potently increased in the isolated SIRT4KO islets compared to controls. Interestingly, glucose-stimulated insulin secretion was also increased in islets isolated from SIRT4KO mice compared to wild-type islets, while glutamine- and KCl-stimulated insulin secretion were similar between SIRT4KO islets and controls in our perfusion assay. Collectively, our data from isolated islets show that SIRT4 most robustly affects glucose- and leucine-stimulated insulin secretion, and this is a direct effect on pancreatic islets.

To determine whether elevated insulin secretion also occurs *in vivo*, we challenged wild-type and SIRT4KO mice with glucose or leucine and measured insulin secretion over time. In contrast to our *ex vivo* data in isolated islets, we did not observe elevated glucose-stimulated insulin secretion in SIRT4KO mice *in vivo* until they were 8 months old (Fig. 6C–E). Interestingly, at 2 months of age, leucine-stimulated insulin secretion was similar in wild-type and SIRT4KO mice; however, while wild-type insulin levels rose and returned to baseline by 60 minutes, leucine-stimulated insulin levels in SIRT4KO mice tended to remain higher than baseline 60 minutes after the leucine gavage (Fig. 6F). This trend for sustained leucine-stimulated insulin levels in SIRT4KO mice was more pronounced at 4 months of age (Fig. 6G). Importantly, blood glucose levels were not affected by the leucine gavages (Fig. S6B). By 8–10 months of age, SIRT4KO mice had overt hyperinsulinemia, even at baseline (Fig. 6H). We also considered whether the increase in leucine-stimulated insulin secretion was caused by altered leucine uptake or clearance in SIRT4KO mice. To test this possibility, we gavaged mice with leucine and measured levels of leucine and α KIC in plasma over time (Fig. S6C). The data clearly show that circulating leucine and α KIC levels are not changed between wild-type and SIRT4KO mice at any of the ages or time-points we tested. Overall, the data demonstrate that SIRT4 affects both glucose- and leucine-stimulated insulin secretion *in vivo*, but the effects on leucine-stimulated insulin secretion precede those of glucose-stimulated insulin secretion.

Taken together, the *ex vivo* and *in vivo* data show that SIRT4 has a clear role in regulating insulin secretion in pancreatic islets. These effects are direct on pancreatic islets since leucine clearance *in vivo* is unchanged and elevated insulin secretion is observed in isolated SIRT4KO islets *ex vivo*. Importantly, the data show that the effects of SIRT4 on leucine-stimulated insulin secretion precede those on glucose-stimulated insulin secretion, suggesting that the primary defect in SIRT4KO mice centers on leucine. Collectively, our data support the model that lower leucine metabolism in SIRT4KO mice alters the fate of intracellular leucine in pancreatic islets thereby increasing insulin secretion.

Elevated Insulin Secretion in SIRT4KO Mice Drives Insulin Resistance

Finally, we investigated the overall physiological consequences of chronic increases in insulin secretion by performing an extensive analysis of glucose metabolism in SIRT4KO mice at multiple ages. When we assessed glucose tolerance in young-, middle-, and old-aged mice, we found that young (2 months old) SIRT4KO mice had normal glucose tolerance (Fig. 7A) but progressively developed glucose intolerance as they aged (Fig. 7A–C). Consistent with the development of age-related glucose intolerance in SIRT4KO mice, we also observed a progressive development of insulin resistance with age (Fig. 7D–F). At 2 months of age, SIRT4KO mice had normal insulin sensitivity (Fig. 7D); however, by 7 months of age, SIRT4KO mice developed insulin resistance (Fig. 7E), which worsened by 11 months of age (Fig. 7F).

As another marker of dysregulated glucose metabolism, we also measured fasting plasma insulin and blood glucose levels. After a mild 5–6 hour fast, SIRT4KO mice had elevated insulin levels at 2 months of age (Fig. 7G). As SIRT4KO mice aged beyond 4 months of age, they developed overt fasting hyperinsulinemia (Fig. 7G). Unlike plasma insulin levels, fasting blood glucose levels were normal at 2 months of age (Fig. 7H). Yet, as the mice aged, SIRT4KO mice developed fasting hyperglycemia compared to the wild-type controls (Fig. 7H).

Together, these data clearly show that *in vivo* fasting hyperinsulinemia is the earliest metabolic defect observed in SIRT4KO mice. Since chronic hyperinsulinemia can lead to the development of insulin resistance (Gray et al., 2010; Rajan et al., 2016), our data suggest that early hyperinsulinemia in SIRT4KO mice may be the primary defect driving accelerated age-induced insulin resistance. As a whole, our data support the notion that SIRT4 controls leucine metabolism and insulin secretion in islets and that loss of SIRT4 leads to dysregulated insulin secretion and accelerated age-induced glucose intolerance and insulin resistance.

DISCUSSION

Among the family of seven sirtuins, the primary enzymatic activity of the mitochondrial sirtuin SIRT4 has remained enigmatic. This gap in knowledge has made interpreting the role of SIRT4 in aging-related physiology difficult. Using a combination of phylogenetics and computational biology, we identified a region within the catalytic pocket of SIRT4 protein that is highly conserved and, therefore, was likely under strong evolutionary selective pressure. By modeling the structure of the protein and performing enzymatic studies on

SIRT4, we found that this region has an α -helix that coordinates and facilitates the removal of glutaryl-, MG-, HMG-, and MGc-lysine modifications.

To identify how SIRT4 and its newly discovered enzymatic activities influence metabolism, we first investigated proteins that interact with SIRT4. We and others have found that SIRT4 binds to several enzymes of the leucine oxidation pathway (Mathias et al., 2014; Wirth et al., 2013). Interestingly, our concurrent study demonstrates that reactive acyl-CoA species (RAS) have the potential to react non-enzymatically with lysine residues to generate protein modifications (Wagner et al., 2017). Indeed, during leucine oxidation, three specific reactive species are generated: methylglutaconyl-CoA (MGc-CoA) and hydroxymethyl-CoA (HMG-CoA) are directly generated, whereas methylglutaryl-CoA (MG-CoA) is generated from the chemical or enzymatic (non-specific) reduction of MGc-CoA (Roe et al., 1986). These metabolites react with lysine residues to produce acyl-lysine modifications that we identified as substrates of SIRT4-mediated deacylation. We hypothesize that RAS generated during leucine metabolism react with lysine residues on nearby proteins in the leucine metabolism pathway to inhibit their function, thus providing a negative feedback loop to reduce pathway flux. Upon activation, SIRT4 removes these modifications to restore leucine catabolism.

In support of this hypothesis, we found that in the absence of SIRT4, flux through the BCAA metabolic pathway was markedly reduced in mitochondria isolated from both liver and heart tissue. Importantly, reduced flux in the SIRT4KO mouse mitochondria was specific to the BCAA pathway, as no consistent changes between genotypes were seen in pyruvate or α KG metabolic flux. Interestingly, we found flux through GDH was elevated, in agreement with previous reports (Haigis et al., 2006). This previous study reported GDH inhibition by ADP-ribosylation, presumed to be catalyzed by SIRT4. Importantly, GDH is allosterically activated by leucine and its deamidated homologue α KIC (Allen et al., 2004; Fahien and Macdonald, 2011). Thus, in light of the data presented here, we hypothesize that elevated GDH activity in the absence of SIRT4 can be explained by lower leucine/ α KIC metabolism, leading to elevations in allosteric activators of GDH, and thus overall activity; future studies will be directed at testing this hypothesis. Overall, our data support the notion that in the absence of SIRT4, BCAA metabolism is inhibited.

We next sought to determine the overall physiological effect of ablated SIRT4 and disrupted leucine metabolism. To do this, we first determined in which tissues SIRT4 was highly expressed. Interestingly, pancreatic islets were among the highest SIRT4-expressing tissues when normalized to mitochondrial content. Leucine has long been known as a potent insulin secretagogue (Sener and Malaisse, 1980). Further, leucine and BCAA metabolism are emerging as important regulators of diabetes (Newgard, 2012), cardiovascular disease (Shah et al., 2010), and metabolic homeostasis throughout the aging process (D'Antona et al., 2010; Mansfeld et al., 2015; Martin et al., 2011). Reduced BCAA catabolism is reported in obese, diabetic *ob/ob* mice and mice rendered diabetic through a high-fat diet and low-dose streptozotocin treatment (Lian et al., 2015). As a result, we focused on characterizing glucose metabolism in SIRT4KO mice that have dysregulated leucine metabolism.

We found that pancreatic islets isolated from SIRT4KO mice had increased insulin secretion in response to leucine. Leucine is proposed to increase insulin secretion through several

different mechanisms. For example, leucine allosterically activates GDH, thereby increasing α KG flux into the TCA cycle, increasing ATP production, and stimulating insulin secretion (Li et al., 2003). Leucine can also be oxidized to generate ATP, thereby stimulating insulin secretion; however, 2-amino-bicyclo[2,2,1] heptane-2-carboxylic acid (BCH), a non-metabolizable leucine analog, can still stimulate insulin secretion by activating GDH (Fahien and Macdonald, 2011). Further, leucine still stimulates insulin secretion in mice lacking mitochondrial branched-chain aminotransferase (BCAT2), which catalyzes the first step in leucine oxidation (Zhou et al., 2010). Consequently, the major mechanism by which leucine stimulates insulin secretion has converged on allosteric activation of GDH. Given that we find decreased leucine metabolism in SIRT4KO tissues, we hypothesize that less leucine metabolism leads to more leucine available to allosterically stimulate GDH, which increases insulin secretion in SIRT4KO islets.

Similar to patients with activating mutations of GDH, SIRT4KO mice also displayed inappropriately high basal levels of insulin and a particular sensitivity to hyperinsulinemia after ingestion of leucine. Interestingly, the earliest defect we observed in SIRT4KO mice was basal hyperinsulinemia. While this phenotype was mild, previous studies have shown that chronic hyperinsulinemia can lead to insulin resistance (Coleman and Hummel, 1974; Gray et al., 2010; Lee, 1981; Rajan et al., 2016). Indeed, as SIRT4KO mice aged, the hyperinsulinemia became progressively worse, which was consistent with the development of glucose intolerance, insulin resistance, and fasting hyperglycemia. Accordingly, the International Mouse Phenotyping Consortium reported that serum fructosamine levels, a measure of long-term glucose control, are elevated in SIRT4KO mice, further supporting our observations that SIRT4KO mice have abnormal glucose homeostasis (Koscielny et al., 2014). Taken together, these data suggest that an impairment in the ability to break down leucine in SIRT4KO mice leads to enhanced leucine-stimulated insulin secretion. With age, this impairment accelerates the development of chronic hyperinsulinemia and eventually a disruption of glucose homeostasis.

Overall, the data presented here support a model where SIRT4 regulates leucine metabolism by controlling the acylation status of enzymes in the pathway, which in turn modulates the ability of proteins to form intact, active complexes. We further propose that RAS generated during leucine oxidation can react with lysine residues on nearby proteins involved with leucine metabolism to produce acyl-lysine modifications and inhibit their function (Wagner et al., 2017). The ability of SIRT4 to remove these modifications shapes the fate of leucine by regulating its flux through the leucine catabolism pathway. An alternative, but not mutually exclusive, model positions sirtuins to act as protein quality control enzymes by removing deleterious protein modifications (Wagner and Hirschey, 2014), thereby maintaining enzyme activity and metabolic flux. Indeed, our data show that SIRT4 plays an important role in maintaining quality of enzymes in the leucine metabolic pathway, and ensuring complex formation. Therefore, future studies will be directed at determining if SIRT4 plays a primary role to control metabolism and metabolic flux, if SIRT4 instead responds to protein hyperacylation in the setting of RAS to ensure protein function, or both, depending on the enzyme substrate. Overall, our studies propose a new, integrated model of how protein acylation and deacylation control metabolism, influence enzyme function and

fidelity, and open up several exciting avenues to better understand the link between sirtuins and the aging process.

STAR METHODS

CONTACT FOR REAGENT AND RESOURCE SHARING

Further information and requests for resources and reagents should be directed to and will be fulfilled by the Lead Contact, Matthew Hirsche (matthew.hirsche@duke.edu).

EXPERIMENTAL MODEL AND SUBJECT DETAILS

SIRT4-Overexpressing and Empty-Vector Stable 293T Cell Lines—The retroviral vector pBabe with a mouse SIRT4 coding region insert or without insert (empty vector control) were used to generate retrovirus. HEK293T cells (ATCC #CRL-3216, female) transduced with SIRT4 or empty vector retrovirus were selected with puromycin at 5 µg/ml to generate SIRT4-overexpressing and empty-vector control stable cell lines. The cells were maintained in DMEM with 10% fetal bovine serum. The parental retroviral vector pBabe was acquired from Dr. Chris Counter (Duke Univ Med School) and the HEK293T cells from Dr Eric Verdin (Gladstone Institute, San Francisco, CA).

Animals—SIRT4KO mice were obtained from the Jackson Laboratory (Bar Harbor, ME, stock #012756) and backcrossed for 7 generations onto a C57BL/6J background obtained from Jackson Laboratory (Bar Harbor, ME, stock #000664). These mice were then backcrossed for another 3 generations onto the C57BL/6NJ background obtained from the Jackson Laboratory (Bar Harbor, ME, stock #005304) to re-introduce a functional nucleotide transhydrogenase (*Nnt*) gene, which is missing in the commonly used C57BL/6J mice. Mice were group-housed on a 12-hour light/dark cycle with free access to water and PicoLab Rodent Diet 20 (LabDiet #5053, St. Louis, MO). Age, sex, genotype, and number of animals used per study are provided in the appropriate figure legends. Genotypes were determined using the Sirt4 F, Sirt4 R1, and Sirt4 R2 primers (sequences provided in Key Resources Table). All *in vivo* procedures were performed on healthy animals in accordance with the Duke Institutional Animal Care and Use Program.

METHOD DETAILS

Protein Alignment and Structural Predictions—To determine the putative nucleotide binding regions, protein sequences and binding regions of each of the seven human sirtuins were obtained from Uniprot (www.uniprot.org); (SIRT1, Q96EB6; SIRT2, Q8IXJ6; SIRT3, Q9NTG7; SIRT4, Q9Y6E7; SIRT5, Q9NXA8; SIRT6, Q8N6T7; SIRT7, Q9NRC8). COBALT (Papadopoulos and Agarwala, 2007) and Uniprot were used for protein alignment. To determine the predicted secondary structure of the mitochondrial sirtuins, primary protein sequences of the three mitochondrial human sirtuins were obtained from Uniprot: <http://www.uniprot.org>; [SIRT3, Q9NTG7; SIRT4, Q9Y6E7; SIRT5, Q9NXA8], and entered into the PredictProtein server: <http://predictprotein.org> (Rost and Liu, 2003); data accessed and downloaded October 2011. Alpha-helices were predicted using Helical TransMembrane Segment Rotational Angle Prediction: <http://biotechnology.tbmed.ac.ir/htmsrap/index.htm>; data accessed and downloaded December 2012.

Phylogenetic Analyses and Scoring—We downloaded all 5,869 protein sequences from Uniprot containing a significant match to the Pfam (version 27.0) SIR2 (PF02146) domain (Finn et al., 2014). We built a phylogenetic tree from the sirtuin domain portions of all of these sequences with length greater than 40 residues using the WAG-CAT model in FastTreeMP (Price et al., 2010), version 2.1.8. Fig. S1C shows the location of the seven human sirtuins in this tree. This tree, based on sirtuin-like sequences from more than 3,000 species supports the previous grouping of the human sirtuins into four classes: SIRT1-3 occupy class I, SIRT4 occupies class II, SIRT5 occupies class III, and SIRT6 and 7 occupy class IV. In addition, it supports several more recent suggestions (Greiss and Gartner, 2009), including: the relationship between SIRT2 and SIRT3 within class I, the existence of a largely fungal-specific sub-group in class I, and the great diversity of class III sirtuins. Furthermore, it suggests additional groups of sirtuins in non-human species (Fig. S1C).

To enable the identification of specific sites within SIRT4 that were likely to influence its enzymatic specificity, we subsampled the available sirtuin sequences to a set of 811 within the Pfam set of representative proteomes at 15% co-membership in UniRef50 clusters (Chen et al., 2011). We further selected a random 10% of these (including all human sirtuins), resulting in 81 sirtuins spanning the four classes. We used PROMALS3D (Pei et al., 2008) to build a 3D structure-aware alignment guided by representative structures available for human sirtuins (4IF6 A, 1J8F A, 3GLR A, 2B4Y A, 3K35 A). We further constrained PROMALS3D to respect the alignment of the alpha helical region (Fig. 1). We assigned each sirtuin in the alignment to the class of the nearest human sirtuin in a tree of these sequences generated as described above. We then applied the GroupSim algorithm (Capra and Singh, 2008) with no window to the resulting alignment (Fig. S1D) and classification of the sirtuins.

GroupSim identifies alignment columns in which the amino acid patterns respect the assignment of the proteins to classes. Columns in which the amino acids within a group are similar and different from the amino acids in other groups receive high scores. In the sirtuin alignment, SIRT4 position 103 received the highest score (Fig. S1D). The second and third highest scoring columns (229 and 228) appeared to distinguish class IV and class III from the other classes, respectively, but the fourth highest scoring column (267, near the end of the sirtuin domain) appeared to distinguish class II (predominantly S) from other classes (predominantly P). The position immediately downstream of 103 received the sixth highest score. These class II specific amino acid preferences for these positions in the alpha helix provide an evolutionary signature that suggests the importance of this region to SIRT4 activity.

Structural Analyses—All molecular modeling studies were conducted using Accelrys Discovery Studio 4.0 (Accelrys Software, Inc., San Diego, CA; <http://accelrys.com>). All crystal structure coordinates were downloaded from the protein data bank (www.pdb.org). The homology model of human SIRT4 was constructed with the MODELLER protocol (Eswar et al., 2008) using crystal structures of SIRT2, SIRT5, and SIRT6 as templates (PDB IDs: 3ZGV, 3RIY, and 3ZG6, respectively). The crystal structure coordinates of the succinylated histone H3K9 peptide co-crystallized with SIRT5 were transferred to the SIRT4 structure during the generation of the homology model. The structures of SIRT5 (3RIY) and

SIRT3 (3GLR) (Jin et al., 2009) also contain co-crystallized modified peptides that were utilized in the modeling studies. Additional modifications were built onto the Lys residue and each of the respective structures were subjected to energy minimization utilizing the conjugate gradient minimization protocol with a CHARMM forcefield (Brooks et al., 2009) and the Generalized Born implicit solvent model with simple switching (Feig et al., 2004). All minimization calculations converged to an RMS gradient of < 0.001 kcal/mol. Interaction energies were then calculated between the entire respective modified peptides and the protein structures using the implicit distance-dependent dielectric model, which represents the sum total of both Van der Waals and electrostatic interactions. Although the entirety of the modified peptides was utilized in the calculations, for clarity only the modified Lys residue is depicted in Figure 2.

SIRT4 Cloning and Recombinant Protein Expression—A cDNA library of expressed mouse liver genes was synthesized using reverse transcriptase. Since the mouse SIRT4 mRNA sequence is known (NM 001167691), 5' and 3' primers against SIRT4 untranslated regions, mouse *Sirt4* 238–259 and 1446–1427 (see Key Resources Table), respectively, were designed and used to amplify by PCR the entire *Sirt4* coding region from the cDNA library. After validation of the PCR product by DNA sequencing, the PCR product was sub-cloned into a mammalian expression vector and a FLAG-tag was engineered at the C-terminus of the SIRT4 protein. FLAG-tagged SIRT4 protein was overexpressed in 293T cells and immunoprecipitated with FLAG resin. Newly synthesized proteins destined for the mitochondria often have a targeting signal consisting of a 10–70 amino acid long peptide at the N-terminus. Often, the target signal is cleaved once targeting to the mitochondria has been completed, similar to the other mitochondrial sirtuins (Nakagawa et al., 2009; Schwer et al., 2006). By sequencing overexpressed SIRT4-FLAG protein we identified a putative mitochondrial target signal at residues 1–23 that agrees with previously published reports (Haigis et al., 2006). This information allowed us to clone a truncated version of SIRT4 that encodes the processed, mature protein (residues 24–333) into pGEX-6P1 glutathione S-transferase (GST) expression vector (GE Healthcare, #28-9546-48) for expression of a GST-SIRT4 fusion protein in bacteria. Site-specific proteolysis of the fusion protein with PreScission Protease (GE Healthcare, #27-0843-01) allowed separation of the SIRT4 protein from the GST tag. DNA encoding the processed, mature SIRT4 protein (residues 24–333) was also cloned into the pETite N-His SUMO Kan vector (Lucigen Corporation, #49003) for expression of a His SUMO-SIRT4 fusion protein in bacteria. In this case, site-specific proteolysis of the fusion protein with SUMO Express Protease (Invitrogen, #12588-018) allowed separation of the SIRT4 protein from the His-SUMO tag. Site-directed mutagenesis of SIRT4 catalytic pocket tyrosine 105 to phenylalanine and arginine 108 to glutamine (Y105F and R108Q; FQ mutant) was made using the QuikChange Mutagenesis II kit (Agilent, #200523) and mutagenic forward primer 5'-CGCCAGCGTTCTGGGCCCAAACCTTTGTG-3' and reverse primer 5'-CTCAAAGTTTTGGGCCCAAGACCGCTGGCG-3'.

Bacterial Cell Culture Conditions for Recombinant SIRT4 Protein—A starter culture (100 ml) of BL21 (DE3) pLysS bacteria expressing wild-type or HY mutant mouse GST-SIRT4 (GST-SIRT4) was started from previously made 25–40% (v/v) glycerol stocks

in LB (Miller's) Broth (growcells.com) containing 100 ug/ml ampicillin and incubated overnight at 29–30°C in an orbital shaker at 225 rpm. The pLysS component of the bacterial strain was not selected. The following day 200–400 ml cultures in LB (Miller's) Broth containing 100 ug/ml ampicillin were seeded from the starter culture at an OD600 of 0.05 and incubated at 35–37°C in an orbital shaker at 225 rpm to an OD600 of 0.6–1. The cultures were cooled in ice to at least room temperature by touch or to 22°C by measuring temperature of a control flask containing water and then induced by the addition of 0.5 mM IPTG. The induction period was approximately 16–18 hours at room temperature (typically 22–24°C) or at a precisely controlled temperature (22°C) in an orbital shaker at 225 rpm. Typically, the cultures reached an OD600 of approximately 5 during the induction period. Cells were harvested by centrifugation (7,700 × g for 10 min. at 4°C) and then re-suspended on ice in at least 15 ml of 4°C Dulbecco's PBS, pH range 7.1–7.5 (Sigma) per 400 ml bacterial culture. The centrifugation was repeated, and after decanting the supernatant, the cell pellets were stored at –80°C until needed for the subsequent protein purification.

SIRT4 Purification with Tag Cleaved—Unless otherwise noted, all steps were performed on ice with buffers cooled to 4°C. Cell pellets were thawed and re-suspended in Lysis Buffer (15 ml per 400 ml culture). Lysis Buffer consisted of Dulbecco's PBS (Sigma) with an additional 150 mM NaCl added by dissolving solid NaCl, resulting in pH ~ 7.1 at room temperature. The cell suspension was sonicated on ice for four cycles (20 sec per cycle with 2 min between cycles) using a Fisher Scientific 60 Sonic Dismembrator on a power setting of between 6–7. After sonication, Triton X-100 was added to a concentration of 1% (v/v) based on the original volume of Lysis Buffer added. The extract was then rotated end-over-end for 30 min at 4°C, followed by centrifugation (12,000 × g for 20 min. at 4°C) to isolate the soluble fraction (supernatant). The soluble fraction was collected and centrifuged again (12,000 × g for 20 min. at 4°C). In preparation for the batch affinity chromatography, Glutathione Sepharose™ 4 FastFlow resin (GE Healthcare) was equilibrated in 15 ml plastic centrifuge tubes with Lysis Buffer by washing twice with approximately 5 bed volumes. Prior to the Lysis Buffer washes, the initial bead slurry was centrifuged (500 × g for 5 min at 4°C), and the supernatant was decanted. Each wash consisted of manually re-suspending the resin by inversion, followed by centrifugation (500 × g for 5 min at 4°C) and decanting of the supernatant. A 1-ml total bed volume of resin was used for cultures 1.6L with the resin and supernatant split into volumes that fit into 50 ml plastic centrifuge tubes. After the resin was washed, it was re-suspended in 1 ml Lysis Buffer and added to the extract in the 50 ml tube. The protein was allowed to bind to the resin overnight with end-over-end rotation at 4°C. The next day the resin was pelleted by centrifugation (1500 × g for 5 min at 4°C), and the supernatant was decanted. The resin with the bound protein was washed with approximately 10–11 column volumes of Wash Buffer (Dulbecco's PBS with an additional 359 mM NaCl added, resulting in pH ~ 6.9 at room temperature). Then two additional washes of approximately 5 column volumes each of Wash Buffer were completed. Each of the three washes consisted of manually re-suspending the resin by inversion and then rotating end-over-end for 15 min at 4°C. The 1500 × g spin was repeated each time, and the supernatant was decanted. After decanting the supernatant from the third wash, the resin with bound protein was then washed twice with 10–11 column volumes each of Cleavage Buffer (50 mM Tris-HCl, pH 7.9 or 8.0 at room temperature, 150 mM NaCl, 1 mM EDTA,

0.01% (v/v) Triton X-100, 1 mM DTT). The Cleavage Buffer washes consisted of manually inverting the resin several times to re-suspend and then rotating end-over-end for 15 min at 4°C. Centrifugation (1500 × g spin for 5 min at 4°C) was performed between washes, and the supernatant was decanted. If enzyme was desired with the GST-tag removed (cleaved SIRT4) after completion of the Cleavage Buffer washes, a 4% (v/v) solution of PreScission™ Protease (GE Healthcare) in Cleavage Buffer was added to the bead pellet and then transferred to a 2-ml microfuge tube. The resin was re-suspended by inverting the tube and then rotated end-over-end overnight at 4°C. Following the overnight cleavage, the resin was pelleted by centrifugation (1500 × g for 5 min at 4°C). The supernatant containing the cleaved SIRT4 was removed, and the resin was washed with 1 ml Cleavage Buffer. The wash consisted of end-over-end rotation for 5 min at 4°C, followed by centrifugation (1500 × g for 5 min at 4°C). The resulting supernatant from the wash was decanted and combined with the first supernatant containing the cleaved SIRT4. The final cleaved SIRT4 solution was buffer exchanged and concentrated in Exchange Buffer A (20 mM Tris-HCl, pH 7.9 at room temperature, 50 mM NaCl, 1 mM CHAPSO, 5% (v/v) glycerol, 1mM DTT) or Exchange Buffer B (19.9 mM Tris-HCl, pH 8.0 at room temperature, 49.5 mM NaCl, 1 mM CHAPSO, 22.8 % (v/v) glycerol, 1 mM DTT) by performing two sequential dilutions (10–11 fold) and three concentration steps using a 10,000 MWCO Amicon® Ultra-15 concentrator. Based on buffer densities and protein solution weights, when using Exchange Buffer A the calculated resulting storage buffer was 20.3 mM Tris-HCl, pH 7.9 at room temperature, 50.9 mM NaCl, 0.0093 mM EDTA, 0.99 mM CHAPSO, 4.95% (v/v) glycerol, 0.00009% (v/v) Triton X-100, 1 mM DTT; when using Exchange Buffer B the calculated resulting storage buffer was 20.2 mM Tris-HCl, pH 8.0 at room temperature, 50.4 mM NaCl, 0.0093 mM EDTA, 0.99 mM CHAPSO, 22.6% (v/v) glycerol, 0.00009% (v/v) Triton X-100, 1 mM DTT. Protein purity was determined by SDS-PAGE, Coomassie InstantBlue™ stain, and the LI-COR Odyssey® CLx Infrared Imaging System with Image Studio software (LI-COR Biosciences). Total protein concentration was determined by the Pierce® Microplate BCA Protein Assay - Reducing Agent Compatible (Thermo Fisher Scientific) using bovine serum albumin (BSA) as a standard. Purified protein was stored at 4°C or at 4°C on ice and used as soon as possible to maintain activity for enzyme assays. Typically, the purified protein solution was an approximately 80% pure mixture of cleaved and uncleaved SIRT4 with the percentage of SIRT4 being cleaved within the range of 11–24%.

SIRT4 Purification with Tag Uncleaved—Unless otherwise noted, all steps were performed on ice with buffers cooled to 4°C. To produce purified uncleaved GST-SIRT4 after completion of the Cleavage Buffer (50 mM Tris-HCl, pH 7.9 at room temperature, 150 mM NaCl, 1 mM EDTA, 0.01% (v/v) Triton X-100, 1 mM DTT) washes, the resin was re-suspended in one column volume of Cleavage Buffer containing 10 mM glutathione and transferred to a 2-ml microfuge tube. The resin was then rotated end-over-end for 5 min at 4°C, followed by centrifugation (1500 × g for 5 min at 4°C). The resulting supernatant was decanted and saved, and then four additional elution steps were performed. After assessment of the elution fractions by SDS-PAGE, fractions containing GST-SIRT4 were combined and buffer exchanged and concentrated as described above. The Exchange Buffer A described above was used and based on buffer densities and protein solution weights, the calculated resulting storage buffer was 20.3 mM Tris-HCl, pH 7.9 at room temperature, 50.8 mM NaCl,

0.0084 mM EDTA, 0.99 mM CHAPSO, 4.96% (v/v) glycerol, 0.084 mM glutathione, 0.00008% (v/v) Triton X-100, 1 mM DTT. Protein was stored at 4°C and used as soon as possible to maintain activity for enzyme assays. Protein purity and total protein concentration was determined as described above. The uncleaved GST-SIRT4 purity was determined to be 60–65% by SDS-PAGE and the LI-COR Odyssey® CLx Infrared Imaging System with Image Studio software (LI-COR Biosciences).

Bacterial Cell Culture Conditions for Alternative Recombinant SIRT4 Protein—

A starter culture (100 ml) of BL21 (DE3) pLysS bacteria expressing wild-type or FQ mutant mouse His-SUMO-SIRT4 was started from previously made 25% (v/v) glycerol stocks in LB Broth containing 30 µg/ml kanamycin and incubated overnight at 30°C in an orbital shaker at 225 rpm. The pLysS component of the bacterial strain was not selected. The following day 400 ml cultures in LB Broth containing 30 µg/ml kanamycin were seeded from the starter culture at an OD600 of 0.05 and incubated at 30 °C in an orbital shaker at 225 rpm to an OD600 of 0.6–0.7. The cultures were cooled on ice to 18°C then induced by the addition of 0.5 mM IPTG. The induction period was 18 hours at 18°C in an orbital shaker at 225 rpm. Typically, the cultures reached an OD600 of approximately 3 during the induction period. Cells were harvested by centrifugation (7,700 × g for 10 min at 4 °C) and then re-suspended in Dulbecco's PBS, pH range 7.1–7.5 (Sigma; 60 ml total for 1.6 L culture). The centrifugation was repeated, and after decanting the supernatant, the cell pellets were stored in 50 ml plastic centrifuge tubes at –80°C until needed for the subsequent protein purification.

SIRT4-His-SUMO Purification—Unless otherwise noted, all steps were performed on ice with buffers cooled to 4°C. Buffers employed were the following:

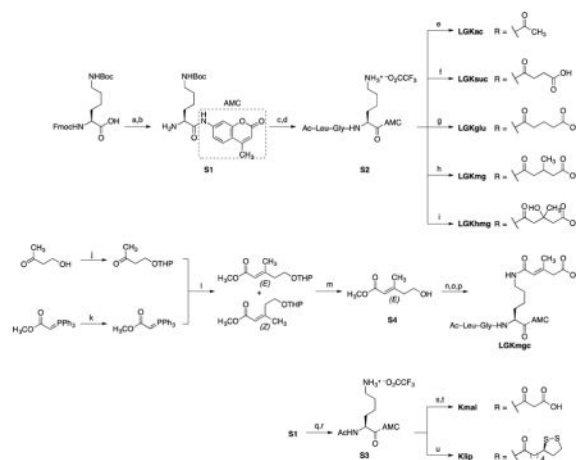
1. Buffer 1: 20 mM Tris-HCl, pH 7.5 at room temp, 50 mM NaCl, 1 mM CHAPSO, 1 mM DTT
2. Lysis Buffer: Bacterial Protein Extraction Reagent (B-PER® containing 20 mM Tris-HCl, pH 7.5, Thermo Fisher Scientific) with the addition of 20 mM imidazole, pH 7.5 at room temp, 1 mM DTT, 100U/ml Pierce™ Universal Nuclease
3. Elution Buffer: 20 mM Tris-HCl, pH 7.5 at room temp, 50 mM NaCl, 500 mM imidazole, 1 mM CHAPSO, 1 mM DTT
4. Binding Buffer 1: B-PER® containing 20 mM Tris-HCl, pH 7.5 with the addition of 20 mM imidazole, pH 7.5 at room temp, 1 mM DTT
5. Binding Buffer 2: 20 mM Tris-HCl, pH 7.5 at room temp, 50 mM NaCl, 20 mM Imidazole, 1 mM CHAPSO, 1 mM DTT
6. Wash Buffer 1: 1:1 ratio of B-PER® and additional buffer containing 20 mM Tris-HCl, pH 7.5 at room temp, 100 mM NaCl, 40 mM imidazole, 2 mM DTT
7. Wash Buffer 2: 20 mM Tris-HCl, pH 7.5 at room temp, 50 mM NaCl, 20 mM Imidazole, 1 mM CHAPSO, 1 mM DTT

8. Exchange Buffer: 20 mM Tris-HCl, pH 8.0 at room temp, 50 mM NaCl, 1 mM CHAPSO, 23% (v/v) glycerol, 1 mM DTT

Cell pellets were thawed and re-suspended in Lysis Buffer (10 ml/g of cell paste) in 50 ml centrifuge tubes. The re-suspended cells were then rotated end-over-end for 30 min at 4°C, followed by centrifugation (16,000 × g for 20 min. at 4°C) to isolate the soluble fraction (supernatant). The soluble fraction was collected and the 16,000 × g centrifugation was repeated. In preparation for batch affinity chromatography, a 0.125 ml bed volume of Ni Sepharose™ 6 FastFlow resin (GE Healthcare Life Sciences) was dispensed into 15 ml plastic centrifuge tubes. The resin was first centrifuged (500 × g for 5 min at 4°C) and the 20% ethanol supernatant was removed, followed by a wash with 5 bed volumes of water, 5 bed volumes of Elution Buffer without DTT, 10 bed volumes of Binding Buffer 1 without DTT, and 10 bed volumes of Binding Buffer 1. Each wash consisted of gently shaking the beads manually for 3 min followed by centrifugation (500 × g for 5 min at 4°C) and decanting of the supernatant. For ~8g of cell paste, the soluble fraction was split into volumes that fit into 50 ml plastic centrifuge tubes. After the beads were equilibrated with Binding Buffer 1, a 0.125 ml resin bed volume was re-suspended in 1.25 ml Binding Buffer 1 and added to the soluble fraction in the 50 ml tube. The protein was allowed to bind to the beads for 2 hr with end-over-end rotation at 4°C. The resin was pelleted by centrifugation (500 × g for 5 min at 4°C), and the supernatant was decanted. The resin with the bound protein was washed with 5 bed volumes of Wash Buffer 1. The resin from two 50 ml plastic centrifuge tubes was combined after adding Wash Buffer 1 and transferred to a 2 ml microfuge tube (now 0.25 ml resin volume). The tube was rotated end-over-end for 15 min at 4°C and then centrifuged (500 × g for 5 min at 4°C). The supernatant was removed and the beads were then washed 4 times with 5 bed volumes of Wash Buffer 2. Each wash consisted of gently re-suspending the beads manually for 3 minutes and then rotating end-over-end for 15 min at 4°C followed by centrifugation (500 × g for 5 min at 4°C) and removal of the supernatant. The protein was then eluted 4 times with 7.5 bed volumes of Elution Buffer. Each elution step consisted of gently re-suspending the beads manually and then rotating end-over-end for 15 min at 4°C followed by centrifugation (500 × g for 5 min at 4°C) and removal of the supernatant. The 4 elution fractions were combined and concentrated approximately 10-fold using a 10,000 MWCO Amicon® Ultra-15 concentrator. The concentrated sample was then diluted 17-fold with Buffer 1 to reduce the imidazole concentration to 29.4 mM. Diluted sample was concentrated approximately 23-fold using the same 10,000 MWCO Amicon® Ultra-15 concentrator. The His-SUMO tag was cleaved from the SIRT4 using 75 Units of SUMO Protease (Invitrogen) in a 0.5 ml total reaction volume (0.375 ml of concentrated SIRT4) using the 10× reaction buffers provided [500 mM Tris-HCl, pH 8.0, 2% (v/v) Igepal (NP-40), 10 mM DTT, +/- 1.5 M NaCl to achieve desired final NaCl concentration] with a final total concentration of 150 mM NaCl. The cleavage reaction was run with gentle rocking at 4°C for approximately 13 hours. The reaction was subsequently diluted with Buffer 1 to reduce the imidazole concentration to 20 mM. The protease was removed from the solution using the Ni Sepharose™ 6 FastFlow resin. A bed volume of 0.125 ml was dispensed into a 2 ml microfuge tube. The resin was first centrifuged (500 × g for 5 min at 4°C) and the 20% ethanol supernatant was removed, followed by a wash with 5 bed volumes of water, 5 bed volumes of Elution Buffer without DTT, 10 bed volumes of Binding Buffer 2 without DTT, and 10 bed volumes of Binding

Buffer 2. Each wash consisted of gently shaking the resin manually for 3 min followed by centrifugation ($500 \times g$ for 5 min at 4°C) and decanting of the supernatant. After the resin was equilibrated with Binding Buffer 2, the 0.125 ml bed volume was re-suspended in a volume of Binding Buffer 2 equal to the previously diluted cleavage reaction and added to the cleavage reaction in the 2 ml tube. The protein was allowed to bind to the resin for 2 hr with end-over-end rotation at 4°C . The resin was pelleted by centrifugation ($500 \times g$ for 5 min at 4°C), and the supernatant containing the cleaved SIRT4 was removed and saved. The resin was washed twice with 10 bed volumes of Binding Buffer 2. Each wash consisted of gently re-suspending the resin manually and then rotating end-over-end for 15 min at 4°C followed by centrifugation ($500 \times g$ for 5 min at 4°C) and removal of the supernatant. The 3 supernatants were combined and concentrated approximately 4.5-fold using a 10,000 MWCO Amicon® Ultra-15 concentrator. The sample was then diluted 10-fold with Exchange Buffer and concentrated approximately 10-fold. An additional 10-fold dilution with Exchange Buffer was performed followed by another concentration of approximately 10-fold. The calculated final buffer composition was 20 mM Tris-HCl, pH 8.0 at room temp, 50 mM NaCl, 1 mM CHAPSO, 1 mM DTT, 0.2 mM imidazole, 0.16% (v/v) Igepal (NP-40), 22.8% (v/v) glycerol. The resulting purified protein solution was stored at 4°C on ice and used as soon as possible to maintain activity for enzyme assays. Protein purity was determined by SDS-PAGE, Coomassie InstantBlue™ stain, and the LI-COR Odyssey® CLx Infrared Imaging System with Image Studio software (LI-COR Biosciences). Total protein concentration was determined by the Pierce® Microplate BCA Protein Assay - Reducing Agent Compatible (Thermo Fisher Scientific) using bovine serum albumin (BSA) as a standard. The purified protein solution was an approximately 21–27% pure mixture of total SIRT4 (cleaved and uncleaved) with approximately 68% of the SIRT4 being cleaved.

Peptide Substrate Syntheses—All modified peptide substrates were synthesized from a common unmodified intermediate (**S2**, see scheme below), as described in literature (Madsen and Olsen, 2012). The syntheses of LGKac,(Madsen and Olsen, 2012; Wegener et al., 2003), LGKsuc,(Madsen and Olsen, 2012), and Kmal (Madsen and Olsen, 2012) have been previously reported. See substrate-specific information below. Briefly, the AMC fluorophore was introduced by POCl_3 mediated coupling to Fmoc-Lys(Boc)-OH followed by mild Fmoc group deprotection which afforded intermediate **S1** in high yield. Standard peptide coupling using N,N' -diisopropylcarbodiimide and HOBt as coupling reagents, followed by removal of the Boc protection group furnished common intermediate **S2**, which could be functionalized to give LGK substrates (**LGKac**, **LGKsuc**, **LGKglu**, **LGKmg**, and **LGKhmg**). Lysine derivative **S1** was also used to prepare K substrates (**Klip** and **Kmal**). **LGKmgc** was synthesized from known methyl (*E*)-5-hydroxy-3-methylpent-2-enoate (**S4**) (White et al., 1982) by ester hydrolysis, coupling with common intermediate **S2** followed by oxidation.



All reagents and solvents were of analytical grade and used without further purification as obtained from commercial suppliers. Anhydrous solvents were obtained from a PureSolv-system (THF) or dried over molecular sieves (CH_2Cl_2 and pyridine, 4 Å; MeCN, 3 Å). Reactions were conducted under an atmosphere of argon or nitrogen whenever anhydrous solvents were used. Vacuum liquid chromatograph (VLC) was performed using silica gel 60 (particle size 0.015–0.040 mm). LC-MS analyses of synthesized compounds were performed on a Waters Acquity ultra high-performance liquid chromatography system. A linear gradient of 0% to 95% acetonitrile in water over 2.5 min or 5.2 min with constant 0.1% formic acid was applied at a flow rate of 0.6 ml/min. Compounds purified by preparative reverse-phase HPLC were purified on a C18 Phenomenex Luna column (250 mm \times 20 mm, 5 μm , 100 Å) on an Agilent 1260 LC system equipped with a diode array UV detector and an evaporative light scattering detector (ELSD), using a linear gradient of 5% to 100% acetonitrile in water at $t=5\text{--}45$ min with constant 0.1% trifluoroacetic acid applied at a flow rate of 20 ml/min. Nucleic magnetic resonance (NMR) spectra were recorded on a Bruker Avance-III HD (^1H , 600 MHz; ^{13}C , 151 MHz), Bruker Ascend-400 (^1H , 400 MHz; ^{13}C , 101 MHz) or Varian Mercury 300 (^1H , 300 MHz; ^{13}C , 75.5 MHz). Chemical shifts are reported in ppm relative to deuterated solvent as internal standard (δ_{H} : DMSO- d_6 2.50 ppm; δ_{C} : DMSO- d_6 39.52 ppm). Assignments of NMR spectra are based on correlation spectroscopy (COSY, HSQC, HMQC, and/or HMBC spectra). Accurate mass verification measurements (HRMS) were performed on a maXis G3 quadrupole time-of-flight (TOF) mass spectrometer (Bruker Daltonics, Bremen, Germany) equipped with an electrospray (ESI) source. All compounds were >95% pure as determined by HPLC and ^1H NMR analysis.

To synthesize LGKac, the title compound and the starting material (Ac-Leu-Gly-Lys-(7-amino-4-methyl-coumarin) trifluoroacetate salt, **S2**) were synthesized according to literature (Madsen and Olsen, 2012). Ac-Leu-Gly-Lys-(7-amino-4-methyl-coumarin) trifluoroacetate salt (**S2**) (49 mg) was suspended in anh CH_2Cl_2 (4 ml) and anh MeCN (3 ml) at 0 °C under N_2 . $i\text{Pr}_2\text{NEt}$ (63 mg, 488 μmol) was added followed by addition of Ac_2O (12 mg, 115 μmol). After stirring for 1 h at rt, the reaction mixture was taken up in half sat brine. The aqueous phase was extracted with CH_2Cl_2 (3 \times 20 ml) and the combined organic phase was washed with aq HCl (1 M, 2 \times 10 ml). The acidic aqueous phase was back extracted with CH_2Cl_2 (3 \times 20 ml), then 10% MeOH in CH_2Cl_2 (5 \times 20 ml). The combined organic phase

was then washed with sat aq NaHCO₃ (10 ml) and the aqueous phase back extracted with CH₂Cl₂ (3 × 20 ml). The combined organic phase was dried over MgSO₄ then evaporated to dryness and purified by HPLC, affording Ac-Leu-Gly-Lys(acetyl)-(7-amino-4-methyl-coumarin) (**LGKac**, 13 mg, 34% from Ac-Leu-Gly-Lys(Boc)-(7-amino-4-methyl-coumarin)) as a white foam. Characterization data was in agreement with the literature (Madsen and Olsen, 2012; Wegener et al., 2003). To synthesize LGKsuc, the title compound was synthesized according to the literature (Madsen and Olsen, 2012). Ac-Leu-Gly-Lys-(7-amino-4-methyl-coumarin) trifluoroacetate salt (**S2**) (50 mg) was suspended in anh CH₂Cl₂ (2 ml) and iPr₂NEt (0.1 ml) at rt under N₂. Succinic anhydride (13 mg, 133 μmol) was added, giving immediately a clear suspension. After stirring for 55 min, the reaction mixture was evaporated to dryness, and the resulting residue purified by HPLC, affording Ac-Leu-Gly-Lys(succinyl)-(7-amino-4-methyl-coumarin) (**LGKsuc**, 29 mg, 70% from Ac-Leu-Gly-Lys(Boc)-(7-amino-4-methyl-coumarin)) as a white solid. UPLC-MS *t_R* 1.47 min, *m/z* 616.5 ([M+H]⁺, C₃₀H₄₂N₅O₉⁺ Calcd 616.3). Characterization data was in agreement with the literature (Madsen and Olsen, 2012).

To synthesize LGKglu, Ac-Leu-Gly-Lys(Boc)-(7-amino-4-methyl-coumarin) (170 mg, 0.276 mmol) was dissolved in anh CH₂Cl₂ (5 ml), then TFA (5 ml) was added, and the reaction mixture stirred at rt for 2 h, then co-evaporated with MeCN:heptane (3 × 10 ml, 75:25, v/v), affording a white solid tentatively assigned as Ac-Leu-Gly-Lys-(7-amino-4-methyl-coumarin) trifluoroacetate salt (**S2**). The residue was suspended in anh CH₂Cl₂ (10 ml) and iPr₂NEt (145 μl, 0.832 mmol) at rt, then glutaric anhydride (47 mg, 0.828 mmol) was added, resulting in a gel like suspension. After stirring for 16 h at rt, the reaction mixture was concentrated to dryness, then dissolved in DMF (6 ml) and purified by prep-HPLC, affording Ac-Leu-Gly-Lys(glutaryl)-(7-amino-4-methyl-coumarin) (**LGKglu**, 117 mg, 68% from Ac-Leu-Gly-Lys(Boc)-(7-amino-4-methyl-coumarin)) as a white fluffy material. ¹H NMR (DMSO-*d*₆) δ 10.36 (s, 1H, NH_{AMC}), 8.32 (t, *J* = 5.8, 1H, NH_{gly}), 8.09 (d, *J* = 7.3, 1H, NH_{leu}), 8.01 (d, *J* = 7.6, 1H, NH_{α,lys}), 7.79 (d, *J* = 2.0, 1H, H_{8AMC}), 7.77 (t, *J* = 5.6, 1H, NH_{e,lys}), 7.72 (d, *J* = 8.7, 1H, H_{5AMC}), 7.52 (dd, *J* = 8.7, 2.1, 1H, H_{6AMC}), 6.26 (d, *J* = 1.5, 1H, H_{3AMC}), 4.37 (td, *J* = 8.3, 5.2, 1H, H_{α,lys}), 4.22 (q, *J* = 7.3, 1H, H_{α,leu}), 3.74 (m_{ABX,A}, *J* = 16.6, 5.7, 1H, H_{α,gly,A}), 3.71 (m_{ABX,B}, *J* = 16.6, 5.6, 1H, H_{α,gly,B}), 3.01 (q, *J* = 6.4, 2H, CH_{2,e,lys}), 2.39 (d, *J* = 1.3, 3H, 4_{AMC}-CH₃), 2.17 (d, *J* = 7.4, 2H, CH₂CO₂H), 2.06 (d, *J* = 7.4, 2H, NH_{e,lys}COCH₂), 1.85 (s, 3H, CH₃CO), 1.52–1.79 (m, 5H, CH_{γ,leu}, CH_{2,β,lys}, CH₂CH₂CO₂H), 1.19–1.51 (m, 6H, CH_{2,β,leu}, CH_{2,γ,lys}, CH_{2,δ,lys}), 0.88 (d, *J* = 6.5, 3H, CH_{3,leu,A}), 0.84 (d, *J* = 6.4, 3H, CH_{3,leu,B}). ¹³C NMR (DMSO-*d*₆) δ 174.2 (CO₂H), 172.9 (CO_{leu}), 171.44 (CO_{lys}/CONH_{e,lys}), 171.41 (CO_{lys}/CONH_{e,lys}), 169.8 (CH₃CO), 169.0 (CO_{gly}), 160.0 (C_{2AMC}), 153.7 (C_{8aAMC}), 153.1 (C_{4AMC}), 142.2 (C_{7AMC}), 126.0 (C_{5AMC}), 115.3 (C_{6AMC}), 115.2 (C_{4aAMC}), 112.4 (C_{3AMC}), 105.8 (C_{8AMC}), 53.6 (C_{α,lys}), 51.5 (C_{α,leu}), 42.1 (C_{α,gly}), 40.5 (C_{β,leu}), 38.3 (C_{e,lys}), 34.5 (NH_{e,lys}COCH₂), 33.1 (CH₂CO₂H), 31.4 (C_{β,lys}), 28.9 (C_{δ,lys}), 24.2 (C_{γ,leu}), 23.0 (CH_{3,leu,A}), 22.9 (C_{γ,lys}), 22.5 (CH₃CO), 21.7 (CH_{3,leu,B}), 20.7 (CH₂CH₂CO₂H), 18.0 (4_{AMC}-CH₃). UPLC-MS *t_R* 1.27 min, *m/z* 630.5 ([M+H]⁺, C₃₁H₄₄N₅O₉⁺ Calcd 630.3); HRMS *m/z* 630.3135 ([M+H]⁺, C₃₁H₄₄N₅O₉⁺ Calcd 630.3134)

To synthesize LGKmg, Ac-Leu-Gly-Lys-(7-amino-4-methyl-coumarin) trifluoroacetate salt (**S2**, 33 mg, 52 μmol) was added to a solution of 3-methylglutaric anhydride (10 mg, 78 μmol) and $i\text{Pr}_2\text{Net}$ (30 μl , 172 μmol) in anhydrous CH_2Cl_2 (1 ml) and the suspension stirred for 2 h at rt, after which the reaction mixture had turned transparent. MeOH (1 ml) was added and the reaction mixture evaporated to dryness. The resulting residue was then purified by preparative HPLC to afford desired Ac-Leu-Gly-Lys(3-methylglutaryl)-(7-amino-4-methyl-coumarin) (**LGKmg**, 29 mg, 87% from Ac-Leu-Gly-Lys(Boc)-(7-amino-4-methyl-coumarin)) as a white fluffy material. ^1H NMR (DMSO- d_6) δ 10.35 (d, J = 1.7 Hz, 1H, NH_{AMC}), 8.32 (t, J = 5.8 Hz, 1H, NH_{gly}), 8.09 (d, J = 7.3 Hz, 1H, NH_{leu}), 8.00 (d, J = 7.6 Hz, 1H, $\text{NH}_{\alpha,\text{lys}}$), 7.79 (d, J = 2.1 Hz, 1H, $\text{H}_{8\text{AMC}}$), 7.77 (t, J = 5.7 Hz, 1H, $\text{NH}_{\text{e,lys}}$), 7.71 (dd, J = 8.6, 2.0 Hz, 1H, $\text{H}_{5\text{AMC}}$), 7.52 (dd, J = 8.7, 2.0 Hz, 1H, $\text{H}_{6\text{AMC}}$), 6.25 (dt, J = 2.5, 1.3 Hz, 1H, $\text{H}_{3\text{AMC}}$), 4.41–4.35 (m, 1H, $\text{H}_{\alpha,\text{lys}}$), 4.22 (ddd, J = 9.0, 7.3, 6.1 Hz, 1H, $\text{H}_{\alpha,\text{leu}}$), 3.75 (m_{ABX,A}, J = 16.6, 5.9 Hz, 1H, $\text{H}_{\alpha,\text{gly,A}}$), 3.71 (m_{ABX,B}, J = 16.6, 5.8 Hz, 1H, $\text{H}_{\alpha,\text{gly,B}}$), 3.07–2.97 (m, 2H, $\text{CH}_{2,\text{e,lys}}$), 2.39 (d, J = 1.4 Hz, 3H, $4_{\text{AMC}}\text{-CH}_3$), 2.25–2.18 (m, 2H, $\text{H}_{3\text{MG}}$, $\text{CH}_{2,\text{A}}\text{CO}_2\text{H}$), 2.06 (dd, J = 13.8, 5.8 Hz, 1H, $\text{CH}_{2,\text{A}}\text{CONH}$), 2.04–1.98 (m, 1H, $\text{CH}_{2,\text{B}}\text{CO}_2\text{H}$), 1.92 (dd, J = 13.9, 7.8 Hz, 1H, $\text{CH}_{2,\text{B}}\text{CONH}$), 1.85 (s, 3H, CH_3CONH), 1.78–1.70 (m, 1H, $\text{H}_{\text{lys},\beta,\text{A}}$), 1.69–1.57 (m, 2H, $\text{H}_{\text{lys},\beta,\text{B}}$, $\text{H}_{\text{leu},\gamma}$), 1.50–1.42 (m, 2H, $\text{H}_{\text{leu},\beta}$), 1.42–1.36 (m, 2H, $\text{H}_{\text{lys},\delta}$), 1.36–1.30 (m, 1H, $\text{H}_{\text{lys},\gamma,\text{A}}$), 1.30–1.23 (m, 1H, $\text{H}_{\text{lys},\gamma,\text{B}}$), 0.88 (d, J = 6.6 Hz, 3H, $\text{CH}_{3,\text{leu,A}}$), 0.86–0.82 (m, 6H, $\text{CH}_{3,\text{leu,B}}$, $3_{\text{MG}}\text{-CH}_3$). ^{13}C NMR (DMSO- d_6) δ 173.6 (CO_2H), 172.9 (CO_{leu}), 171.4 (CO_{lys}), 170.8 ($\text{CONH}_{\text{e,lys}}$), 169.7 (CH_3CO), 169.0 (CO_{gly}), 160.0 ($\text{C}_{2\text{AMC}}$), 153.6 ($\text{C}_{8\text{aAMC}}$), 153.1 ($\text{C}_{4\text{AMC}}$), 142.1 ($\text{C}_{7\text{AMC}}$), 125.9 ($\text{C}_{5\text{AMC}}$), 115.3 ($\text{C}_{6\text{AMC}}$), 115.2 ($\text{C}_{4\text{aAMC}}$), 112.4 ($\text{C}_{3\text{AMC}}$), 105.8 ($\text{C}_{8\text{AMC}}$), 53.6 ($\text{C}_{\alpha,\text{lys}}$), 51.5 ($\text{C}_{\alpha,\text{leu}}$), 42.2 (CH_2CONH), 42.1 ($\text{C}_{\alpha,\text{gly}}$), 40.7 ($\text{CH}_2\text{CO}_2\text{H}$), 40.5 ($\text{C}_{\beta,\text{leu}}$), 38.2 ($\text{C}_{\text{e,lys}}$), 31.4 ($\text{C}_{\beta,\text{lys}}$), 28.8 ($\text{C}_{\delta,\text{lys}}$), 27.4 ($\text{C}_{3\text{MG}}$), 24.2 ($\text{C}_{\gamma,\text{leu}}$), 22.9 ($\text{CH}_{3,\text{leu,A}}$), 22.8 ($\text{C}_{\gamma,\text{lys}}$), 22.5 (CH_3CO), 21.6 ($\text{CH}_{3,\text{leu,B}}$), 19.4 ($3_{\text{MG}}\text{-CH}_3$), 18.0 ($4_{\text{AMC}}\text{-CH}_3$).

To synthesize LGKhmg, 3-Hydroxy-3-methyl-glutaric acid (14.9 mg, 92 μmol) was suspended in anhydrous CH_2Cl_2 (1.5 ml) at r.t., then N,N' -diisopropylcarbodiimide (13 μl , 83 μmol) was added and the reaction stirred for 2 h, affording a clear solution, to which Ac-Leu-Gly-Lys-(7-amino-4-methyl-coumarin) trifluoroacetate salt (**S2**, 51 mg, 80 μmol) and pyridine (9.0 μl , 119 μmol), resulting in a clear solution with a yellow precipitate forming. Addition of NMP (0.5 ml) resulted in a clear solution. After stirring for 22 h, pyridine (90 μl , 1.11 mmol) and a catalytic amount of 4-(N,N -dimethylamino)pyridine was added. An additional aliquot of 3-hydroxy-3-methyl-glutaric acid (15.5 mg, 96 μmol) and N,N' -diisopropylcarbodiimide (13 μl , 83 μmol) was stirred in anhydrous CH_2Cl_2 (1.5 ml) for 2 h at r.t., then added to the reaction mixture, and the reaction stirred for additional 22 h. Addition of water (0.5 ml) and DMF (0.5 ml) followed by concentration of the reaction mixture to approx 1.5 ml followed by direct purification by preparative HPLC afforded desired Ac-Leu-Gly-Lys(3-hydroxy-3-methylglutaryl)-(7-amino-4-methyl-coumarin) (**LGKhmg**, 40 mg, 76%) as a white fluffy material. ^1H NMR (400 MHz, DMSO- d_6) δ 10.37 (s, 1H, NH_{AMC}), 8.33 (t, J = 5.8, 1H, NH_{gly}), 8.10 (d, J = 7.3, 1H, NH_{leu}), 8.02 (d, J = 7.7, 1H, $\text{NH}_{\alpha,\text{lys}}$), 7.99 (t, J = 5.6, 1H, $\text{NH}_{\text{e,lys}}$), 7.81 (d, J = 2.0, 1H, $\text{H}_{8\text{AMC}}$), 7.73 (d, J = 8.7, 1H, $\text{H}_{5\text{AMC}}$), 7.54 (dd, J = 8.7, 2.1, 1H, $\text{H}_{6\text{AMC}}$), 6.28 (d, J = 1.4, 1H, $\text{H}_{3\text{AMC}}$), 4.40 (td, J = 8.1, 5.1, 1H, $\text{H}_{\alpha,\text{lys}}$), 4.24 (dt, J = 8.4, 7.1, 1H, $\text{H}_{\alpha,\text{leu}}$), 3.77 (m_{ABX,A}, J = 16.7, 5.8, 1H, $\text{H}_{\alpha,\text{gly,A}}$), 3.73 (m_{ABX,B}, J = 16.7, 5.8, 1H, $\text{H}_{\alpha,\text{gly,B}}$), 3.07 (q, J = 6.7, 2H, $\text{H}_{\text{e,lys}}$), 2.45–2.42 (m, 2H,

$\text{CH}_2\text{CO}_2\text{H}$), 2.41 (d, $J = 1.2$, 3H, $4_{\text{AMC}}\text{-CH}_3$), 2.37 (br s, 2H, NHCOCH_2), 1.87 (s, 3H, CH_3CO), 1.84–1.69 (m, 1H, $\text{H}_{\beta,\text{lys,A}}$), 1.71–1.57 (m, 2H, $\text{H}_{\gamma,\text{leu}}, \text{H}_{\beta,\text{lys,B}}$), 1.54–1.24 (m, 6H, $\text{H}_{\beta,\text{leu}}, \text{H}_{\gamma,\text{lys}}, \text{H}_{\delta,\text{lys}}$), 1.21 (s, 3H, CH_3COH), 0.90 (d, $J = 6.6$, 3H, $\text{CH}_3,\text{leu,A}$), 0.86 (d, $J = 6.5$, 3H, $\text{CH}_3,\text{leu,B}$). ^{13}C NMR (400 MHz, $\text{DMSO-}d_6$) δ 172.9 (CO_{leu}), 172.2 (CO_2H), 171.4 (CO_{lys}), 171.0 ($\text{CONH}_{\text{e,lys}}$), 169.7 (CH_3CO), 169.0 (CO_{gly}), 160.0 ($\text{C}_{2\text{AMC}}$), 153.6 ($\text{C}_{8\text{aAMC}}$), 153.0 ($\text{C}_{4\text{AMC}}$), 142.1 ($\text{C}_{7\text{AMC}}$), 125.9 ($\text{C}_{5\text{AMC}}$), 115.3 ($\text{C}_{6\text{AMC}}$), 115.1 ($\text{C}_{4\text{aAMC}}$), 112.4 ($\text{C}_{3\text{AMC}}$), 105.8 ($\text{C}_{8\text{AMC}}$), 69.4 (COH), 53.5 ($\text{C}_{\alpha,\text{lys}}$), 51.5 ($\text{C}_{\alpha,\text{leu}}$), 46.1 ($\text{CH}_2\text{CO}_2\text{H}$), 45.8 (NHCOCH_2), 42.1 ($\text{C}_{\alpha,\text{gly}}$), 40.5 ($\text{C}_{\beta,\text{leu}}$), 38.2 ($\text{C}_{\epsilon,\text{lys}}$), 31.3 ($\text{C}_{\beta,\text{lys}}$), 28.6 ($\text{C}_{\delta,\text{lys}}$), 27.3 (CH_3COH), 24.2 ($\text{C}_{\gamma,\text{leu}}$), 22.9 ($\text{CH}_3,\text{leu,A}$), 22.8 ($\text{C}_{\gamma,\text{lys}}$), 22.5 (CH_3CO), 21.6 ($\text{CH}_3,\text{leu,B}$), 18.0 ($4_{\text{AMC}}\text{-CH}_3$). HRMS m/z 682.3049 ($[\text{M}+\text{H}]^+$, $\text{C}_{32}\text{H}_{45}\text{N}_5\text{O}_{10}\text{Na}^+$ Calcd 682.3059)

To synthesize LGKmgc, methyl (*E*)-5-hydroxy-3-methylpent-2-enoate (**S4**) was first synthesized based on the method described in the literature (White et al., 1982). Methyl ester **S4** (370 mg, 2.56 mmol) was stirred vigorously in THF (20 ml) and aq LiOH (1 M, 11 ml, 11 mmol) at rt. After stirring for 44 h, the reaction mixture was concentrated to approx 10 ml, then EtOAc (25 ml) was added and the reaction mixture acidified (pH ~1) by addition of aq HCl (2 M, 6 ml). The aqueous phase was extracted with EtOAc (3×25 ml), the org. phase dried over MgSO_4 and evaporated to dryness, affording a clear oil tentatively assigned as crude (*E*)-5-hydroxy-3-methylpent-2-enoic acid (351 mg). (*E*)-5-hydroxy-3-methylpent-2-enoic acid (17 mg, 0.128 mmol) was co-evaporated with toluene (2×0.5 ml), then dissolved in anhydrous CH_2Cl_2 (1 ml) and anhydrous MeCN (1 ml). HOBt (15 mg, 0.112 mmol) and *N,N'*-diisopropylcarbodiimide (17 μl , 0.111 mmol) was added and the reaction mixture stirred for 10 min at rt. *i*Pr₂NEt (34 μl , 0.198 mmol) and Ac-Leu-Gly-Lys-(7-amino-4-methylcoumarin) trifluoroacetate salt (**S2**, 48 mg, 0.076 mmol) was added. After stirring the reaction mixture for 16 h at rt, MeOH (1 ml) was added, the reaction mixture was evaporated to dryness and the resulting residue purified by VLC (0–14% MeOH in CH_2Cl_2) to afford a white solid tentatively assigned as Ac-Leu-Gly-Lys((*E*)-5-hydroxy-3-methylpent-2-enoyl)-(7-amino-4-methylcoumarin) (47 mg, 99%). Ac-Leu-Gly-Lys((*E*)-5-hydroxy-3-methylpent-2-enoyl)-(7-amino-4-methylcoumarin) (47 mg, 0.075 mmol) was suspended in acetone (2 ml) and cooled to 0°C, then aliquots of a solution of chromium trioxide (79 mg, 0.792 mmol) in water (640 μl) and conc H_2SO_4 (80 μl) was added over 1 h until LC-MS indicated full conversion of starting material. *i*PrOH (0.2 ml) and water (1 ml) was added, immediately turning the reaction mixture green. The reaction mixture was concentrated to approx 1 ml, then extracted with EtOAc (3×3 ml). The organic phase was evaporated to dryness and the resulting residue dissolved in water–DMF (1.5 ml, 50:50 (v/v)) and purified by HPLC to afford Ac-Leu-Gly-Lys((*E*)-3-methyl-glutacon-1-yl)-AMC (**LGKmgc**, 3.6 mg, 7%) as a white fluffy material. ^1H NMR ($\text{DMSO-}d_6$) δ 10.36 (s, 1H, NH_{AMC}), 8.31 (dd, $J = 6.0, 5.8$ Hz, 1H, NH_{gly}), 8.09 (d, $J = 7.3$ Hz, 1H, NH_{leu}), 8.01 (d, $J = 7.6$ Hz, 1H, $\text{NH}_{\alpha,\text{lys}}$), 7.84 (t, $J = 5.7$ Hz, 1H, $\text{NH}_{\text{e,lys}}$), 7.79 (d, $J = 2.0$ Hz, 1H, $\text{H}_{8\text{AMC}}$), 7.71 (d, $J = 8.7$ Hz, 1H, $\text{H}_{5\text{AMC}}$), 7.52 (dd, $J = 8.7, 2.0$ Hz, 1H, $\text{H}_{6\text{AMC}}$), 6.26 (d, $J = 1.6$ Hz, 1H, $\text{H}_{3\text{AMC}}$), 5.69 (q, $J = 1.2$ Hz, 1H, $\text{H}_{2\text{-MG}}$), 4.37 (m, 1H, $\text{H}_{\alpha,\text{lys}}$), 4.22 (m, 1H, $\text{H}_{\alpha,\text{leu}}$), 3.75 ($m_{\text{ABX,A}}$, $J = 16.6, 5.8$, 1H, $\text{H}_{\alpha,\text{gly,A}}$), 3.71 ($m_{\text{ABX,B}}$, $J = 16.6, 6.0$, 1H, $\text{H}_{\alpha,\text{gly,B}}$), 3.05 (qd, $J = 6.7, 3.3$ Hz, 2H, $\text{CH}_{2,\text{e,lys}}$), 2.98 (d, $J = 1.0$ Hz, 2H, $\text{H}_{4\text{-MG}}$), 2.39 (d, $J = 1.3$ Hz, 3H, $4_{\text{AMC}}\text{-CH}_3$), 2.08 (d, $J = 1.3$ Hz, 3H, 3-MG-CH_3), 1.85 (s, 3H, CH_3CO), 1.79–1.70 (m, 1H, $\text{H}_{\text{lys},\beta,\text{A}}$), 1.70–1.63

(m, 1H, H_{lys,β,B}), 1.63–1.57 (m, 1H, H_{leu,γ}), 1.50–1.39 (m, 4H, H_{leu,β}, H_{lys,δ}), 1.39–1.31 (m, 1H, H_{lys,γ,A}), 1.31–1.22 (m, 1H, H_{lys,γ,B}), 0.88 (d, *J* = 6.6 Hz, 3H, CH_{3,leu,A}), 0.84 (d, *J* = 6.6 Hz, 3H, CH_{3,leu,B}). ¹³C NMR (DMSO-*d*₆) δ 172.9 (CO_{leu}), 171.7 (C5_{3-MG}), 171.4 (CO_{lys}), 169.7 (CH₃CO), 169.0 (CO_{gly}), 165.5 (NH_{e,lys}CO), 160.0 (C2_{AMC}), 153.6 (C8_{aAMC}), 153.1 (C4_{AMC}), 144.5 (C3_{3-MG}), 142.1 (C7_{AMC}), 125.9 (C5_{AMC}), 122.0 (C2_{3-MG}), 115.3 (C6_{AMC}), 115.1 (C4_{aAMC}), 112.3 (C3_{AMC}), 105.8 (C8_{AMC}), 53.6 (C_{α,lys}), 51.5 (C_{α,leu}), 45.4 (C4_{3-MG}), 42.0 (C_{α,gly}), 40.5 (C_{β,leu}), 38.1 (C_{e,lys}), 31.4 (C_{β,lys}), 28.8 (C_{δ,lys}), 24.2 (C_{γ,leu}), 23.0 (CH_{3,leu,A}), 22.9 (C_{γ,lys}), 22.5 (CH₃CO), 21.6 (CH_{3,leu,B}), 17.97 (3_{3-MG}-CH₃/4_{AMC}-CH₃), 17.96 (3_{3-MG}-CH₃/4_{AMC}-CH₃).

To synthesize **Kmal**, the title compound and the starting material (Ac-Lys-(7-amino-4-methyl-coumarin) trifluoroacetate salt, (**S3**) were synthesized according to the literature (Madsen and Olsen, 2012). Ac-Lys-(7-amino-4-methyl-coumarin) trifluoroacetate salt (**S3**, 102 mg) was dissolved in MeCN (1.5 ml) and iPr₂NEt (0.06 ml). Potassium monomethyl malonate (40 mg, 0.254 mmol) and HATU (92 mg, 0.241 mmol) was premixed for 10 min in MeCN (1 ml), then added to the amine. After stirring for 3 h, MeOH (2 ml) was added, then the reaction mixture adsorbed directly onto celite and purified by VLC (0–5% MeOH in CH₂Cl₂), to afford desired methylmalonate amide (44 mg, 49% from Ac-Lys(Boc)-(7-amino-4-methyl-coumarin)) as a white foam. Characterization data was in agreement with the literature (Madsen and Olsen, 2012). Methyl ester (101 mg, 0.227 mmol) was suspended in THF (1.2 ml) and aq LiOH (1.0 M, 1.2 ml), affording a clear solution after stirring for 30 sec. After 30 min, aq HCl (2M, 0.5 ml) was added followed by addition of sat aq NaHCO₃ (0.2 ml), then the reaction mixture was concentrated to approx 2 ml and purified directly by prep-HPLC, affording the desired Ac-Lys(malonyl)-(7-amino-4-methyl-coumarin) (**Kmal**, 80 mg, 81%) as a white fluffy material. Characterization data was in agreement with the literature (Madsen and Olsen, 2012).

To synthesize **Klipoyl**, (*R*)-Lipoic acid (36 mg, 175 μmol) and HOBt (26 mg, 190 μmol) was suspended in anhydrous CH₂Cl₂ (2.2 ml) at 0 °C, followed by addition of iPr₂NEt (57 μl, 327 μmol) and *N,N'*-diisopropylcarbodiimide (22 μl, 142 μmol). After stirring for 10 min, Ac-Lys-(7-amino-4-methyl-coumarin) trifluoroacetate salt (**S3**, 50 mg, 109 μmol) was added, cooling was removed, and the reaction allowed to heat at rt. After stirring for 2 h, MeOH (1 ml) was added, the reaction mixture evaporated to dryness and the resulting residue taken up in DMF (1.5 ml) and purified by prep-HPLC, to afford desired Ac-Lys((*R*)-lipoyl)-(7-amino-4-methyl-coumarin) (**Klipoyl**, 27 mg, 47%) as a white fluffy material. ¹H NMR (DMSO-*d*₆) δ 10.48 (s, 1H, NH_{AMC}), 8.20 (d, *J* = 7.6, 1H, NH_α), 7.78 (d, *J* = 2.1, 1H, H_{8AMC}), 7.74 (t, *J* = 5.7, 1H, NH_e), 7.72 (d, *J* = 8.7, 1H, H_{5AMC}), 7.49 (dd, *J* = 8.7, 2.1, 1H, H_{6AMC}), 6.26 (t, *J* = 1.2, 1H, H_{3AMC}), 4.36 (td, *J* = 8.1, 5.5, 1H, H_α), 3.57 (dq, *J* = 8.7, 6.2, 1H, CHS), 3.17 (ddd, *J* = 10.9, 6.9, 5.5, 1H, CH_{2,A}S), 3.10 (dt, *J* = 11.0, 6.8, 1H, CH_{2,B}S), 3.01 (q, *J* = 6.5, 2H, CH_{2,e}), 2.44–2.34 (m, 4H, CH(S)CH_{2,A}CH_{2,S}, 4_{AMC}-CH₃), 2.01 (t, *J* = 7.4, 2H, NHCOCH₂), 1.87 (s, 3H, CH₃CONH), 1.82 (dt, *J* = 12.7, 6.8, 1H, CH(S)CH_{2,B}CH₂S), 1.74–1.54 (m, 3H, CH₂CH₂CH_{2,A}CHSS, CH_{2,β}), 1.54–1.21 (m, 9H, CH_{2,γ}, CH_{2,δ}, CH₂CH₂CH_{2,B}CHS). ¹³C NMR (DMSO-*d*₆) δ 171.8 (CONH_e/CONH_{AMC}), 171.7 (CONH_e/CONH_{AMC}), 169.5 (CH₃CO), 160.0 (C2_{AMC}), 153.6 (C8_{aAMC}), 153.1 (C4_{AMC}), 142.2 (C7_{AMC}), 125.9 (C5_{AMC}), 115.3 (C6_{AMC}), 115.0 (C4_{aAMC}), 112.3

(C₃AMC), 105.7 (C₈AMC), 56.1 (CHS), 53.6 (C_α), 39.9 (CH(S)CH₂CH₂S), 38.12 (C_ε/CH₂S), 38.08 (C_ε/CH₂S), 35.3 (NHCOCH₂), 34.1 (CH₂CH₂CH₂CHSS), 31.5 (C_β), 28.9 (C_δ), 28.3 (NHCOCH₂CH₂CH₂), 25.1 (NHCOCH₂CH₂), 22.9 (C_γ), 22.4 (CH₃CONH), 18.0 (4_{AMC}-CH₃). UPLC-MS *t*_R 1.77 min, *m/z* 534.2 ([M+H]⁺, C₂₆H₃₆N₃O₅S₂⁺ Calcd 534.2); HRMS *m/z* 534.2086 ([M+H]⁺, C₂₆H₃₆N₃O₅S₂⁺ Calcd 534.2091)

Chemical Acylation of Bovine Serum Albumin—Bovine serum albumin (BSA), fatty acid free (Sigma #A7030) at 2 mg/ml in 0.1 M sodium bicarbonate, pH 8.0, was mixed with acetic, succinic, glutaric, 3-methylglutaric anhydride (Sigma-Aldrich #91204, #239690, #G3806, #M47809) or 3-hydroxy-3-methylglutaric anhydride (Cayman Chemical #18632) at 10-fold molar excess over BSA lysine residues to form acetyl, succinyl, glutaryl, methylglutaryl, or hydroxymethylglutaryl-BSA, respectively. The reactions were incubated at room temperature for 30 min with continuous mixing following which, 20 mM Tris-HCl, pH 8.0, was added to neutralize unreacted anhydride. BSA lysine modifications were verified by gel electrophoresis and by mass spectrometry analysis by the Duke Proteomics Core Facility.

³²P-Nicotinamide Adenine Dinucleotide Consumption Assay—Based on the method previously described (Du et al., 2011), reactions were performed in a total volume of 10 μl in 50 mM Tris-HCl, pH 8.0, 4 mM MgCl₂, 50 mM NaCl, 0.5 mM DTT, and 0.5 μCi ³²P-NAD (PerkinElmer, #NEG023, 800 Ci/mmol) in the presence of 2 μg acylated-BSA or 0.5 μg acylated-K substrate and ~1–2 μg recombinant SIRT4 protein. After a 1 h incubation at 37°C, 1.5 μl of each reaction was spotted onto a silica gel-coated thin layer chromatography plate (Sigma-Aldrich #60768) and eluted with ethanol:aqueous ammonium bicarbonate (1 M) at a ratio of 7:3. The plates were air-dried and exposed to a Kodak storage phosphorimager screen (GE Healthcare #SD230) and the signal detected using a STORM820 phosphorimager (GE Healthcare).

Fluorogenic Sirtuin Deacylase Assay for Substrate Screening—SIRT1 (aa 193–741 with N-terminal GST-tag, >64% purity), SIRT2 (aa 50–356 with C-terminal His-tag, >90% purity), SIRT3 (aa 102–399 with N-terminal GST-tag; >59% purity), SIRT4 (aa 25–314 with N-terminal GST-tag, >70% purity), SIRT6 (full length with N-terminal GST-tag, >75% purity), and SIRT7 (full length with C-terminal FLAG-tag, >48% purity) were purchased from BPS Biosciences (San Diego, CA); SIRT5 (aa 37–310 with His-tag; >95% purity) was purchased from Enzo Life Sciences (Farmingdale, NY). Purities are given by SDS-PAGE and Coomassie blue stain according to the supplier. Assay buffer was prepared as described in Biomol International product sheets BML-KI-143 [<http://www.enzolifesciences.com/BML-AK500/fluor-de-lys-hdac-fluorometric-activity-assay-kit/>] [Tris/Cl (50 mM), NaCl (137 μM), KCl (2.7 μM), MgCl₂ (1 μM), pH 8.0] with addition of BSA (1.0 mg/ml). BSA (A7030), trypsin (T1426), NAD⁺ (N7004), and nicotinamide (N3376) were from Sigma-Aldrich (Steinheim, Germany). Screening for substrate deacylation activity was performed with end-point fluorophore cleavage by trypsin. Reactions were performed in black low binding 96-well microtiter plates (Corning half area wells, flat bottom, non-binding surface, black PS), with duplicate series in each assay and each assay performed twice. Control wells without enzyme were included in each plate. All

Author Manuscript

reactions were performed in assay buffer, with appropriate concentrations of substrates obtained by dilution from 20–50 mM stock solutions in DMSO, and appropriate concentration of enzyme obtained by dilution of the stock provided by the supplier. For a final volume of 25 μ l per well, acyl substrates (50 μ M, final concentration), and NAD⁺ (500 μ M, final concentration) was added to each well, followed by a solution of sirtuin 1–7 (200 nM, final concentration). The reaction was incubated at 37 °C for 60 min, then 25 μ l of a solution of trypsin and nicotinamide (25 μ l, 5.0 mg/ml and 8 mM, respectively; final concentration 2.5 mg/ml and 4 mM, respectively) was added and the assay development was allowed to proceed for 90 min at room temperature before fluorescence analysis. All plates were analyzed using a Perkin Elmer 2300 EnSpire Multilabel Plate Reader with excitation at 360 nm and detecting emission at 460 nm. Fluorescence measurements were converted to [AMC] concentrations based on an RFU–[AMC] standard curve to afford [AMC] relative to control wells, and all data analysis was performed using GraphPad Prism.

Author Manuscript

SIRT4 Peptide Substrate Profiling—The assay was as described above with the following exceptions. NAD⁺ (N3014) and nicotinamide (72340) were from Sigma-Aldrich, and BSA (03117057001) was from Roche Diagnostics. The final concentrations of acyl substrate and NAD⁺ were 500 μ M and 3 mM, respectively. SIRT4 was prepared in our laboratory as described for the GST fusion protein in this manuscript. The estimated final concentration of total SIRT4 was 11 μ M. Each condition within an assay occasion was done in triplicate. The assay was performed in a black, 384-well, untreated plate (Nunc). After adding the acyl substrate to the plate, the plate was placed on ice while the enzyme was added. The reaction was started by the addition of NAD⁺ after which the plate was shaken for 30 sec at room temp and then placed at 37 °C with a plate lid. The total time from the NAD⁺ addition to the addition of the trypsin and nicotinamide was 60 min, and the plate was shaken again after approximately 30 min of incubation at 37 °C. The final DMSO concentration was 1.7%. After addition of the trypsin and nicotinamide, the plate was shaken for 30 sec and allowed to develop at room temp in the dark with a plate lid. A SpectraMax M2e plate reader with SoftMax Pro software (Molecular Devices) was used. Fluorescence (RFU) measurements were not converted to [AMC]. Where nicotinamide was included in the assay to test for inhibition of SIRT4, it was dissolved in assay buffer at 5 \times concentration prior to addition to the assay.

Author Manuscript

Comparison of Wild-type and FQ Mutant SIRT4 Activities—The assay for this comparison was done as described for the SIRT4 peptide substrate profiling above, except enzyme was used from the His-SUMO-SIRT4 purification as described in this manuscript. The final cleaved SIRT4 concentration was 0.28 μ M and the substrate LGK-mg-AMC was used at 50 μ M or 500 μ M. During the 60 min assay at 37 °C, the plate was covered with a lid and aluminum foil.

Author Manuscript

SIRT4-expressing and Empty Vector Stable Cell Lines—pBABE-derived plasmids with a mouse SIRT4 coding region insert or without insert (empty vector control) were used to generate retrovirus. HEK293T cells (provided by Eric Verdin, Gladstone Institute) transduced with SIRT4 or empty vector retrovirus were selected with puromycin to generate stable cell lines. The cells were maintained on DMEM with 10% fetal bovine serum.

Antibodies and Western Blotting—Commercial antibodies used are as follows: anti-MCCA from Santa Cruz (sc-271427), anti-UQCRFS1 from Abcam (ab14746), anti-SIRT4 from Sigma-Aldrich (HPA029691), anti-glutaryl-K from Cell Signaling (generous gift), anti-phospho-BCKDHe1 α from Abcam (ab200577), anti-BCKDHe1 α from Santa Cruz (sc67200), anti-citrate synthase from Origene (TA308265), and anti-total OXPHOS cocktail from Abcam (ab110413). The anti-3-methylglutaryl (MG) and hydroxymethylglutaryl (HMG) polyclonal antibodies were generated by YenZym Antibodies LLC (San Francisco, CA) using the ‘regular rabbit antibody service’. The immunogens used were MG-BSA and HMG-BSA that were made as follows: BSA (Sigma, fatty acid free, product number A7030) at 2 mg/ml in 0.1 M sodium bicarbonate, pH 8.0, was mixed with 3-methylglutaric or hydroxymethylglutaric anhydride (Sigma-Aldrich) at 10-fold molar excess over BSA lysine residues to form 3-methylglutaryl-BSA and hydroxymethylglutaryl-BSA, respectively. The reactions were incubated at room temperature for 30 min with continuous mixing and then passed over a Sephadex G-25 column (GE Healthcare #17-0851-01) to remove unreacted anhydride. The modified BSAs were then incubated with 1 M hydroxylamine, pH 7.0, for 1 h at room temperature to reverse off-site modifications. Unreacted hydroxylamine was removed from the reactions by passage over Sephadex G-25 columns (GE Healthcare #17-0851-01) and BSA MG- and HMG-lysine modifications were verified by mass spectrometry analysis by the Duke Proteomics Core Facility.

For western blotting analysis using a LI-COR, whole-cell or crude mitochondrial protein extracts were resolved by SDS-PAGE and transferred to nitrocellulose membranes. The membranes were blocked in LI-COR buffer (0.6 \times PBS, 0.25% fish gelatin; Sigma-Aldrich #G7041, 0.05% casein; Sigma-Aldrich #C3400, and 0.02% azide) for 1 h at room temperature and probed with primary antibody in LI-COR buffer/Tween (LI-COR buffer with 0.1% tween 20). After incubation with infrared dye-conjugated secondary antibodies, the blots were developed using the LI-COR Odyssey Infrared Imaging System.

For western blotting analysis using ECL, 25 μ g of protein was resolved by SDS-PAGE and transferred to Immobilon-P membranes (Thermo Fisher Scientific, #88520). The membranes were blocked in PBS block (PBS containing 5% milk) for 1 h at room temperature and probed with primary antibodies in PBS-T (PBS block containing 0.1% Tween 20). After incubation with horseradish peroxidase (HRP)-conjugated secondary antibodies in PBS-T the blots were developed using SuperSignal West Pico Chemiluminescence substrate (Thermo Fisher Scientific, #34079) and visualized with the ChemiDoc XRS System (BioRad).

Isolation of Crude Mitochondria—Freshly harvested mouse liver was rinsed in ice-cold PBS, minced with scissors in STE buffer (0.25 M sucrose, 10 mM Tris-HCl, pH 8.0, 1 mM EDTA, HALT protease inhibitor cocktail; Thermo Fisher Scientific, #78420B) 10–20 times, and homogenized in 10 volumes STE with 10–20 strokes in a chilled glass-teflon homogenizer. The homogenate was centrifuged at 700 \times g for 10 min at 4 $^{\circ}$ C and the resulting supernatant centrifuged at 7,000 \times g for 10 min at 4 $^{\circ}$ C. The pellet of the 7,000 \times g centrifugation is the mitochondrial pellet and was washed one time with STE buffer and frozen at –80 $^{\circ}$ C.

Methylcrotonyl-CoA Carboxylase Activity Assay—Mitochondria were isolated from the left lobe of freshly harvested liver of male wild-type and SIRT4KO mice as described above. Mitochondria were permeabilized by resuspending the never-frozen pellet in 0.2 ml of permeabilization buffer (105 mM K-MES, pH 7.1, 30 mM KCl, 10 mM KH₂PO₄, 5 mM MgCl₂, 0.5 mg/ml BSA, and 30 µg/ml alamethicin; Sigma-Aldrich #A5361) and incubated for 5 min on ice. 10 µl of permeabilized mitochondria were pipetted into an Eppendorf tube and the MCCC assay begun by adding 0.1 ml MCCC reaction mix (105 mM K-MES, pH 7.1, 30 mM KCl, 10 mM KH₂PO₄, 5 mM MgCl₂, 0.5 mg/ml BSA, 2 mM ATP, 0.1 mM DTT, 0.3 mM methylcrotonyl-CoA; Sigma-Aldrich #M3013, and 1 mM NaH[¹⁴C]O₃; Perkin Elmer #NEC086H). The reaction was incubated for 30 min at 37°C. The unreacted H[¹⁴C]O₃ was then removed from the reaction by adding 0.05 ml 2 N HCl and placing the Eppendorf tube with lid open in a 60°C heat block in a radiation fume hood overnight. Under these conditions, unreacted H[¹⁴C]O₃ is converted to CO₂ gas that evaporates leaving the MGC-CoA product in the aqueous phase that dries to the bottom of the tube. The next morning, 0.5 ml of water was added to the dried sediment at the bottom of the tube and left for 3 hours at room temperature. The sediment was resuspended by pipetting up and down several times and all 0.5 ml were added to scintillation cocktail for DPM determination. Negative control reactions without permeabilized mitochondria or methylcrotonyl-CoA substrate were run in parallel. Negative control activity was subtracted from that of the test reaction to obtain MCCC activity.

Methylcrotonyl-CoA Carboxylase Immunoprecipitation—Fresh crude mitochondrial pellets were resuspended in Triton X-100 lysis buffer (50 mM Tris HCl, pH 8.0, 150 mM NaCl, 0.5% Triton X-100, 2 mM EDTA, 40 mM NaF, and HALT protease inhibitor cocktail; Thermo Fisher Scientific, #78420B) and homogenized in chilled racks with a TissueLyser bead mill (Qiagen #85300) for 2 min at 30 Hz. After lysate centrifugation at 14,000 × g for 30 min to pellet insoluble material the supernatant protein concentration was determined by the BCA protein assay (Thermo Fisher Scientific, #23252). About 1 mg protein in 1 ml Triton X-100 lysis buffer was incubated end-over-end overnight at 4 °C with 20 µl Protein A/G agarose (Thermo Fisher Scientific, #20423) and anti-MCCA (Santa Cruz, sc-271427) at 1/50 dilution. The Pro A/G agarose was washed 3× with lysis buffer, 1× with lysis buffer containing no detergent, and frozen at –80 °C.

Preparation of Methylcrotonyl-CoA Carboxylase for Proteomics Analysis—After washing the MCCC IPs as described above, proteins were eluted by incubating the beads with 150 µl 0.1% TFA for 15 minutes at room temperature while rotating. Samples were centrifuged at 1000 × g for 30 sec, the supernatant collected, spiked with 30 µl 1M Tris pH 8.0, added to a filter spin column (Pierce #69705), centrifuged for 30 seconds at 1000 × g, and the flow-through saved. The agarose beads were subsequently eluted again by incubation with 150 µl of 8M-containing buffer (8 M urea in 50 mM Tris, pH 8.0, 40 mM NaCl, 2 mM MgCl₂, + 1× Complete Roche protease inhibitor tablet, 10 mM Nicotinamide, 10 µM TSA) for 15 minutes at room temperature while rotating. The beads and solution from the second elution were added to the spin column, which was centrifuged for 30 sec at 1000 × g, and the flow-through combined with that from the first elution. After the pH was verified to be ~7–8 with a pH strip, the sample was reduced with 5 mM DTT at 37°C for 30

min, cooled to RT, alkylated with 15 mM iodoacetamide for 30 min in the dark, and unreacted iodoacetamide quenched by the addition of DTT up to 15 mM for 10 min at room temperature. Following dilution to 1.5 M urea with 50 mM Tris (pH 8.0), 5 mM CaCl₂, 5 µg of sequencing-grade trypsin (Promega) was added and digestion proceeded overnight at 37°C. The samples were acidified to 0.5% TFA and desalted on a Waters 50 mg tC18 SEP-PAK SPE column (Waters, #WAT054960)—eluting once with 500 µl 25% acetonitrile/0.1% TFA and twice with 500 µl 50% acetonitrile/0.1% TFA. The 1.5 ml eluate was frozen, lyophilized, and the dried peptides were re-suspended in 12 µl 0.1% formic acid, frozen, and submitted to the Duke University School of Medicine Proteomics Core facility for analysis by nLC-MS/MS described below.

Methylcrotonyl-CoA Carboxylase Analysis by Mass Spectrometry—Proteomic analysis was performed using a nano-Acquity UPLC system (Waters) coupled to a *Q Exactive Plus* Hybrid Quadrupole-Orbitrap mass spectrometer (Thermo Fisher Scientific) via a nanoelectrospray ionization source. For each injection, the sample was first trapped on a Symmetry C18 20 mm × 180 µm trapping column (5 µl/min at 99.9/0.1 v/v water/acetonitrile), after which the analytical separation was performed using a 1.7 µm Acquity BEH130 C18 75 µm × 250 mm column (Waters Corp.) over a gradient of 3 to 30% acetonitrile (total run time 235 min) in 0.1% formic acid at a flow rate of 400 nanoliters/minute (nL/min) with a column temperature of 55°C. The mass spectrometer was operated in data-dependent acquisition (DDA) collecting MS/MS spectra for the top 10 ions with a charge greater than 1. MS¹ (precursor) analysis was performed at 70,000 resolution, with an AGC target of 1×10⁶ ions and a maximum injection time of 60 ms. Tandem mass spectra (MS/MS) were collected in a data-dependent manner on the top 10 most abundant precursor ions per MS¹ scan, with dynamic exclusion enabled for a window of 20 seconds. Precursor ions were filtered with a 2.0 m/z isolation window and fragmented with a normalized collision energy of 27. MS² scans were performed at 17,500 resolution, with an AGC target of 5 × 10⁴ ions and a maximum injection time of 60 ms.

LC-MS/MS Data Processing—Raw LC-MS/MS data were processed in Proteome Discoverer v2.1, service pack 1 (PD2.1 SP1, Thermo Fisher Scientific), using the Byonic search engine as a node (Protein Metrics, Inc.). Data were searched against the UniProt mouse complete proteome database of reviewed (Swiss-Prot) and unreviewed (TrEMBL) proteins, which consisted of 51,414 sequences on the date of download (6/23/2016). Seven (all set as “common”) variable modifications included oxidation (M), and acylation of lysine with the following monoisotopic additions to K in parentheses: hydroxymethylglutarylation (HMG, 144.0422587348 Da), 3-methylglutaconyl (MGc, 126.0316941 Da), methylglutaryl (MG, 128.047344 Da), glutaryl (114.0316941 Da), acetyl (42.010565 Da), and succinyl (100.016044 Da). Fixed modification of carbamidomethyl (C) was selected. Data were searched with a 10 ppm precursor mass and 20 ppm product ion tolerance. The maximum number of missed cleavages was set at 4 and enzyme specificity was trypsin. Peptide spectral matches (PSMs) were filtered to a 1% false discovery rate (FDR) in PDv2.1 based on the target-decoy search results from Byonic. Site localization probabilities were determined using the ptmRS node of PDv2.1. PSMs were grouped to peptides maintaining 1%FDR at the peptide level and peptides were grouped to proteins using the rules of strict

parsimony. Proteins were filtered to 1% FDR using the Protein FDR Validator node of PD2.1.

Methylcrotonyl-CoA Carboxylase Modeling—All computational modeling was performed using Accelrys Discovery Studio 4.5 (Biovia, Inc., San Diego, CA). The crystal structure coordinates for the *P. aeruginosa* MCCC complex (Huang et al., 2012) was downloaded from the Protein Data Bank (www.pdb.org; PDB ID: 3U9S). Using this structure as a template, mouse homology models of the alpha (48% identity, 63% similarity) and beta (66% identity, 83% similarity) subunits were generated using the MODELLER protocol (Eswar et al., 2008). Each mouse subunit was superimposed over the corresponding subunits in the crystal structure template by sequence alignment and the resulting complex typed with the CHARMM forcefield (Brooks et al., 2009) and energy minimized with the smart minimizer protocol using the Generalized-Born with simple switching implicit solvent model (Feig et al., 2004) to an RMS convergence <0.01 kcal/mol. Figures were rendered using Lightwave 2015.3 (Lightwave3D Group, Burbank, CA).

Native Protein-Complex Preparation—Crude mitochondrial pellets were isolated from freshly harvested mouse liver as described above, flash frozen, and stored at -80°C . Mitochondrial extracts containing non-denatured native protein complexes were prepared using NativePAGE Sample Prep Kit (Invitrogen, #BN2008). Crude mitochondrial pellets were thawed on ice before extraction. Proteins were solubilized in 1× NativePAGE sample buffer containing 5% DDM (n-dodecyl-b-D-maltoside), at a protein concentration of 10–50 mg/ml, by pipetting up and down and by inversion. After 15 min on ice the lysates were centrifuged for 30 min at $14,000 \times g$ and the supernatants stored at -80°C .

Blue Native Polyacrylamide Gel Electrophoresis—Mitochondrial native protein extracts (25 μg protein per lane) were resolved by PAGE using the Native PAGE Novex Bis-Tris Gel System (Invitrogen, #BN2008). Immediately before PAGE coomassie G-250 additive was added to the mitochondrial extracts at a final concentration of 1.25%. 4–16% Polyacrylamide gradient gels (Invitrogen, #BN2111) were run at 200V for 3h. Protein from the gels was transferred to PVDF membranes for immunoblotting following the standard ECL western blotting protocol.

Detection of Biotinylated Methylcrotonyl-CoA Carboxylase subunit A—Protein extracts or immunoprecipitates containing MCCA were resolved by PAGE and transferred to nitrocellulose membranes. The membranes were incubated with streptavidin-AlexaFluor 680 (Thermo Fisher Scientific, #S32358) at a dilution of 1/2000 in LI-COR buffer/Tween for 1 h, washed, and the signal imaged and quantified using the LI-COR Odyssey Infrared Imaging System.

Mitochondrial Substrate Oxidation Assays—Mitochondria were isolated from liver, heart and/or skeletal muscle of SIRT4KO or WT mice, as previously described (Frezza et al., 2007). Briefly, mitochondria were isolated from liver, heart and/or skeletal muscle of SIRT4KO or WT mice via differential centrifugation. Tissues were minced in ice-cold mitochondrial isolation buffer (KCl 100mM, MOPS 50mM, EGTA 1mM, MgSO_4 5mM, pH=7.1) and washed once with the same buffer. Skeletal muscle and heart tissues were pre-

treated with bacterial proteinase (0.5mg/ml; Sigma: P8038) for 2 minutes on ice prior to homogenization. Tissues were homogenized in mitochondrial isolation buffer, supplemented with 0.2% BSA using glass/teflon Potter Elvehjem homogenizers. Homogenate was centrifuged at $500 \times G$ for 10 minutes at 4°C . The supernatant was then centrifuged at $9,000 \times G$ for 10 minutes at 4°C . Mitochondrial pellets were washed once in mitochondrial isolation buffer without BSA and again pelleted at $9,000 \times G$ for 10 minutes at 4°C . Final pellets were resuspended in mitochondrial isolation buffer without BSA and protein content was determined using the Pierce BCA protein assay.

All substrate oxidation assays were performed in a 96-well plate using a potassium-based respiration buffer (105 mM K-MES, 30 mM KCl, 10 mM KH_2PO_4 , 5 mM MgCl_2 , 0.5 mg/ml BSA, pH 7.1), supplemented with thiamine pyrophosphate (0.3 mM), coenzyme A (0.1 mM), rotenone (0.005 mM), oxidized nicotinamide adenine dinucleotide (2 mM) and alamethicin (0.03 mg/ml). Mitochondria were added to the assay buffer at a concentration of 0.15 mg/ml and the suspension was incubated at room temperature for 5 minutes to allow adequate permeabilization of the inner mitochondrial membrane by alamethicin (Gostimskaya et al., 2003). Substrates and/or drugs were added directly to their respective wells during this incubation period at the following concentrations: 5 mM pyruvate, 10 mM 2-ketoglutarate, 10 mM glutamate, 1 mM ketoisocaproate, 1 mM ketoisovalerate, 1 mM ketomethylvalerate, 0.2 mM isovaleryl-CoA, 0.1 mM BT2. To initiate the assay, 200 μl of assay suspension was added to each well and NADH fluorescence (excitation/emission, 340/460) was monitored for 10 minutes using a temperature-controlled spectrofluorometer. All assays were performed at 37°C . The linear portions of each trace were used to calculate rates of NADH production and data were presented as a percentage of the WT slope.

High-resolution O_2 consumption measurements were conducted at 37°C in potassium-based respiration buffer (K-MES 105mM, KCl 30mM, KH_2PO_4 10mM, MgCl_2 5mM, BSA 0.5mg/ml, pH=7.1), using the OROBOROS O_2K Oxygraph. For experiments involving heart mitochondria, respiration buffer was supplemented with creatine monohydrate (25mM). Hexokinase (1U/ml) and glucose (5mM) were included in all assays in an effort to clamp extramitochondrial ADP at 1mM (Clark et al., 1997). To begin, mitochondria (0.025mg/ml heart, 0.1mg/ml liver) were added to the respiration chamber in the absence of energizing substrates. The following substrates were then added sequentially: octanoyl-carnitine/malate (Oct/M; 0.2/2mM), ADP (D; 1mM), glutamate (G; 10mM) and succinate (S; 10mM). Cytochrome C (0.01mM) was added last to assess the intactness of the inner mitochondrial membrane.

Islet Perfusion—Mouse islet isolations and perfusions were performed as described (Campbell et al., 2016). The pancreas was inflated via the pancreatic duct with collagenase type V (0.8 mg per ml from Sigma-Aldrich, #C9263), excised, and digested for 10–15 minutes at 37°C . The digest was washed with cold RPMI (containing 2 mM L-glutamine, 10 mM glucose, 0.25% BSA, 100 U/ml penicillin, and 100 $\mu\text{g}/\text{ml}$ streptomycin), and the then islets were separated using a Histopaque gradient (Sigma-Aldrich, #10771 and #11191). Individual islets were handpicked and then cultured in RPMI 1640 with 10% FBS and penicillin/streptomycin overnight. Prior to perfusion, islets were equilibrated for one hour with Krebs-Ringer buffer containing 2.7 mM glucose. Islets were washed with Krebs-Ringer

buffer containing 2.7 mM glucose in between nutrient stimulations. Stimulatory glutamine was from Thermo Fisher Scientific (#25030081) and L-leucine was from Sigma-Aldrich (#61819). Perifusate was collected in 1 minute intervals and assayed for insulin by radioimmunoassay (Millipore, RI-13K).

Mouse Physiology—Fasting insulin and glucose measurements were made after a 5–6 hour fast beginning at 8:30 am. Nutrient-stimulated insulin secretion was measured by fasting the mice for 5–6 hours and then orally gavaging them with 1.5 mg/g glucose or 0.3 mg/g L-leucine. Blood samples were subsequently collected via saphenous vein using heparinized capillary tubes and centrifuged at 4600 RCF for 9 minutes at 4°C to obtain plasma. Plasma was assayed for insulin using the Stellux Rodent Insulin ELISA (Alpco, #80-INSMR-CH01). Insulin tolerance tests were performed by intraperitoneally injecting the mice with 1.0–1.4 U/kg insulin (Lilly, Humulin R U-100) following a 5–6 hour fast and then blood glucose levels were measured using a NovaMax glucometer (Nova Biomedical).

Plasma Leucine and a-Ketoisocaproate Measurements—50 µl of plasma containing internal standards L-leucine-d3 (CDN Isotopes, D-1973) and L-isoleucine-13C6 (Cambridge Isotope Laboratories, CLM-2248-H-PK) was precipitated with methanol, the supernatants were dried down under N₂, and reconstituted in 0.1% formic acid in water. Leu and Ile were analyzed on a Waters Xevo TQ-S triple quadrupole mass spectrometer coupled to a Waters Acquity UPLC system. The analytical column (Waters Acquity UPLC HSS T3 Column, 1.8 µm, 2.1 × 100 mm) was used at 30°C, 10 µl of the sample was injected onto the column, and eluted at a flow rate of 0.3 ml/min. The gradient began with 100% eluent A (0.1% formic acid in water) and was then programmed as follows: 0 to 2 min - 0% eluent B (95:5 acetonitrile-water, 0.1% formic acid); 2 to 10 min - gradient to 40% eluent B; 10 to 11 min - gradient to 100% eluent B; 11 to 13 min hold at 100% eluent B; 13.0 to 13.5 min gradient to 0% eluent B; 13.5 to 15.5 min hold at 100% eluent A to re-equilibrate the column. Mass transitions of m/z 132.1 → 86.1 for Leu and Ile, 135.1 → 89.2 for L-leucine-d3, and 138.1 → 91.2 for L-isoleucine-13C6 were monitored in a positive ion electrospray ionization mode with the following parameters: capillary voltage 2,000 V, cone voltage 14 V, and collision energy 15 V. Separate quantitation of Leu and Ile from raw multiple reaction monitoring data was performed using Waters TargetLynx Quantitative Analysis.

Plasma αKIC was measured as previously described (Glynn et al., 2015; Olson et al., 2013). 30 µl of plasma containing internal standard KIC-d3 (Cambridge Isotope Laboratories, DLM-1944) was precipitated with 150 µl of 3M PCA. 200 µl of 25 M o-phenylenediamine (OPD) in 3M HCl was added to the supernatants and the samples were incubated at 80°C for 20 minutes. KIC was extracted with ethyl acetate as previously described (Olson et al., 2013). The extracts were dried under nitrogen, reconstituted in 200 mM ammonium acetate and analyzed on a Waters Xevo TQ-S triple quadrupole mass spectrometer coupled to a Waters Acquity UPLC system. The analytical column (Waters Acquity UPLC BEH C18 Column, 1.7 µm, 2.1 × 50 mm) was used at 30°C, 10 µl of the sample was injected onto the column, and eluted at a flow rate of 0.4 ml/min. The gradient began with 45% eluent A (5 mM ammonium acetate in water) and was then programmed as follows: 0 to 2 min - 55% eluent B (methanol); 2 to 2.5 min - gradient to 95% eluent B; 2.5 to 3.2 min - hold at 95%

eluent B, return to 45% A and re-equilibrate the column for 1 minute. Mass transitions of m/z 203 \rightarrow 161 for KIC and 206 \rightarrow 161 for KIC-d3 were monitored in a positive ion electrospray ionization mode.

QUANTIFICATION AND STATISTICAL ANALYSIS

All statistical tests, exact values of n , what n represents, definitions of center, dispersion, and precision, and definitions of significance are indicated in the figure legends. Box plots depict the interquartile range with whiskers plotted to the min and max values. The horizontal line within the box is the median value and the “+” is the mean value. Statistical tests were performed using GraphPad Prism. Z-scores were calculated using the equation $Z=(n\text{-mean})/\text{standard deviation}$. Heatmaps were generated using Plotly (www.plot.ly).

DATA AND SOFTWARE AVAILABILITY

Proteomic datasets used to define the SIRT4 interactome (Table S2) and identify methylcrotonyl-CoA carboxylase acylation sites (Table S3) are available as supplemental files. The mass spectrometry proteomics data have been deposited to the ProteomeXchange Consortium via the PRIDE (Vizcaino et al., 2016) partner repository with the dataset identifier PXD005896.

KEY RESOURCES TABLE

REAGENT or RESOURCE	SOURCE	IDENTIFIER
Antibodies		
Rabbit polyclonal anti-3-methylglutaryl-K	This paper; YenZym Antibodies LLC 'regular rabbit antibody service'	N/A
Rabbit polyclonal anti-hydroxymethylglutaryl-K	Wagner et al 2017; YenZym Antibodies LLC 'regular rabbit antibody service'	N/A
Rabbit polyclonal anti-glutaryl-K	Cell Signaling Technology	14943MF
Rabbit polyclonal anti-SIRT4	Sigma-Aldrich	HPA029691
Mouse monoclonal UQCRFS1	Abcam	ab14746
Mouse monoclonal anti-MCCA (A-4)	Santa Cruz Biotechnology	sc271427
Rabbit polyclonal anti-pBCKDHe1 α	Abcam	ab200577
Rabbit polyclonal anti-BCKDHe1 α	Santa Cruz Biotechnology	sc67200
Rabbit polyclonal anti-citrate synthase	Origene	TA308265
Mouse monoclonal anti-total OXPHOS cocktail	Abcam Inc.	ab110413
Bacterial and Virus Strains		
BL21 (DE3) pLysS Competent Cells	Promega	L119B
Biological Samples		

REAGENT or RESOURCE	SOURCE	IDENTIFIER
Chemicals, Peptides, and Recombinant Proteins		
BSA, fatty acid free	Sigma-Aldrich	A7030
Acetic anhydride	Sigma-Aldrich	91204
Succinic anhydride	Sigma-Aldrich	239690
Glutaric anhydride	Sigma-Aldrich	G3806
3-methylglutaric anhydride	Sigma-Aldrich	M47809
3-hydroxy-3-methylglutaric anhydride	Cayman Chemical	18632
Acetyl-BSA	This paper	N/A
Succinyl-BSA	This paper	N/A
Glutaryl-BSA	This paper	N/A
Methylglutaryl-BSA	This paper	N/A
Hydroxymethylglutaryl-BSA	This paper	N/A
NAD, [adenylate-32P]	Perkin Elmer	NEG023
Pierce Protein A/G Agarose	Thermo Fisher Scientific	20423
Streptavidin Alexa Fluor 680	Thermo Fisher Scientific	S32358
Methylcrotonyl coenzyme A lithium salt	Sigma-Aldrich	M3013
H[14C]O ₃ , sodium bicarbonate	Perkin Elmer	NEC086H
LB (Miller's) Broth	Growcells.com	MBPE-1020
Ampicillin sodium salt	Sigma-Aldrich	A9518
Isopropyl-B-D-thiogalactopyranoside (IPTG), dioxane-free	Thermo Fisher Scientific	BP1755-10
Dulbecco's Phosphate Buffer Saline (PBS)	Sigma-Aldrich	D8537
Trizma® base	Sigma-Aldrich	T1503
DL-Dithiothreitol (DTT)	Sigma-Aldrich	D5545
PreScission™ Protease	GE Healthcare	27-0843-01
CHAPSO (3-([3-Cholamidopropyl]dimethylammonio)-2-hydroxy-1-propanesulfonate)	Sigma-Aldrich	C3649
Glutathione	Sigma-Aldrich	G-4251
Glutathione Sepharose™ 4 Fast Flow	GE Healthcare	17-5132-01
Kanamycin sulfate	Sigma-Aldrich	K4000
Bovine Serum Albumin (BSA), protein assay standard	Thermo Fisher Scientific	23209
B-PER® Bacterial Protein Extraction Reagent	Thermo Fisher Scientific	90084
Imidazole	Sigma-Aldrich	792527
Pierce™ Universal Nuclease for Cell Lysis	Thermo Fisher Scientific	88701
Ni Sepharose™ 6 Fast Flow	GE Healthcare Life Sciences	17-5318-01
SUMO Protease	Invitrogen	12588-018
IGEPAL® CA-630	Sigma-Aldrich	I-3021
SIRT4 Wild-type (produced with N-terminal GST tag)	This paper	N/A
SIRT4 HY Mutant (produced with N-terminal GST tag)	This paper	N/A
SIRT4 Wild-type (produced with N-terminal His-SUMO tag)	This paper	N/A

REAGENT or RESOURCE	SOURCE	IDENTIFIER
SIRT4 FQ Mutant (produced with N-terminal His-SUMO tag)	This paper	N/A
SIRT1 (aa 193-741 with N-terminal GST-tag)	BPS Biosciences	50012
SIRT2 (aa 50-356 with C-terminal His-tag)	BPS Biosciences	50013
SIRT3 (aa 102-399 with N-terminal GST-tag)	BPS Biosciences	50014
SIRT4 (aa 25-314 with N-terminal GST-tag)	BPS Biosciences	50015
SIRT5 (aa 37-310 with His-tag)	Enzo Life Sciences	SE555
SIRT6 (full length with N-terminal GST-tag)	BPS Biosciences	50017
SIRT7 (full length with C-terminal FLAG-tag)	BPS Biosciences	50018
AMC (7-amino-4-methyl-coumarin)	Chem-Impex Int'l Inc	02029
Trypsin from bovine pancreas, TPCK treated	Sigma-Aldrich	T1426
Nicotinamide	Sigma-Aldrich	72340
Nicotinamide	Sigma-Aldrich	N3376
Beta-NAD ⁺ (nicotinamide adenine dinucleotide hydrate)	Sigma-Aldrich	N7004
Beta-NAD ⁺ (nicotinamide adenine dinucleotide hydrate)	Sigma-Aldrich	N3014
BSA (Bovine Serum Albumin, Fraction V, heat shock, fatty acid free)	Roche Diagnostics	03 117 057 001
InstantBlue™ Ultrafast Protein Stain (Coomassie)	Sigma-Aldrich	ISB1L-1L
Humulin R U-100	Lilly	0002-8215-17
Collagenase	Sigma-Aldrich	C9263
Histopaque-1077	Sigma-Aldrich	10771
Histopaque-1119	Sigma-Aldrich	11191
Glutamine	Thermo Fisher Scientific	25030081
L-leucine	Sigma-Aldrich	61819
Critical Commercial Assays		
Rat Insulin RIA	EMD Millipore	RI-13K
Stellux Chemi Rodent Insulin ELISA	Alpco	80-INSMR-CH01
Pierce® Microplate BCA Protein Assay - Reducing Agent Compatible	Thermo Fisher Scientific	23252
Fish Gelatin	Sigma-Aldrich	G7041
Casein	Sigma-Aldrich	C3400
HALT protease inhibitor cocktail	Thermo Fisher Scientific	78420B
Alamethicin	Sigma-Aldrich	A5361
SuperSignal West Pico Chemiluminescent Substrate	Thermo Fisher Scientific	34079
Deposited Data		
Proteomic dataset used to identify methylcrotonyl-CoA carboxylase acylation sites	ProteomeXchange	PXD005896
Experimental Models: Cell Lines		
Human HEK293T stable mSIRT4 overexpressing	This paper	N/A
Human HEK293T stable empty vector control	This paper	N/A
Human HEK293T	Dr Eric Verdin, Gladstone Institute	N/A

REAGENT or RESOURCE	SOURCE	IDENTIFIER
Experimental Models: Organisms/Strains		
Mouse: 129-Sirt4tm1Fwa/J	Jackson Laboratory	012756
Mouse: C57BL/6J	Jackson Laboratory	000664
Mouse: C57BL/6NJ	Jackson Laboratory	005304
Oligonucleotides		
mSIRT4 YR to FQ Forward: 5'-CGCCAGCGTTCTGGGCCCAAACTTTGTG-3'	Custom-made by Integrated DNA Technologies	N/A
mSIRT4 YR to FQ Reverse: 5'-CTCAAAGTTTGGGCCCAGAACCGCTGGCG-3'	Custom-made by Integrated DNA Technologies	N/A
Sirt4 F: 5'-GTCTGTCTAGCTTCCTCACTG-3'	Custom-made by Integrated DNA Technologies	N/A
Sirt4 R1: 5'-TAAAGATAGTTGTAAGTCACC-3'	Custom-made by Integrated DNA Technologies	N/A
Sirt4 R2: 5'-AGAGCCCAGTGTGCTGGGTTG-3'	Custom-made by Integrated DNA Technologies	N/A
mSirt4 238-259: 5'-CCAGACAGAATAAGAATGAGCG-3'	Custom-made by Integrated DNA Technologies	N/A
mSirt4 1446-1427: 5'-TTCTGCCTGGTCTCTTCC-3'	Custom-made by Integrated DNA Technologies	N/A
Recombinant DNA		
GST-mSIRT4	This paper	N/A
pGEX-6P1	GE Healthcare	28-9546-48
N-His-SUMO-mSIRT4	This paper	N/A
N-His-SUMO-mSIRT4 FQ	This paper	N/A
pETite N-His SUMO Kan	Lucigen	49003
pBabe-mSIRT4	This paper	N/A
pBabe	Dr Chris Counter, Duke Univ Med Center	N/A
Software and Algorithms		
GraphPad Prism	GraphPad Software	N/A
SoftMax Pro 6.5	Molecular Devices	N/A
Image Studio Ver 3.0.12 and Ver 3.1.4	LI-COR Biosciences	N/A
Other		
Immobilon-P membrane	Millipore	IPVH00010
Sephadex G-25	GE Healthcare	17-0851-01
NativePAGE 4-16% Bis Tris gels	Invitrogen	BN2111

REAGENT or RESOURCE	SOURCE	IDENTIFIER
NativePAGE Sample Prep Kit	Invitrogen	BN2008
QuikChange Mutagenesis II Kit	Agilent	200523
LI-COR Odyssey® CLx Infrared Imaging System	LI-COR Biosciences	N/A
SpectraMax M2e plate reader	Molecular Devices	N/A
2300 EnSpire Multilabel Plate Reader, software version 4.10.3005.1440	Perkin Elmer	N/A
Amicon® Ultra-15 10Kconcentrator	Millipore	UFC901024
Thin layer chromatography plates, silica gel-coated	Sigma-Aldrich	60768
Kodak storage phosphorimager screen	GE Healthcare	SD230
TissuLyser Bead Mill	Qiagen	85300
ChemiDoc XRS System	BioRad	N/A
STORM820 Phosphorimager	GE Healthcare	N/A
96-well half area assay plate, flat bottom, non-binding surface, black PS	Corning	3686
384-well, Black, Non-treated Microtiter Plate	Nunc	262260

Supplementary Material

Refer to Web version on PubMed Central for supplementary material.

Acknowledgments

We would like to thank Xiaoke (Betty) Hu and James D. Johnson at the University of British Columbia, Vancouver for early assistance and advice with islet perfusions; Feng Yan, Dennis Goldfarb, Michael (Ben) Major at the University of North Carolina at Chapel Hill for the interactome studies; Rami Najjar and Cell Signaling Technology for the glutaryl-lysine antibody; Zhihong Lin at Duke University for technical assistance with animal experiments; and the entire Hirschey lab for feedback. We would also like to acknowledge funding support from the American Heart Association grants 12SDG8840004 and 12IRG9010008 (MDH), The Ellison Medical Foundation (MDH), the National Institutes of Health and the NIA grant R01AG045351 (MDH), and the Duke Pepper Older Americans Independence Center (OAIC) Program in Aging Research supported by the National Institute of Aging (P30AG028716-01). FKH was supported by an American Diabetes Association/Canadian Diabetes Association Post-doctoral Fellowship (PF-3-13-4342-FH); KFW is supported by a Ruth L. Kirschstein National Research Service Award F32 Postdoctoral Fellowship (1F32DK105665-01A1). JDD and GRW are supported by an NIH/NIDDK training grant to Duke University Department of Endocrinology, Metabolism and Nutrition (2T32-DK007012-36A1); BSP is supported by R24DK085610; ASM is supported by a Sapere Aude grant from the Danish Independent Research Council–Technology and Production Sciences (12-132328); MFG was supported by a postdoctoral fellowship on an NIH/NCI training grant to Duke University (CA059365-19). CAO thanks the Lundbeck Foundation for the Group Leader Fellowship (R52-2010-5054), the Carlsberg Foundation (2011-01-0169, 2013-01-0333, CF15-011), and the Novo Nordisk Foundation (NNF15OC0017334). RMS was supported by an NIH/NEI training grant to Vanderbilt University (T32-EY021453). Computational simulations were conducted at the University of Colorado Computational Chemistry and Biology Core Facility, which is funded in part by NIH/NCATS Colorado CTSI Grant UL1TR001082. DMM is supported by a NIH/NIDDK grant (2R01DK089312). The funding sources had no role in the conduct or presentation of this research.

References

- Ahuja N, Schwer B, Carobbio S, Waltregny D, North BJ, Castronovo V, Maechler P, Verdin E. Regulation of insulin secretion by SIRT4, a mitochondrial ADP-ribosyltransferase. *J Biol Chem.* 2007; 282:33583–33592. [PubMed: 17715127]
- Allen A, Kwagh J, Fang J, Stanley CA, Smith TJ. Evolution of glutamate dehydrogenase regulation of insulin homeostasis is an example of molecular exaptation. *Biochemistry.* 2004; 43:14431–14443. [PubMed: 15533048]

- Anderson KA, Green MF, Huynh FK, Wagner GR, Hirschey MD. SnapShot: Mammalian Sirtuins. *Cell*. 2014; 159:956–956. e951. [PubMed: 25417168]
- Brooks BR, Brooks CL 3rd, Mackerell AD Jr, Nilsson L, Petrella RJ, Roux B, Won Y, Archontis G, Bartels C, Boresch S, et al. CHARMM: the biomolecular simulation program. *J Comput Chem*. 2009; 30:1545–1614. [PubMed: 19444816]
- Campbell JE, Ussher JR, Mulvihill EE, Kolic J, Baggio LL, Cao X, Liu Y, Lamont BJ, Morii T, Streutker CJ, et al. TCF1 links GIPR signaling to the control of beta cell function and survival. *Nat Med*. 2016; 22:84–90. [PubMed: 26642437]
- Capra JA, Singh M. Characterization and prediction of residues determining protein functional specificity. *Bioinformatics*. 2008; 24:1473–1480. [PubMed: 18450811]
- Chen C, Natale DA, Finn RD, Huang H, Zhang J, Wu CH, Mazumder R. Representative proteomes: a stable, scalable and unbiased proteome set for sequence analysis and functional annotation. *PLoS One*. 2011; 6:e18910. [PubMed: 21556138]
- Clark JF, Kuznetsov AV, Radda GK. ADP-regenerating enzyme systems in mitochondria of guinea pig myometrium and heart. *Am J Physiol*. 1997; 272:C399–404. [PubMed: 9124281]
- Coleman DL, Hummel KP. Hyperinsulinemia in pre-weaning diabetes (db) mice. *Diabetologia*. 1974; 10(Suppl):607–610. [PubMed: 4448328]
- Csibi A, Fendt SM, Li C, Poulgiannis G, Choo AY, Chapski DJ, Jeong SM, Dempsey JM, Parkhitko A, Morrison T, et al. The mTORC1 pathway stimulates glutamine metabolism and cell proliferation by repressing SIRT4. *Cell*. 2013; 153:840–854. [PubMed: 23663782]
- D'Antona G, Ragni M, Cardile A, Tedesco L, Dossena M, Bruttini F, Caliaro F, Corsetti G, Bottinelli R, Carruba MO, et al. Branched-chain amino acid supplementation promotes survival and supports cardiac and skeletal muscle mitochondrial biogenesis in middle-aged mice. *Cell Metab*. 2010; 12:362–372. [PubMed: 20889128]
- Du J, Jiang H, Lin H. Investigating the ADP-ribosyltransferase activity of sirtuins with NAD analogues and 32P-NAD. *Biochemistry*. 2009; 48:2878–2890. [PubMed: 19220062]
- Du J, Zhou Y, Su X, Yu JJ, Khan S, Jiang H, Kim J, Woo J, Kim JH, Choi BH, et al. Sirt5 is a NAD-dependent protein lysine demalonylase and desuccinylase. *Science*. 2011; 334:806–809. [PubMed: 22076378]
- Eswar N, Eramian D, Webb B, Shen MY, Sali A. Protein structure modeling with MODELLER. *Methods Mol Biol*. 2008; 426:145–159. [PubMed: 18542861]
- Fahien LA, Macdonald MJ. The complex mechanism of glutamate dehydrogenase in insulin secretion. *Diabetes*. 2011; 60:2450–2454. [PubMed: 21948999]
- Feig M, Onufriev A, Lee MS, Im W, Case DA, Brooks CL 3rd. Performance comparison of generalized born and Poisson methods in the calculation of electrostatic solvation energies for protein structures. *J Comput Chem*. 2004; 25:265–284. [PubMed: 14648625]
- Feldman JL, Baeza J, Denu JM. Activation of the protein deacetylase SIRT6 by long-chain fatty acids and widespread deacylation by mammalian sirtuins. *The Journal of biological chemistry*. 2013; 288:31350–31356. [PubMed: 24052263]
- Felig P. Amino acid metabolism in man. *Annu Rev Biochem*. 1975; 44:933–955. [PubMed: 1094924]
- Finn RD, Bateman A, Clements J, Coggill P, Eberhardt RY, Eddy SR, Heger A, Hetherington K, Holm L, Mistry J, et al. Pfam: the protein families database. *Nucleic Acids Res*. 2014; 42:D222–230. [PubMed: 24288371]
- Frezza C, Cipolat S, Scorrano L. Organelle isolation: functional mitochondria from mouse liver, muscle and cultured fibroblasts. *Nat Protoc*. 2007; 2:287–295. [PubMed: 17406588]
- Frye RA. Phylogenetic classification of prokaryotic and eukaryotic Sir2-like proteins. *Biochemical and Biophysical Research Communications*. 2000; 273:793–798. [PubMed: 10873683]
- Gostimskaya IS, Grivennikova VG, Zharova TV, Bakeeva LE, Vinogradov AD. In situ assay of the intramitochondrial enzymes: use of alamethicin for permeabilization of mitochondria. *Anal Biochem*. 2003; 313:46–52. [PubMed: 12576057]
- Gray SL, Donald C, Jetha A, Covey SD, Kieffer TJ. Hyperinsulinemia precedes insulin resistance in mice lacking pancreatic beta-cell leptin signaling. *Endocrinology*. 2010; 151:4178–4186. [PubMed: 20631001]

- Greiss S, Gartner A. Sirtuin/Sir2 phylogeny, evolutionary considerations and structural conservation. *Mol Cells*. 2009; 28:407–415. [PubMed: 19936627]
- Haigis MC, Mostoslavsky R, Haigis KM, Fahie K, Christodoulou DC, Murphy AJ, Valenzuela DM, Yancopoulos GD, Karow M, Blander G, et al. SIRT4 inhibits glutamate dehydrogenase and opposes the effects of calorie restriction in pancreatic beta cells. *Cell*. 2006; 126:941–954. [PubMed: 16959573]
- Hall JA, Dominy JE, Lee Y, Puigserver P. The sirtuin family's role in aging and age-associated pathologies. *J Clin Invest*. 2013; 123:973–979. [PubMed: 23454760]
- Hirschev MD. Old Enzymes, New Tricks: Sirtuins Are NAD(+)-Dependent De-acylases. *Cell Metabolism*. 2011; 14:718–719. [PubMed: 22100408]
- Ho L, Titus AS, Banerjee KK, George S, Lin W, Deota S, Saha AK, Nakamura K, Gut P, Verdin E, et al. SIRT4 regulates ATP homeostasis and mediates a retrograde signaling via AMPK. *Aging (Albany NY)*. 2013; 5:835–849. [PubMed: 24296486]
- Hornbeck PV, Kornhauser JM, Tkachev S, Zhang B, Skrzypek E, Murray B, Latham V, Sullivan M. PhosphoSitePlus: a comprehensive resource for investigating the structure and function of experimentally determined post-translational modifications in man and mouse. *Nucleic Acids Research*. 2011; 40:D261–D270. [PubMed: 22135298]
- Houtkooper RH, Pirinen E, Auwerx J. Sirtuins as regulators of metabolism and healthspan. *Nat Rev Mol Cell Biol*. 2012; 13:225–238. [PubMed: 22395773]
- Huang CS, Ge P, Zhou ZH, Tong L. An unanticipated architecture of the 750-kDa alpha6beta6 holoenzyme of 3-methylcrotonyl-CoA carboxylase. *Nature*. 2012; 481:219–223.
- Hutson SM, Wallin R, Hall TR. Identification of mitochondrial branched chain aminotransferase and its isoforms in rat tissues. *J Biol Chem*. 1992; 267:15681–15686. [PubMed: 1639805]
- Imai S, Armstrong CM, Kaerberlein M, Guarente L. Transcriptional silencing and longevity protein Sir2 is an NAD-dependent histone deacetylase. *Nature*. 2000; 403:795–800. [PubMed: 10693811]
- Jeong SM, Lee A, Lee J, Haigis MC. SIRT4 protein suppresses tumor formation in genetic models of Myc-induced B cell lymphoma. *The Journal of biological chemistry*. 2014; 289:4135–4144. [PubMed: 24368766]
- Jeong SM, Xiao C, Finley LW, Lahusen T, Souza AL, Pierce K, Li YH, Wang X, Laurent G, German NJ, et al. SIRT4 has tumor-suppressive activity and regulates the cellular metabolic response to DNA damage by inhibiting mitochondrial glutamine metabolism. *Cancer Cell*. 2013; 23:450–463. [PubMed: 23562301]
- Jiang H, Khan S, Wang Y, Charron G, He B, Sebastian C, Du J, Kim R, Ge E, Mostoslavsky R, et al. SIRT6 regulates TNF-alpha secretion through hydrolysis of long-chain fatty acyl lysine. *Nature*. 2013; 496:110–113. [PubMed: 23552949]
- Jin L, Wei W, Jiang Y, Peng H, Cai J, Mao C, Dai H, Choy W, Bemis JE, Jirousek MR, et al. Crystal structures of human SIRT3 displaying substrate-induced conformational changes. *J Biol Chem*. 2009; 284:24394–24405. [PubMed: 19535340]
- Koscielny G, Yaikhom G, Iyer V, Meehan TF, Morgan H, Atienza-Herrero J, Blake A, Chen CK, Easty R, Di Fenza A, et al. The International Mouse Phenotyping Consortium Web Portal, a unified point of access for knockout mice and related phenotyping data. *Nucleic Acids Res*. 2014; 42:D802–809. [PubMed: 24194600]
- Laurent G, de Boer VC, Finley LW, Sweeney M, Lu H, Schug TT, Cen Y, Jeong SM, Li X, Sauve AA, et al. SIRT4 represses peroxisome proliferator-activated receptor alpha activity to suppress hepatic fat oxidation. *Molecular and cellular biology*. 2013a; 33:4552–4561. [PubMed: 24043310]
- Laurent G, German NJ, Saha AK, de Boer VCJ, Davies M, Koves TR, Dephoure N, Fischer F, Boanca G, Vaitheesvaran B, et al. SIRT4 Coordinates the Balance between Lipid Synthesis and Catabolism by Repressing Malonyl CoA Decarboxylase. *Molecular cell*. 2013b; 50:686–698. [PubMed: 23746352]
- Lee S. Effects of diazoxide on insulin secretion and metabolic efficiency in the db/db mouse. *Life Sci*. 1981; 28:1829–1840. [PubMed: 7017329]
- Li C, Najafi H, Daikhin Y, Nissim IB, Collins HW, Yudkoff M, Matschinsky FM, Stanley CA. Regulation of leucine-stimulated insulin secretion and glutamine metabolism in isolated rat islets. *J Biol Chem*. 2003; 278:2853–2858. [PubMed: 12444083]

- Lian K, Du C, Liu Y, Zhu D, Yan W, Zhang H, Hong Z, Liu P, Zhang L, Pei H, et al. Impaired adiponectin signaling contributes to disturbed catabolism of branched-chain amino acids in diabetic mice. *Diabetes*. 2015; 64:49–59. [PubMed: 25071024]
- Madsen AS, Andersen C, Daoud M, Anderson KA, Laursen JS, Chakladar S, Huynh FK, Colaco AR, Backos DS, Fristrup P, et al. Investigating the Sensitivity of NAD⁺-dependent Sirtuin Deacetylation Activities to NADH. *The Journal of biological chemistry*. 2016; 291:7128–7141. [PubMed: 26861872]
- Madsen AS, Olsen CA. Substrates for efficient fluorometric screening employing the NAD-dependent sirtuin 5 lysine deacylase (KDAC) enzyme. *J Med Chem*. 2012; 55:5582–5590. [PubMed: 22583019]
- Mansfeld J, Urban N, Priebe S, Groth M, Frahm C, Hartmann N, Gebauer J, Ravichandran M, Dommaschk A, Schmeisser S, et al. Branched-chain amino acid catabolism is a conserved regulator of physiological ageing. *Nature communications*. 2015; 6:10043.
- Marcotte PA, Richardson PL, Guo J, Barrett LW, Xu N, Gunasekera A, Glaser KB. Fluorescence assay of SIRT protein deacetylases using an acetylated peptide substrate and a secondary trypsin reaction. *Anal Biochem*. 2004; 332:90–99. [PubMed: 15301953]
- Martin FP, Spanier B, Collino S, Montoliu I, Kolmeder C, Giesbertz P, Affolter M, Kussmann M, Daniel H, Kochhar S, et al. Metabotyping of *Caenorhabditis elegans* and their culture media revealed unique metabolic phenotypes associated to amino acid deficiency and insulin-like signaling. *J Proteome Res*. 2011; 10:990–1003. [PubMed: 21275419]
- Mathias RA, Greco TM, Oberstein A, Budayeva HG, Chakrabarti R, Rowland EA, Kang Y, Shenk T, Cristea IM. Sirtuin 4 is a lipoamidase regulating pyruvate dehydrogenase complex activity. *Cell*. 2014; 159:1615–1625. [PubMed: 25525879]
- Michishita E, McCord RA, Berber E, Kioi M, Padilla-Nash H, Damian M, Cheung P, Kusumoto R, Kawahara TL, Barrett JC, et al. SIRT6 is a histone H3 lysine 9 deacetylase that modulates telomeric chromatin. *Nature*. 2008; 452:492–496. [PubMed: 18337721]
- Min J, Landry J, Sternglanz R, Xu RM. Crystal structure of a SIR2 homolog-NAD complex. *Cell*. 2001; 105:269–279. [PubMed: 11336676]
- Miyo M, Yamamoto H, Konno M, Colvin H, Nishida N, Koseki J, Kawamoto K, Ogawa H, Hamabe A, Uemura M, et al. Tumour-suppressive function of SIRT4 in human colorectal cancer. *British journal of cancer*. 2015; 113:492–499. [PubMed: 26086877]
- Mostoslavsky R, Chua KF, Lombard DB, Pang WW, Fischer MR, Gellon L, Liu P, Mostoslavsky G, Franco S, Murphy MM, et al. Genomic instability and aging-like phenotype in the absence of mammalian SIRT6. *Cell*. 2006; 124:315–329. [PubMed: 16439206]
- Nakagawa T, Lomb DJ, Haigis MC, Guarente L. SIRT5 Deacetylates carbamoyl phosphate synthetase 1 and regulates the urea cycle. *Cell*. 2009; 137:560–570. [PubMed: 19410549]
- Nasrin N, Wu X, Fortier E, Feng Y, Bare OC, Chen S, Ren X, Wu Z, Streeper RS, Bordone L. SIRT4 regulates fatty acid oxidation and mitochondrial gene expression in liver and muscle cells. *The Journal of biological chemistry*. 2010
- Newgard CB. Interplay between lipids and branched-chain amino acids in development of insulin resistance. *Cell Metab*. 2012; 15:606–614. [PubMed: 22560213]
- Newgard CB, An J, Bain JR, Muehlbauer MJ, Stevens RD, Lien LF, Haqq AM, Shah SH, Arlotto M, Slentz CA, et al. A branched-chain amino acid-related metabolic signature that differentiates obese and lean humans and contributes to insulin resistance. *Cell Metabolism*. 2009; 9:311–326. [PubMed: 19356713]
- Papadopoulos JS, Agarwala R. COBALT: constraint-based alignment tool for multiple protein sequences. *Bioinformatics*. 2007; 23:1073–1079. [PubMed: 17332019]
- Pei J, Kim BH, Grishin NV. PROMALS3D: a tool for multiple protein sequence and structure alignments. *Nucleic Acids Res*. 2008; 36:2295–2300. [PubMed: 18287115]
- Peng C, Lu Z, Xie Z, Cheng Z, Chen Y, Tan M, Luo H, Zhang Y, He W, Yang K, et al. The first identification of lysine malonylation substrates and its regulatory enzyme. *Molecular & cellular proteomics : MCP*. 2011; 10:M111012658.
- Price MN, Dehal PS, Arkin AP. FastTree 2--approximately maximum-likelihood trees for large alignments. *PLoS One*. 2010; 5:e9490. [PubMed: 20224823]

- Rajan S, Shankar K, Beg M, Varshney S, Gupta A, Srivastava A, Kumar D, Mishra RK, Hussain Z, Gayen JR, et al. Chronic hyperinsulinemia reduces insulin sensitivity and metabolic functions of brown adipocyte. *J Endocrinol.* 2016; 230:275–290. [PubMed: 27340034]
- Roe CR, Millington DS, Maltby DA. Identification of 3-methylglutaryl-carnitine. A new diagnostic metabolite of 3-hydroxy-3-methylglutaryl-coenzyme A lyase deficiency. *J Clin Invest.* 1986; 77:1391–1394. [PubMed: 3958190]
- Rost B, Liu J. The PredictProtein server. *Nucleic Acids Res.* 2003; 31:3300–3304. [PubMed: 12824312]
- Schuetz A, Min J, Antoshenko T, Wang CL, Allali-Hassani A, Dong A, Loppnau P, Vedadi M, Bochkarev A, Sternglanz R, et al. Structural basis of inhibition of the human NAD⁺-dependent deacetylase SIRT5 by suramin. *Structure.* 2007; 15:377–389. [PubMed: 17355872]
- Schwer B, Bunkenborg J, Verdin RO, Andersen JS, Verdin E. Reversible lysine acetylation controls the activity of the mitochondrial enzyme acetyl-CoA synthetase 2. *Proc Natl Acad Sci U S A.* 2006; 103:10224–10229. [PubMed: 16788062]
- Sener A, Malaisse WJ. L-leucine and a nonmetabolized analogue activate pancreatic islet glutamate dehydrogenase. *Nature.* 1980; 288:187–189. [PubMed: 7001252]
- Shah SH, Bain JR, Muehlbauer MJ, Stevens RD, Crosslin DR, Haynes C, Dungan J, Newby LK, Hauser ER, Ginsburg GS, et al. Association of a peripheral blood metabolic profile with coronary artery disease and risk of subsequent cardiovascular events. *Circulation Cardiovascular genetics.* 2010; 3:207–214. [PubMed: 20173117]
- Shimomura Y, Honda T, Shiraki M, Murakami T, Sato J, Kobayashi H, Mawatari K, Obayashi M, Harris RA. Branched-chain amino acid catabolism in exercise and liver disease. *J Nutr.* 2006; 136:250S–253S. [PubMed: 16365092]
- Sievers F, Wilm A, Dineen D, Gibson TJ, Karplus K, Li W, Lopez R, McWilliam H, Remmert M, Soding J, et al. Fast, scalable generation of high-quality protein multiple sequence alignments using Clustal Omega. *Molecular systems biology.* 2011; 7:539. [PubMed: 21988835]
- Tan M, Peng C, Anderson KA, Chhoy P, Xie Z, Dai L, Park JS, Chen Y, Huang H, Zhang Y, et al. Lysine Glutarylation Is a Protein Post-translational Modification Regulated by SIRT5. *Cell Metab.* 2014; 19:605–617. [PubMed: 24703693]
- Tanny JC, Dowd GJ, Huang J, Hilz H, Moazed D. An enzymatic activity in the yeast Sir2 protein that is essential for gene silencing. *Cell.* 1999; 99:735–745. [PubMed: 10619427]
- Verdin E, Dequiedt F, Fischle W, Frye R, Marshall B, North B. Measurement of mammalian histone deacetylase activity. *Methods in enzymology.* 2004; 377:180–196. [PubMed: 14979025]
- Vizcaino JA, Csordas A, Del-Toro N, Dianas JA, Griss J, Lavidas I, Mayer G, Perez-Riverol Y, Reisinger F, Ternent T, et al. 2016 update of the PRIDE database and its related tools. *Nucleic acids research.* 2016; 44:11033. [PubMed: 27683222]
- Wagner GR, Bhatt DP, O'Connell TM, Thompson JW, Dubois LG, Backos DS, Yang H, Mitchell GA, Ilkayeva OR, Stevens RD, et al. A class of reactive acyl-CoA species reveals the nonenzymatic origins of protein acylation. 2017 Submitted.
- Wagner GR, Hirshey MD. Nonenzymatic protein acylation as a carbon stress regulated by sirtuin deacylases. *Molecular cell.* 2014; 54:5–16. [PubMed: 24725594]
- Wagner GR, Payne RM. Widespread and enzyme-independent N{epsilon}-acetylation and N{epsilon}-succinylation in the chemical conditions of the mitochondrial matrix. *Journal of Biological Chemistry.* 2013
- Wegener D, Wirsching F, Riester D, Schwienhorst A. A fluorogenic histone deacetylase assay well suited for high-throughput activity screening. *Chem Biol.* 2003; 10:61–68. [PubMed: 12573699]
- White JD, Carter JP, Kezar HS. Stereoselective synthesis of the macrocycle segment of verrucarin. *J Org Chem.* 1982; 47:929–932.
- Wirth M, Karaca S, Wenzel D, Ho L, Tishkoff D, Lombard DB, Verdin E, Urlaub H, Jedrusik-Bode M, Fischle W. Mitochondrial SIRT4-type proteins in *Caenorhabditis elegans* and mammals interact with pyruvate carboxylase and other acetylated biotin-dependent carboxylases. *Mitochondrion.* 2013; 13:705–720. [PubMed: 23438705]

- Wishart DS, Jewison T, Guo AC, Wilson M, Knox C, Liu Y, Djoumbou Y, Mandal R, Aziat F, Dong E, et al. HMDB 3.0--The Human Metabolome Database in 2013. *Nucleic Acids Res.* 2013; 41:D801–807. [PubMed: 23161693]
- Zhou Y, Jetton TL, Goshorn S, Lynch CJ, She P. Transamination is required for {alpha}-ketoisocaproate but not leucine to stimulate insulin secretion. *J Biol Chem.* 2010; 285:33718–33726. [PubMed: 20736162]
- Zhu A, Su X, Lin H. Detecting sirtuin-catalyzed deacylation reactions using (3)(2)P-labeled NAD and thin-layer chromatography. *Methods Mol Biol.* 2013; 1077:179–189. [PubMed: 24014407]

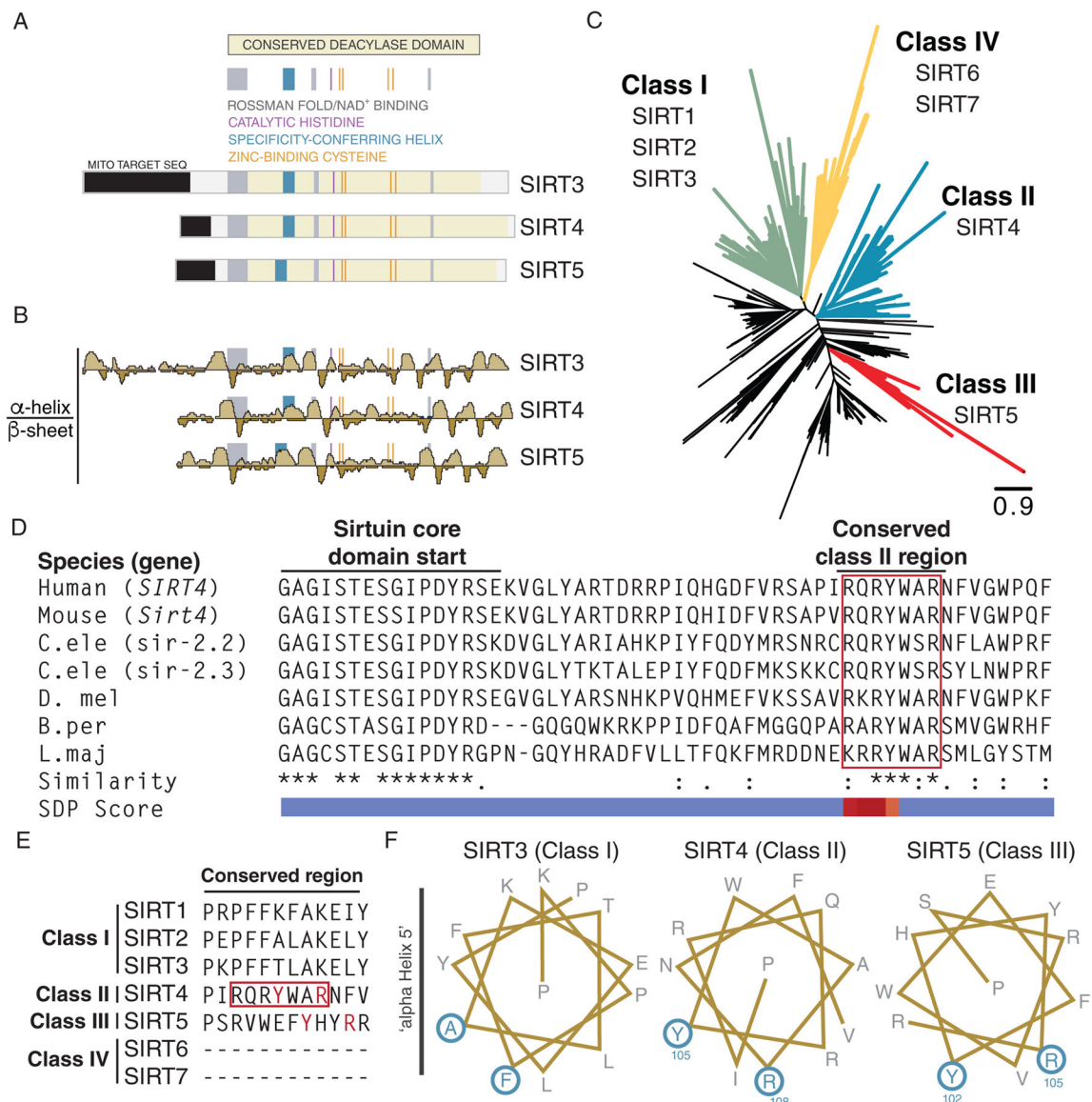


Figure 1. Phylogenetic and Evolutionary Analyses of SIRT4 (See also Figure S1)

(A) Primary sequence analyses and alignment of the three mitochondrial sirtuins SIRT3, SIRT4, and SIRT5 showing locations of amino acids important for mitochondrial localization, NAD⁺ binding, catalysis, substrate specificity, and Zn²⁺ binding. (B) Secondary structure analyses of the three mitochondrial sirtuins aligned with (A), showing predicted α -helices (above the axis) and β -sheets (below the axis). (C) Unrooted phylogenetic tree of species containing sirtuin-like genes, showing class I–IV groupings and the corresponding mammalian sirtuins; scale: 0.9 substitutions/site. (D) Regions of conserved (: and .) and identical (*) amino acids within the primary sequence of select class II sirtuins; z-score heatmap (–2.0 to 2.0) of specificity determining position (SDP) scores. (E) Same conserved sequence from (D) compared to other sirtuin classes; (–) non-conserved amino acids. (F) α -helical wheel prediction of conserved region in class I, II, and III sirtuins; ‘P’ indicates

proline at start of helix, cyan indicates highly conserved amino acids from (D), and other conserved amino acids within the same region of SIRT3 and SIRT5.

Author Manuscript

Author Manuscript

Author Manuscript

Author Manuscript

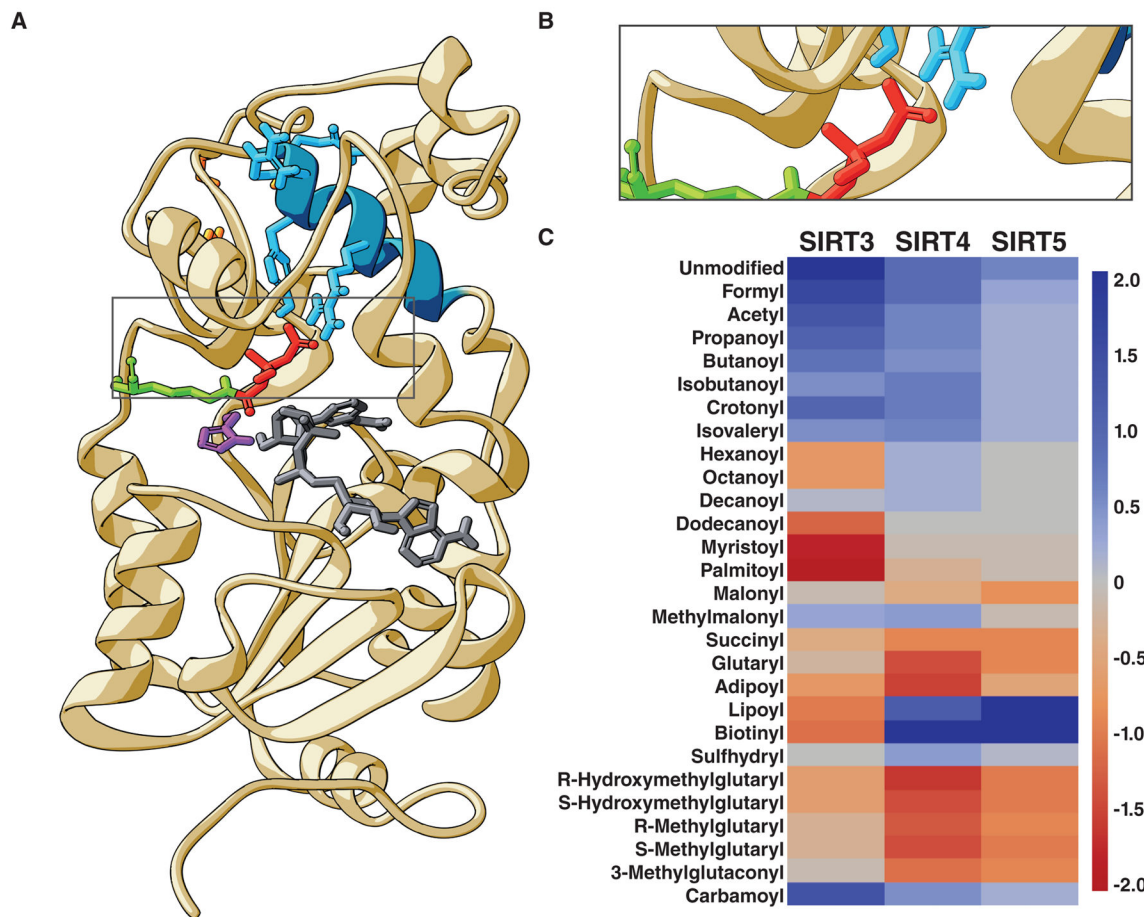


Figure 2. Structural and Modeling Studies on SIRT4 (See also Figure S2)

(A) Structural homology model of human SIRT4; NAD⁺ (black), catalytic H161 (magenta), zinc-binding cysteines (orange), conserved α -helix (cyan), lysine (green) with substrate (red); HMG-lysine shown as a prototypical substrate. (B) Enlarged view of catalytic pocket of SIRT4. (C) Heat map of energy minimization z-scores (-2.0—2.0) in the SIRT4 catalytic pocket of strong (red) and weak (blue) putative substrates.

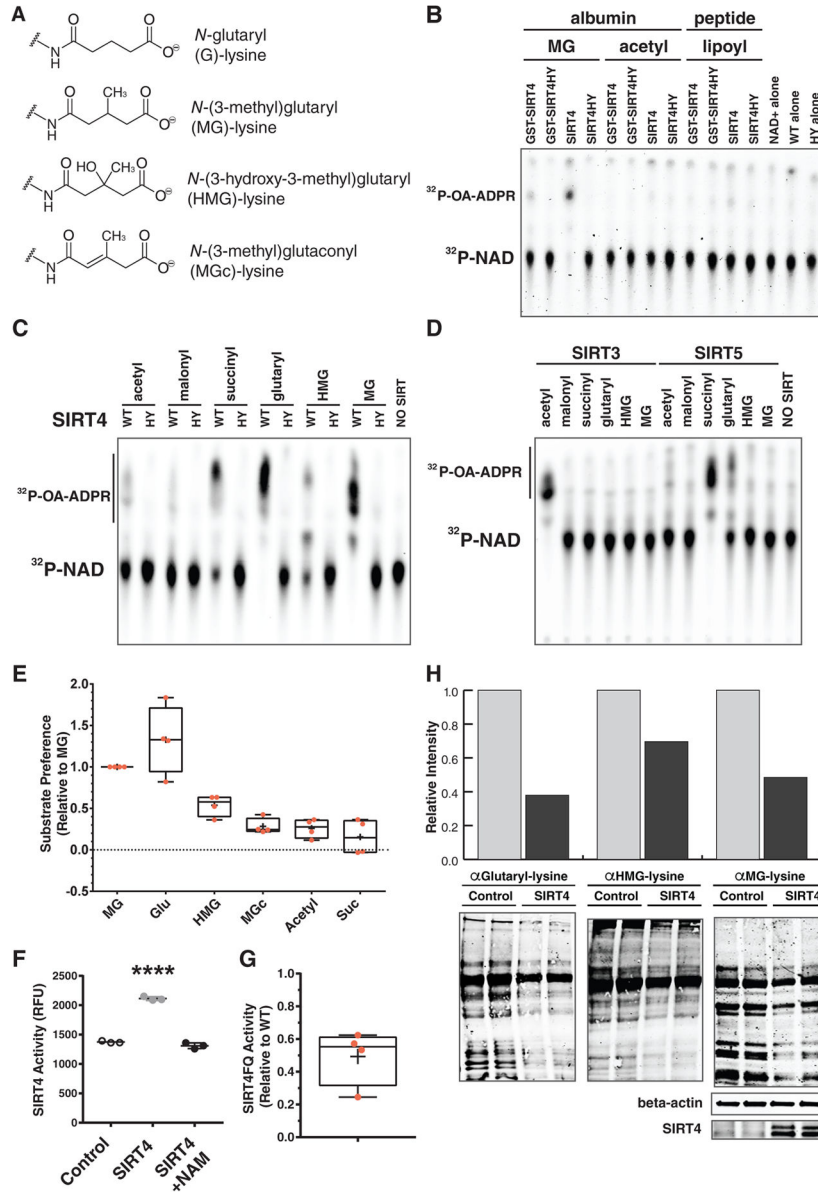


Figure 3. SIRT4 is a Lysine Deacylase (See also Figure S3)

(A) Structures of acyl-lysines removed by SIRT4. (B) SIRT4 activity assay using uncleaved (GST) or cleaved recombinant mouse SIRT4 or catalytically inactive SIRT4HY, targeting methylglutarylated BSA, acetylated BSA or a lipoyl-lysine peptide; lower spot, $^{32}\text{P-NAD}^+$; upper spot, $^{32}\text{P-O-acyl-ADP-ribose}$ (OAADPR). (C) Same assay from (B) using SIRT4 against a range of acylated BSA or peptide substrates. (D) Same assay from (B) using SIRT3 or SIRT5 against a range of acylated BSA or peptide substrates. (E) Profiling SIRT4 activity using AMC-labeled peptide substrates in a fluorogenic assay; results shown are from four independent experiments. (F) A representative experiment of SIRT4 incubated with AMC-labeled methylglutarylated peptide substrate with or without 4 mM nicotinamide; control contains no enzyme. Each column represents the mean \pm standard deviation (N=3). (G) Relative SIRT4FQ mutant enzyme activity compared to wild-type using 50 μM AMC-

labeled methylglutarylated peptide substrate in a fluorogenic assay; each data point is derived from an independent experiment. (H) Whole-cell extracts from 293 cells stably over-expressing SIRT4 or a control plasmid were immunoblotted using antibodies against glutaryl-, MG-, or HMG-lysine. Box plots depict the interquartile range with whiskers plotted to the min and max values. The horizontal line within the box is the median value and the “+” is the mean value. **** $p < 0.0001$ by Holm-Sidak post-hoc test.

Author Manuscript

Author Manuscript

Author Manuscript

Author Manuscript

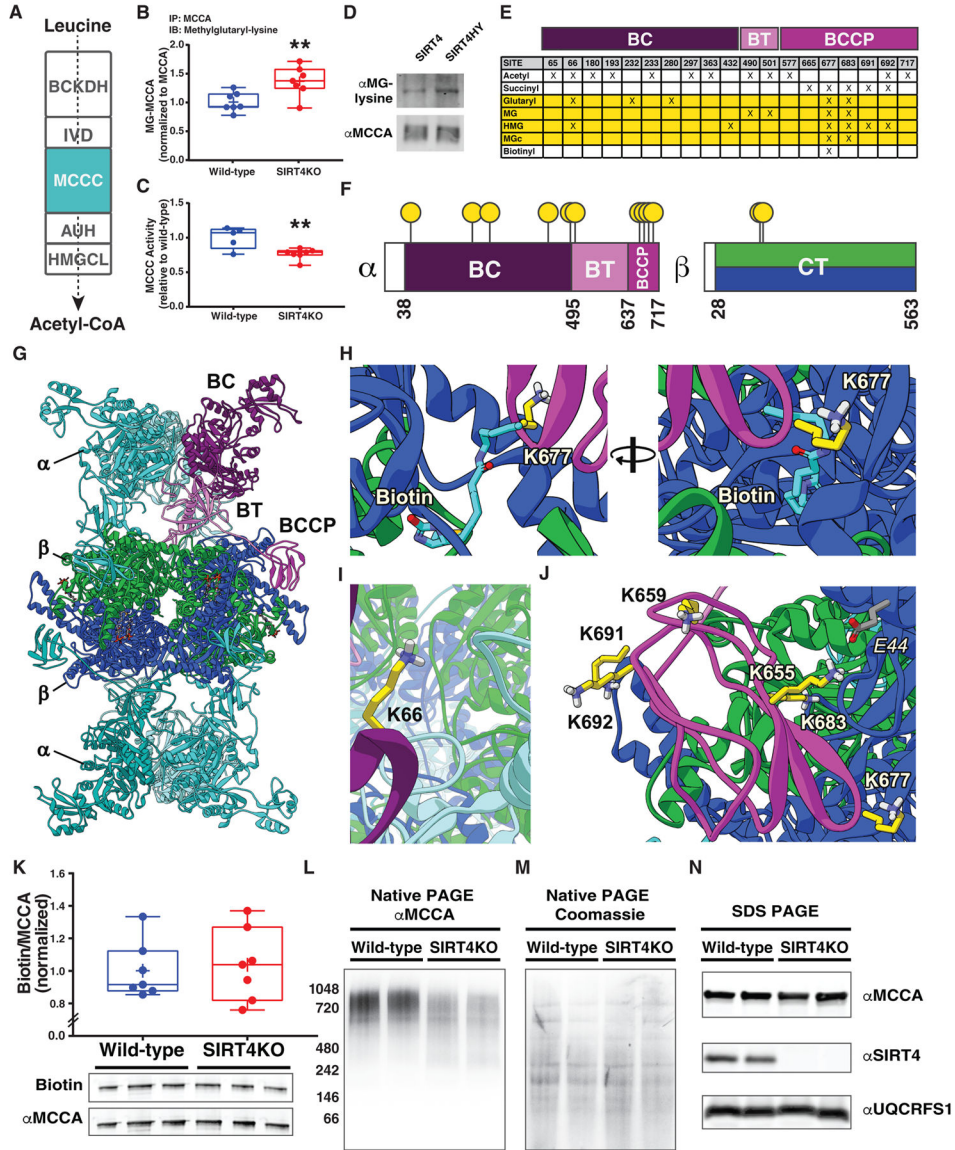


Figure 4. SIRT4 Ablation Leads to Disrupted MCCC Complex Formation (See also Figure S4)
 (A) Schematic representation of enzymes in leucine catabolism. (B) MCCA from wild-type and SIRT4KO liver was immunoprecipitated and immunoblotted using antibodies against MG-lysine and MCCA. Shown is quantification of the MG-lysine signal normalized for total MCCA where n=7/7 WT/SIRT4KO. (C) MCCC activity was measured from wild-type and SIRT4KO liver, n=5/7 WT/SIRT4KO. (D) MCCA was immunoprecipitated from SIRT4KO liver and incubated in SIRT4 deacylation reaction buffer with either SIRT4 or SIRT4HY mutant. Deacylation of MCCA was then assessed by immunoblotting using antibodies against MG-lysine and MCCA. (E) Summary table of sites of acylation identified on MCCC by proteomics (PTMs from peptides identified at 1% FDR with site localization probability of greater than 95% are represented by an “X”). PSMs were summed across sites for each PTM type. (F) 1D summary of acylation sites mapped on sub-domains of the MCCC α- and β-subunits, corresponding to colors in panels G–J; sites of acylation are stylized in yellow.

(G) Energy minimized mouse homology model of the murine MCCC complex; α -subunits are colored in shades of teal, with one magenta-shaded color-coded α -subunit showing BC, BT, and BCCP domains; β -subunits are colored blue and green. (H) Zoomed view of the location of K677 (yellow) or biotinylated K677 (cyan). (I) Zoomed view of K66 located at the interaction interface between MCCC α - α subunits. (J) Zoomed view the MCCC α BCCP domain, showing acylated Lys residues from (E) highlighted in yellow; amino acids numbers are labeled; binding amino acids are shown in gray and labeled in italics. (K) MCCA from wildtype and SIRT4KO liver was immunoprecipitated and blotted with α -streptavidin, to measure biotinylation, or with α -MCCA (n=7/7 WT/SIRT4KO); Top: summary of quantification of seven pairs of mice; Bottom: representative image. (L) Intact MCCC complex measured by native PAGE and α -MCCCA immunoblotting of hepatic WT and SIRT4KO mouse mitochondrial extracts. (M) Total native proteins from (L) measured by Coomassie staining serving as a loading control. (N) Total MCCCA, SIRT4, and UQCRES1 (as a control) protein from (L) measured by denaturing SDS-PAGE and immunoblotting with respective antibodies. Box plots depict the interquartile range with whiskers plotted to the min and max values. The horizontal line within the box is the median value and the “+” is the mean value. ** $p < 0.01$ by two-tailed Student’s t-test.

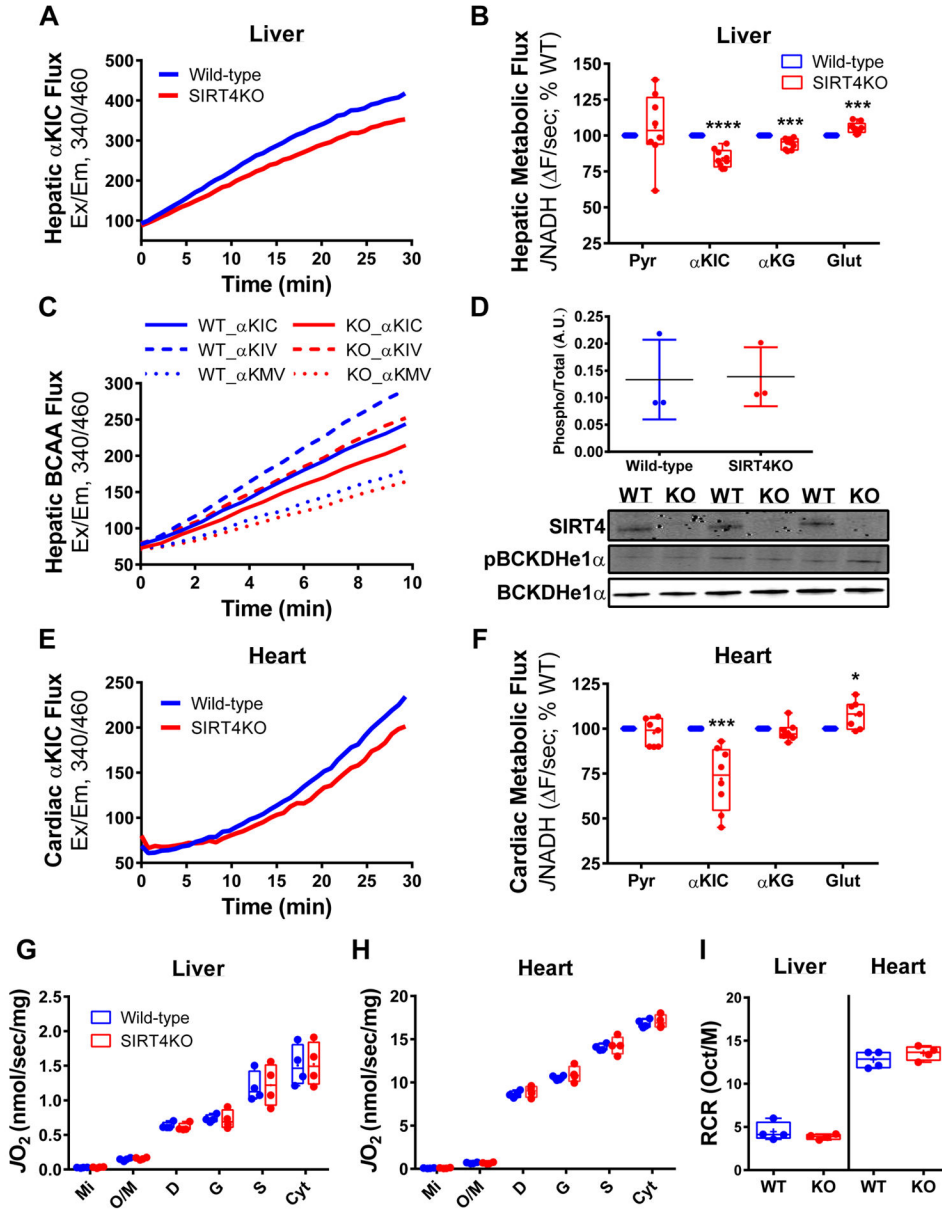


Figure 5. SIRT4 Ablation Reduces Leucine and BCAA Metabolic Flux (See also Figure S5)

(A) Representative trace of α -ketoisocaproate (α KIC) flux measured *ex vivo* in WT and SIRT4KO mouse liver mitochondria, monitored by NADH fluorescence (excitation 340nm/emission 460nm). (B) Quantification of relative hepatic substrate flux using pyruvate (Pyr), α KIC, α -ketoglutarate (α KG), or glutamate (Glu) as a substrate (n=9/9 WT/SIRT4KO). (C) Representative trace of BCAA flux using α KIC, α -ketoisovalerate (α KIV), or α -ketomethylvalerate (α KMV) measured *ex vivo* in WT and SIRT4KO mouse liver mitochondria, monitored by NADH fluorescence (n= 2/2 WT/SIRT4KO, excitation 340nm/emission 460nm). (D) Quantified levels and representative blot of phosphorylated BCKDHe1 α relative to total levels measured in WT and SIRT4KO mouse liver (n= 3/3 WT/SIRT4KO). (E) Representative trace of α KIC flux measured *ex vivo* in WT and SIRT4KO

mouse cardiac mitochondria, monitored by NADH fluorescence (excitation 340nm/emission 460nm). (F) Quantification of relative cardiac substrate flux using Pyr, α KIC, α -ketoglutarate (α KG), or Glu as a substrate (n=8/8 WT/SIRT4KO). (G–H) Oxygen consumption was assessed in isolated mitochondrial prepared from liver (G) and hearts (H) of WT and SIRT4KO mice. Respiration was assessed in the presence of mitochondria alone (Mi), followed by octanoyl-carnitine/malate (0.2/2mM; Oct/M), ADP (D; 1mM), glutmate (G; 10mM), succinate (S; 10mM) and cytochrome C (0.01mM; Cyt) (n=4/4 WT/SIRT4KO). (I) Respiratory control ratios (RCR) were calculated from respiration in the presence of ADP divided by that with Oct/M (n=4/4 WT/SIRT4KO). Box plots depict the interquartile range with whiskers plotted to the min and max values. The horizontal line within the box is the median value and the “+” is the mean value. * p <0.05, *** p <0.001, **** p <0.0001 by two-tailed Student’s t-test.

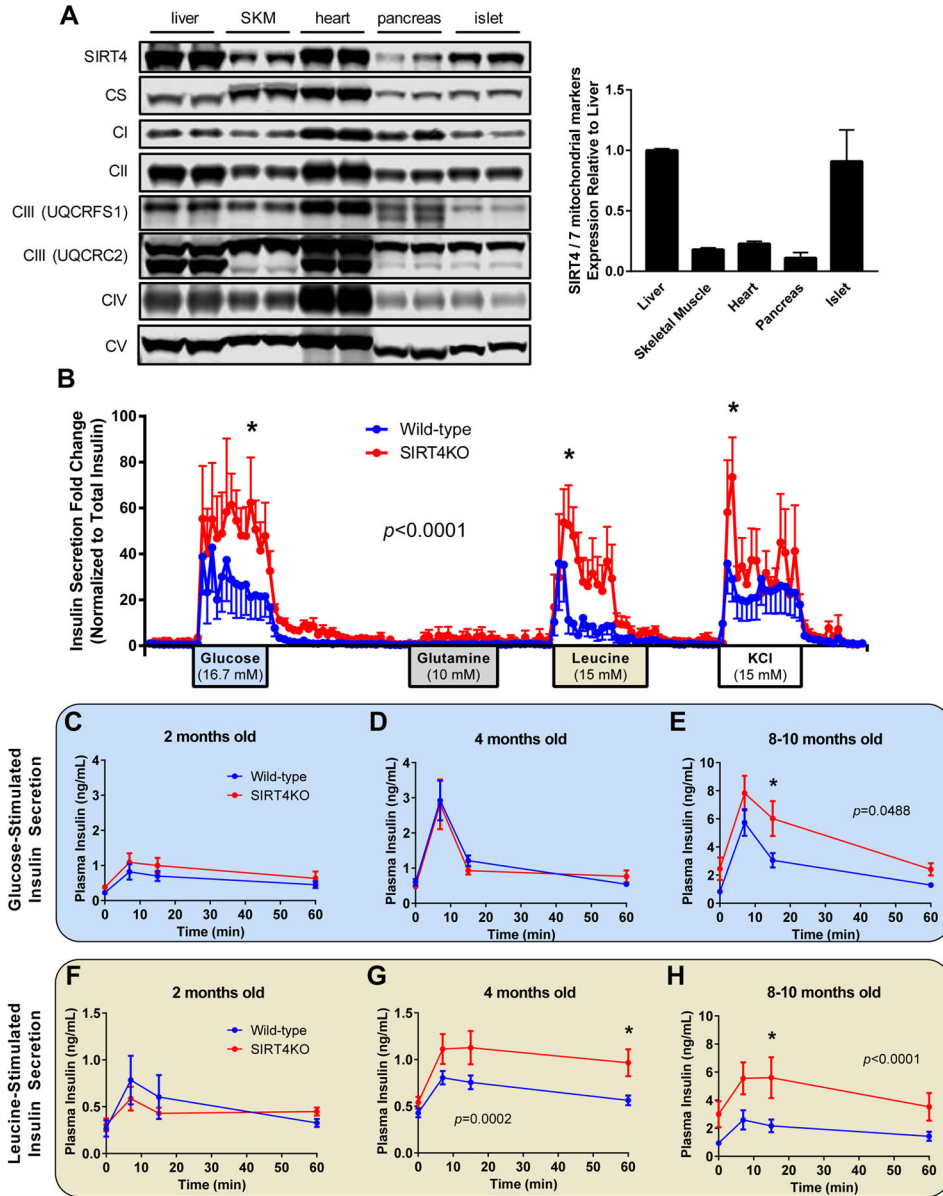


Figure 6. SIRT4KO Mice Have Increased Leucine-Stimulated Insulin Secretion (See also Figure S6)

(A) Immunoblot and quantification of SIRT4 expression normalized to 7 different mitochondrial markers: citrate synthase (CS), complex I (CI), complex II (CII), complex III subunit 5, ubiquinol-cytochrome C reductase, Rieske iron-sulfur polypeptide 1 (CIII, UQCRC1), complex III subunit 2, ubiquinol-cytochrome C reductase core protein II (CIII, UQCRC2), complex IV (CIV), complex V (CV). (B) Pancreatic islets were isolated from 4–5 month old male SIRT4KO mice and then subject to an islet perfusion; 75 islets each from $n=8/6$ WT/SIRT4KO mice. Islets were washed with Krebs Ringer buffer containing 2.7 mM glucose in between nutrient stimulations. (C–E) Plasma insulin was measured in 2 month old ($n=9/11$ WT/SIRT4KO), 4 month old ($n=6/4$), and 8–10 month old ($n=11/11$) wild-type and SIRT4KO male mice following an oral gavage of 1.5 mg/g glucose. (F–H) Plasma

insulin was measured in 2 month old (n=4/7 WT/SIRT4KO), 4 month old (n=15/15), and 8–10 month old (n=11/11) wild-type and SIRT4KO male mice following an oral gavage of 0.3 mg/g leucine. P values less than 0.05 by two-way ANOVA are indicated. Asterisks indicate $p < 0.05$ between wild-type and SIRT4KO by Holm-Sidak post-hoc test.

Author Manuscript

Author Manuscript

Author Manuscript

Author Manuscript

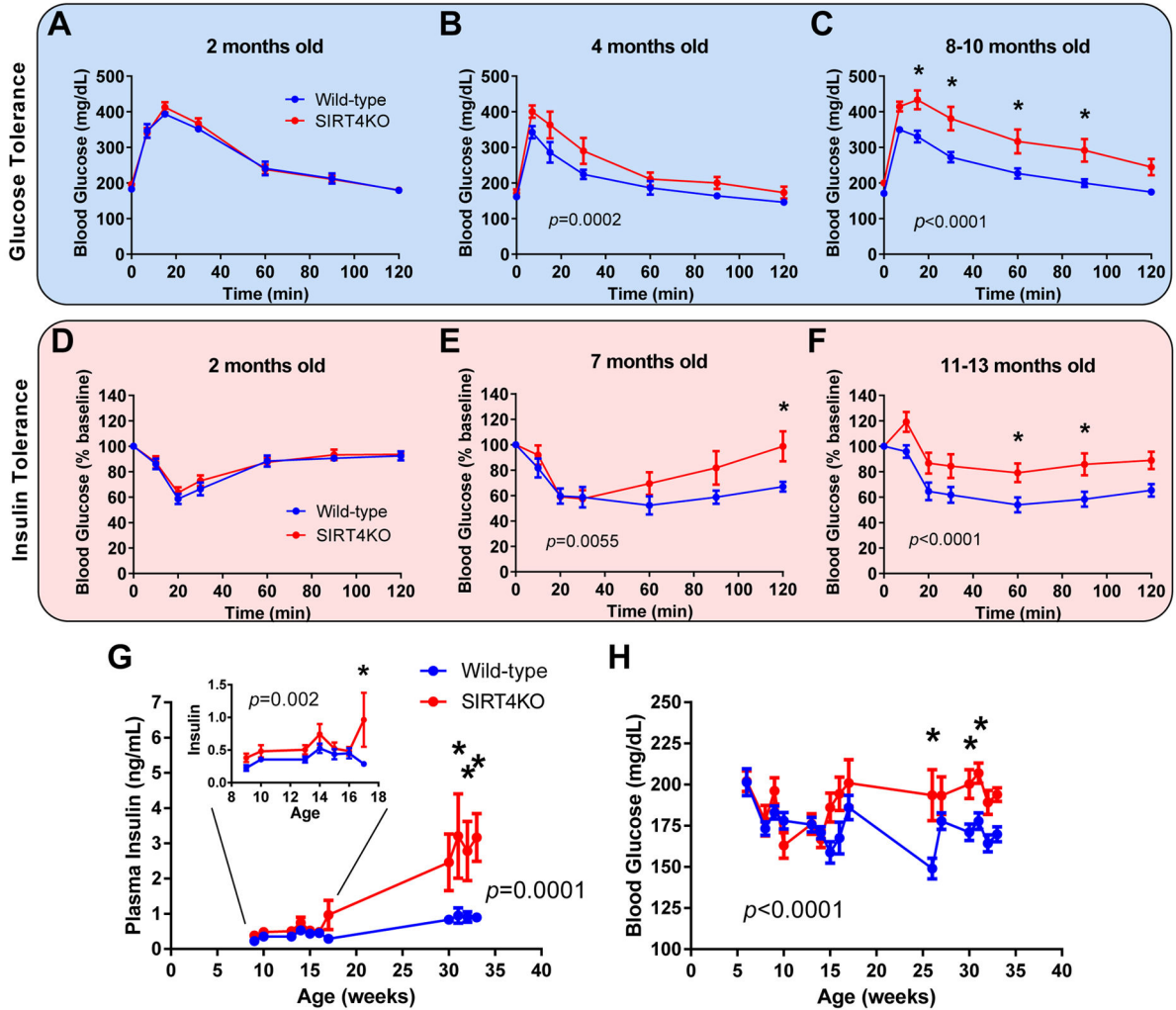


Figure 7. SIRT4KO Mice Develop Accelerated Age-Induced Disruptions in Glucose Homeostasis (A–C) Blood glucose was measured in 2 month old (n=9/11 WT/SIRT4KO mice), 4 month old (n=6/4), and 8–10 month old (n=11/11) wild-type and SIRT4KO male mice following an oral gavage of 1.5 mg/g glucose. (D–F) Blood glucose was measured in 2 month old (n=9/5 WT/SIRT4KO, 1 U/kg insulin), 7 month old (n=9/4, 1.2 U/kg insulin), and 11–13 month old (n=13/11, 1.4 U/kg insulin) wild-type and SIRT4KO male mice following an intraperitoneal injection of insulin. (G) Plasma insulin and (H) fasting blood glucose levels were measured in male wild-type and SIRT4KO mice following a 5–6 hour fast (n=4–15 per time point). P values less than 0.05 by two-way ANOVA are indicated. Asterisks indicate $p<0.05$ between wild-type and SIRT4KO by Holm-Sidak post-hoc test.